



Faculty of Engineering, Computer and Mathematical Sciences
SCHOOL OF MECHANICAL ENGINEERING

Ocean acoustic interferometry

DOCTORAL THESIS

12th October 2008

Author: Laura A. Brooks

Supervisor: Assoc. Prof. Anthony C. Zander [†]

Co-supervisors: Dr Peter Gerstoft ^{††}

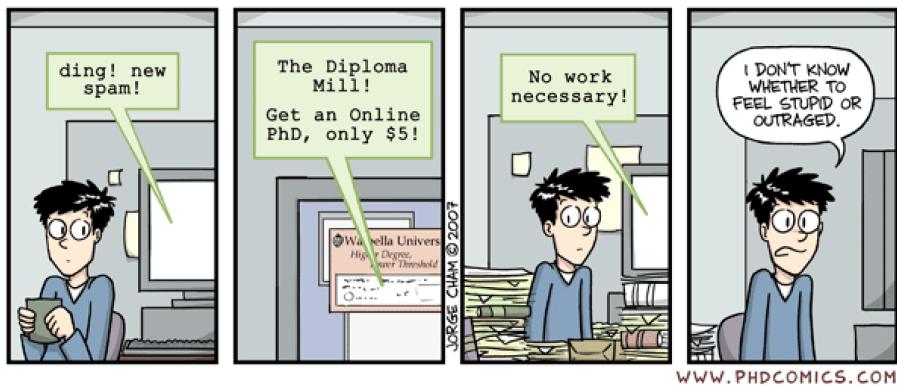
Prof. Colin H. Hansen [†]

Dr Z. Yong Zhang ^{*}

[†]School of Mechanical Engineering, The University of Adelaide, Australia

^{††}Marine Physical Laboratory, Scripps Institution of Oceanography, USA

^{*}Defence Science and Technology Organisation, Edinburgh, Australia



source: "Piled Higher and Deeper" by Jorge Cham - www.phdcomics.com

Doctoral Thesis

Brooks, Laura A.; October 2008
Acoustics, Vibration and Control Group
School of Mechanical Engineering
The University of Adelaide
SA 5005 Australia

Typeset by the author with the $\text{\LaTeX} 2_{\epsilon}$ document preparation system.

Printed in Australia.

Copyright © 2008, The University of Adelaide, South Australia.

All rights reserved. No part of this report may be used or reproduced, stored in a retrieval system, or transmitted in any form or by any means, electronic, mechanical, photocopying, recording or otherwise, without prior written permission of the university except in the case of brief quotations embodied in critical articles and reviews.

This thesis is dedicated to Ruth Myra Kinsman

Ab Ovo Usque Ad Mala

Abstract

Information from accurate ocean acoustic Green's function estimations can potentially be used to determine environmental characteristics such as water column and seafloor properties, knowledge of which is beneficial in numerous fields including sedimentology, oil exploration, and defence. Good estimates of acoustic Green's functions between two locations have previously been determined from cross-correlation of sound and vibration in other research fields. There is, however, limited literature that addresses Green's function approximation from cross-correlation of sound in the ocean. The work in this thesis therefore aims to further the understanding of Green's function approximation from cross-correlation of sound recorded at two locations in a shallow water oceanic waveguide, an approach referred to as ocean acoustic interferometry. Both active source and ship dominated ambient noise ocean acoustic interferometry are considered.

A stationary phase argument is used to relate cross-correlations from active sources to the Green's function between hydrophones. A vertical line source, a horizontal line source, and a horizontal hyperbolic source are considered. The theory and simulations are in agreement with related theory presented by others. The advantages and disadvantages of each source configuration are discussed.

Empirical Green's function approximations (EGFAs) were determined from ship dominated ocean noise cross-correlation. Direct and secondary path travel times between hydrophones were determined, and agree well with simulated data. Averaging the cross-correlations between equi-spaced

horizontal line array hydrophone pairs is shown to increase the signal-to-noise ratio. Analysis of temporal variations in the cross-correlations confirms that at any one time the signal is generally dominated by one or two sources. Cross-correlations obtained from data recorded during a tropical storm are shown to be clearer than those obtained at other times. This is due to both a reduction in nearby shipping, and an increase in overall sound levels caused by the increased wave action associated with the storm.

Ocean experiments were performed on the New Jersey Shelf. The direct acoustic path of the given ocean environment is shown to be highly sensitive to changes in sound speed profile, making reflection coefficient inversion difficult.

Cross-correlations of experimental data from a source lowered vertically and a source towed horizontally are compared and contrasted with the ship dominated noise cross-correlations, and also with cross-correlations of noise from a stationary ship. The EGFAs and their relationship to simulated Green's functions are explained using theory and simulations.

Two practical applications of ocean noise cross-correlation are also detailed: diagnosis of a multichannel hydrophone array, and array hydrophone self-localisation. Results obtained from active source measurements reveal that signals from several hydrophones, which were recorded on certain channels before a storm, were subsequently recorded on different channels after the storm. Noise cross-correlation of data recorded during the storm show when, and in what manner, these changes took place. Differences in travel times from any given source to hydrophone pairs were consistently less than expected for the assumed geometry. Travel times extracted from day long noise cross-correlations were used in an inversion to estimate array geometry. The resulting curved array geometry provided more consistent acoustic travel times from active noise sources than the assumed straight line geometry.

In summary, the findings documented in this thesis increase the understanding of Green's function approximation from cross-correlation of sound

in the ocean by providing: a theoretical and practical understanding of Green's function estimations for both active sources and passive ship dominated ambient noise; and examples of how the extracted travel times can be applied to practical situations.

Statement of Originality

This work contains no material that has been accepted for the award of any other degree or diploma in any university or other tertiary institution and, to the best of my knowledge and belief, contains no material previously published or written by another person, except where due reference has been made in the text.

I give consent to this copy of my thesis, when deposited in the University of Adelaide Library, being available for both loan and photocopying.

Laura Anne Brooks

Acknowledgements

The author expresses gratitude to her advisors, colleagues, friends, and family, who have provided both academic and emotional support throughout her time as a postgraduate student. This thesis, and more importantly, my growth as an individual, and as an academic, have benefited from your encouragement, assistance, loyalty, and support.

The author is appreciative of the two years spent as a visiting Fulbright scholar at the Marine Physical Laboratory, Scripps Institution of Oceanography, and of the opportunity to participate in sea trials during the Shallow Water 2006 experiments.

The experimental data used in this thesis could not have been obtained without the assistance of Scripps Institution of Oceanography; Applied Research Laboratories, the University of Texas at Austin; Woods Hole Oceanographic Institute; and the captain and crew of R/V *Knorr*, the ship that was used during the experiments.

This work has been supported by an Australian Postgraduate Award; the Defence Science and Technology Organisation; the Australian-American Fulbright Commission (along with Clough Engineering); the Office of Naval Research under Grant No. N00014-05-1-0264; and Scripps Institution of Oceanography, the University of California San Diego.

Contents

Abstract	i
Statement of Originality	v
Acknowledgements	vii
List of Tables	xii
List of Figures	xii
1 Introduction	1
1.1 Gaps in the literature	4
1.2 Document structure	5
2 Literature Review	9
2.1 Background	9
2.1.1 Propagation of sound in the ocean	10
2.1.2 Overview of the acoustic wave equation	15
2.1.3 Overview of the acoustic Green's function	16
2.1.4 Numerical solutions to the wave equation	18
2.2 Literature review on Green's function extraction	24
2.2.1 Early research	24
2.2.2 Uniform homogeneous medium	25
2.2.3 Interdisciplinary review	28
2.2.4 Simplified isovelocity ocean waveguide	31

2.2.5	Green's function extraction in the ocean	32
3	Active Source Ocean Acoustic Interferometry Theory	35
3.1	Vertical source column	36
3.1.1	Stationary phase evaluation	39
3.1.2	Incorporation of sediment layers	44
3.1.3	Spurious arrivals	48
3.1.4	Variations in sound speed profile	50
3.1.5	Generalised environment	51
3.1.6	Simulations	52
3.2	Horizontal straight line towed source	59
3.3	Horizontal hyperbolic towed source	60
3.4	Conclusion	62
4	Experimental Environment	65
4.1	Overview of experiment	66
4.1.1	Sound speed profiles	69
4.2	Analysis of experimental environment	70
4.2.1	Effects of ocean sound speed profile	72
4.2.2	Reflection coefficient inversion	73
4.2.3	Sub-bottom arrival time inversion	77
4.2.4	Conclusion	79
5	Ship Dominated Ambient Noise Cross-correlation	81
5.1	Introduction	82
5.2	Theory	83
5.3	Experiment	86
5.4	Analysis of data preprocessing methods	88
5.4.1	Removal of main contamination	89
5.4.2	Spectra and coherence	90
5.4.3	Frequency domain normalisation	94
5.4.4	Time domain normalisation	98

CONTENTS

5.5	Geometric comparisons	105
5.6	Temporal variations	110
5.7	Conclusion	115
6	Experimental Active Ocean Acoustic Interferometry	117
6.1	Background	118
6.2	Experiment	123
6.2.1	Data collection	123
6.2.2	Data analysis	125
6.3	Conclusion	141
7	Practical Applications of Travel Time Estimates	145
7.1	Introduction	145
7.2	Diagnosis of channel switching	147
7.2.1	Analysis of recorded data	147
7.2.2	Active sources	147
7.2.3	Ambient noise cross-correlations	150
7.2.4	Conclusion	156
7.3	Array shape estimation	157
7.3.1	Inter-hydrophone travel times	158
7.3.2	Inversion algorithm for array element localisation	158
7.3.3	Application to data	160
7.3.4	Conclusion	161
8	Conclusion	163
8.1	Summary of thesis findings	163
8.2	Recommendations for future work	167
8.2.1	Effect of various parameters on SNR	168
8.2.2	Additional source lowering experiments	169
8.2.3	Experimental hyperbolic source	170
8.2.4	Cross-correlations at seismic frequencies	171
8.2.5	Cross-correlations for monitoring gas hydrates	173

References	177
A Normalisation for Impedance Changes	189
B Array Details	191
B.1 Array geometries	192
B.1.1 MPL-VLA1 array	192
B.1.2 SWAMI arrays	194
B.1.3 Shark array	197
B.2 Array data acquisition specifications	199
C The Inversion Process	201
D Publications	203
D.1 Journal papers	203
D.2 Refereed conference papers	204
D.3 Invited talks	204
D.4 Other conference proceedings	204

List of Tables

5.1	Details of array configurations.	88
B.1	Data acquisition capabilities of the SWAMI arrays, MPL-VLA1 array, and Shark array.	199

List of Figures

2.1	Absorption of seawater at three temperatures as a function of frequency for salinity of 35 ppt and pH of 8.	13
2.2	Bottom reflection loss versus angle.	14
2.3	Vibrating sphere in an infinite fluid medium.	16
2.4	Cross-correlation of a source impulse in free space.	27
2.5	Free-field cross-correlation examples: broadband noise correlation function (NCF), derivative of the broadband NCF, filtered (0.05–0.2 Hz) NCF, and derivative of the filtered NCF.	28

2.6	Impulse source creates pseudo-diffuse field in a block, which is detected at receivers \mathbf{x} and \mathbf{y} ; the cross-correlation of the signals is compared to the signal which would be received at \mathbf{y} given an impulse source at \mathbf{x}	29
2.7	Waveguide without losses. (a) Green's function between receivers A and B showing direct, surface reflected, and bottom reflected paths with corresponding Green's function shown to the right. (b)–(c) Surface sources that yield (b) direct path, and (c) direct and single reflected paths, with corresponding cross-correlations shown at the far-right.	31
3.1	Source-receiver geometry and notation.	38
3.2	Examples of wave paths that correspond to stationary points.	41
3.3	Example of water source and sediment source stationary points that have the same path length to each receiver, and therefore the same path length difference.	46
3.4	The direct and bottom bounce paths are linked via a continuous transition through sediment source configurations.	47
3.5	(a) Waveguide with a downward refracting sound speed profile. (b) Geometry associated with the curved ray paths from the source to each receiver.	50
3.6	Simulated waveguide environments.	53
3.7	The cross-correlations for (a) the isovelocity waveguide, (b) the reflective environment with a sediment, (c) a magnified portion of (b), and (d) the refractive environment, plotted as a function of depth.	55
3.8	Two possible sets of ray paths: (a) direct path to B and the bottom bounce path to A ; and (b) a path to B with one water-sediment bounce and a path to A that has two transmissions through the interface.	57

LIST OF FIGURES

3.9	The difference between the path lengths from the source to receiver A and the source to receiver B as a function of source depth for the ray path geometry of Figure 3.8(b).	59
3.10	Geometrical construct for determining the equation governing the location of point p_n	61
3.11	Hyperbolic source track as viewed from above.	62
4.1	(a) Geographic location of the SW06 experimental site on the New Jersey Shelf. (b) Locations of the four hydrophone arrays.	67
4.2	Hydrophone array equipment prior to deployment.	68
4.3	Photographs of (a) the ITC-2015 mid-frequency source and (b) the source being controlled using a ship-board winch.	69
4.4	SSPs recorded from all CTDs measured from R/V <i>Knorr</i> between August 30 and September 6.	71
4.5	MPL-VLA1 array (a) geometry, and (b) SSPs from CTDs 36 and 37.	71
4.6	Modelled pressure amplitude of the 2200 Hz ocean-only field versus range and depth for source depths of (a) 45 m (SSP36), (b) 45 m (SSP37), and (c) 15 m (SSP36). Figures (d)–(g) show the amplitude versus depth at 230 m range using SSP36 and SSP37 for source depths of (d) 15, (e) 25, (f) 45, and (g) 65 m.	73
4.7	Match filter of 1500–4500 Hz chirp, recorded on all 16 hydrophones for a source depth of (a) 15m, and (b) 25m.	75
4.8	Match filter of 1500–4500 Hz chirp, recorded on all 16 hydrophones for a source depth of (a) 35m, and (b) 45m.	76
4.9	The square of the difference between the measured bottom and sub-bottom time differences, and the modelled values, summed over all source-hydrophone geometries.	78

5.1	(a) The relative VLA locations of SWAMI52, SWAMI32, and Shark. (b) SWAMI52 array geometry and hydrophone numbering system. (c) SSPs near SWAMI52 for August 30 and September 6. (d) Wind direction and (e) wind speed from August 31 to end of September 3.	87
5.2	Spectrograms and time-series of September 2 data: (a) signal dominated by mid-frequency fixed sound sources, (b) clipped signal, and (c) energy dominated by low frequency sources. . . .	91
5.3	Spectrograms of signals recorded on H-52, using the entire September 2 data, and coherograms of the data recorded on H-52 and H-40. The average of the individual spectra or coherences is plotted to the right of each figure.	93
5.4	Normalised spectra of the September 2 signal recorded on H-40 (a) before pre-filtering, and (b)–(e) after pre-filtering.	95
5.5	(a) Cross-correlations between H-52 and all other hydrophones for September 2 data using smoothed-whitening frequency filtering. (b)–(d) EGFA envelopes: (b) with smoothed whitening, (c) with no frequency normalisation, and (d) with no frequency domain filtering or normalisation.	97
5.6	Preprocessed waveforms for 2.5 s of 20–100 Hz bandpass filtered data from H-40 with normalisation method: (a) none, (c) threshold clipping, (d) one-bit, (e) RCTVW, and (f) ECTVW.	102
5.7	Summed cross-correlations and EGFA envelopes for all time normalisation methods for H-52 and (a) H-48 (entire day with 51.32 m horizontal separation), (b) H-8 (entire day with 230 m horizontal separation), and (c) H-8 (10:24 min from 8:30 Z).	103
5.8	(a) Summed cross-correlations and (b) EGFAs between H-52 and all other hydrophones for September 2. (c) Simulated Green’s functions convolved with a 20–100 Hz bandwidth linear source. (d) EGFA envelopes with the simulated travel times between the hydrophones.	106

LIST OF FIGURES

5.9 September 2 EGFA envelope with respect to: (a) H-34, and (a) H-10. 107

5.10 September 2 EGFA envelopes for (a) SWAMI32, with respect to H-30, and (b) Shark, with respect to H-16. 108

5.11 (a) Summed cross-correlations over September 2 for Shark hydrophone pairs separated by 345 m. (b) The median values from (a) overlie a shaded region between which all values lie. (c) Data from the dashed box in (b) are magnified. EGFA envelopes are shown in (d) using cross-correlations between H-52 and all other HLA hydrophones only, and in (e) using the median cross-correlations for all HLA hydrophone pairs. 109

5.12 EGFA envelope with respect to: H-52 for (a) August 31, (b) September 1, (c) September 2, and (d) September 3. 111

5.13 EGFA envelope for: (a) SWAMI52 H-52 and H-17 (230 m separation), (b) SWAMI32 H-30 and H-15 (200 m separation), and (c) Shark H-16 and H-35 (285 m separation). The envelope of the time gradient of the sum of all cross-correlations is shown at the right of each plot. (d)–(e) 20–100 Hz spectrograms from 3:36:40 Z August 31 for SWAMI52 H-52 and SWAMI32 H-30 respectively. (f) Enlarged view of SWAMI52 EGFA envelope. (g) The envelope of the time gradient of the sum of all cross-correlations for SWAMI52 data, excluding the period 12–24 Z August 31. 112

6.1 Source-receiver geometry and notation. 119

6.2 (a) Source and receiver geometries. (b) Plan view of array and source geometries showing where the source is towed and lowered. (c) SSPs from CTDs 42–44 with assumed SSP for modelling overlaid. 124

6.3	EGFA envelopes between H-30 and all other hydrophones for: (a) source lowered vertically, (b) source towed horizontally, (c) noise generated by R/V <i>Knorr</i> during the source lowering, and (d) ship dominated ambient noise.	127
6.4	Times corresponding to the direct path arrival EGFA envelope peaks of Figure 6.3 as a function of hydrophone number: (a) source lowering, (b) towed source, (c) stationary ship, (d+) causal ship dominated ambient noise, and (d-) acausal ship dominated ambient noise.	128
6.5	Source lowering. (a) Source (far left) is lowered from 9.8–60 m, and signals are recorded on H-5 and H-30. (b)–(g) Source-receiver geometry and stationary point paths for (b) direct, (d) surface, and (f) surface-bottom paths between the two hydrophones.	130
6.6	Cross-correlated data versus source depth: (a) experimental, (b) simulated, and (c) extract of simulated data.	132
6.7	View of part of the simulated cross-correlations showing the direct path to H-30 and bottom reflected path to H-5 surface convergence point (a), and the four sets of paths that converge to this point as the source moves towards the surface (b)–(e). . . .	133
6.8	Sum of the H-5 and H-30 cross-correlations from the source lowering experiment is compared to the simulated cross-correlations and the simulated source shaded Green’s function.	134
6.9	Cross-correlated towed source data, (a) experimental and (b) simulated, as a function of range from H-30.	137
6.10	Source-receiver geometry and stationary point paths for (a) direct path, (b) surface reflection path, and (c) surface-bottom reflection path. (d)–(f) Stationary phase geometries that yield spurious arrivals.	138

LIST OF FIGURES

6.11 Sum of the H-5 and H-30 cross-correlations from the towed source experiment is compared to the simulated summed cross-correlations and the simulated source shaded H-5–H-30 Green’s function. 139

6.12 Cross-correlations of H-30 and H-5 data from the stationary ship as a function of time during the source lowering event. The sum of the cross-correlations is shown underneath. 140

6.13 Short time cross-correlations of 6 minutes and 24 seconds for H-30 and H-5 ship dominated ambient noise data as a function of time of September 2. The sum of the entire day’s cross-correlations is shown underneath. 142

7.1 (a) Array geometry. (b)–(d) Schematics showing the connections between hydrophones and channels: (b) at deployment, (c) after the first switch, and (d) after the second switch. 148

7.2 Envelope of the signal recorded on each channel (a) before the storm, and (b) after the storm. (c) Signal envelope from after the storm with channels re-sorted. 149

7.3 Short time cross-correlations between channel 13 and all other channels from the time period surrounding the first switch (a) 7:07:37 Z and (b) 7:14:01 Z, and from the time period surrounding the second switch (c) 12:08:40 Z and (d) 12:15:05 Z. (e)–(g) 20 s long cross-correlations at 12:14 Z for times (e) 20–40 s, (f) 30–50 s, and (g) 40–60 s. 152

7.4 (a)–(c) Cross-correlations between channel 13 and all other channels after re-sorting the channels, plotted as a function of distance from hydrophone 13: (a) before, (b) between, and (c) after the switches. (d)–(f) Normalised envelopes of the cross-correlation function time-derivatives: (d) before, (e) between, and (f) after the switches. 155

7.5	Arrival time as a function of distance from the first HLA element, from (a) before the first switch, (b) after one channel has switched, and (c) after both channels have switched.	156
7.6	Array element locations: <i>a priori</i> and <i>a posteriori</i> results from non-linear least squares travel-time inversion.	161
8.1	Mid-frequency SWAMI32 towed source tracks: straight, hyperbolic path 1, and hyperbolic path 2.	171
8.2	Hyperbolic tracks were achieved with dynamic ship positioning.	172
8.3	Locations of fixed sound sources and hydrophone arrays	173
8.4	Location of Mississippi Canyon Block 118.	174
8.5	Gas hydrate sea-floor observatory in Mississippi Canyon Block 118.	175
B.1	MPL-VLA1 mooring diagram.	193
B.2	SWAMI32 mooring diagram.	195
B.3	SWAMI52 mooring diagram.	196
B.4	Shark mooring diagram.	198
C.1	The inversion process.	202

Chapter 1

Introduction

The attenuation of sound as it travels through water is significantly less than that of light or radio waves and therefore acoustics is the preferred means of underwater exploration, communication and target acquisition.

Acoustic signals recorded on a hydrophone, or an array of hydrophones, contain information about the environment in which they are measured. The relationship between recorded acoustic signals and the ocean environment has been an important area of research since submarines took an active role in defence in the First World War, and much of the fundamental material has since been documented [1–5]. Theoretical relationships between the environment and acoustic propagation within it can be determined for simple environments, but a realistic ocean environment requires numerical methods to solve for acoustic propagation. Full inversion techniques have traditionally been employed to analyse hydrophone data in attempts to characterise properties of the waveguide environment and to define underlying sediment properties [6]. The main drawbacks of these techniques are that optimisation over multiple variables results in a computationally expensive problem, and uniqueness problems often occur.

The Green's function between two points is the point source solution of the governing acoustic propagation equations (i.e., it is the signal that would be received at one point given a unit impulsive source at the other).

It is fully dependent upon the geometry and environment under consideration, and therefore can be used to determine information about the environment, in this case the ocean waveguide and the underlying sediment, through which acoustic transmission between the two points takes place. Approximation of the acoustic Green's function in the ocean using simple processing techniques is therefore an exciting prospect.

The most straightforward method of determining the Green's function between two points A and B is to excite a source at one of the points, A say, and record the subsequent signal at a receiver located at B . The Green's function is then extracted from the received signal by deconvolution with the source signal.

It has been shown that good estimates of the acoustic Green's function between two points can be determined from cross-correlations of diffuse sound fields [7]. This concept, which eliminates the requirement of having a source at either location, has been successfully applied to problems in ultrasonic noise [8–10], ambient noise in a homogeneous medium [11], seismic noise [12–19], moon-seismic noise [20], and even human skeletal muscle noise [21].

To obtain an accurate representation of the Green's function between two receivers, there is a local requirement that waves propagate on average isotropically near both receivers [13]. This could theoretically be achieved in the ocean by locating the two points between which the Green's function is to be estimated within a volume distribution of sources. Such a configuration is, however, unrealistic in practice.

The ocean noise field is dominated by wave generated noise above a few hundred Hertz [22–24] and shipping noise below about 100 Hz [22, 23]. Wave generated ambient noise is concentrated near the ocean surface, and although it gives an approximately uniform sheet of sources, the absence of sources lower in the waveguide means that the ocean acoustic modes are not all excited. As a result, time-averaged cross-correlations of ocean surface wave noise will produce accurate inter-hydrophone travel times, but

incorrect amplitudes [15]. Ship sources give low frequency high amplitude signals, which have high coherence over greater distances. The distribution of these sources, also concentrated near the surface, is less uniform than wave generated noise, but cross-correlations over a sufficiently long interval should yield an amplitude shaded Green's function (i.e., a Green's function convolved with amplitude factors) similar to that obtained from ocean wave noise [25, 26].

Biological organisms, such as fish, can give a quasi-volume source distribution, but again, they tend not to span the entire depth of the water column. Travel times have successfully been extracted from cross-correlation of croaker fish dominated noise [27].

Alternate source configurations can be achieved using active sources. For example, a simplification of a volume distribution can be achieved using a vertical column of sources, which can potentially excite all water-borne modes.

There are less than a dozen refereed papers in the literature that address Green's function approximation from acoustic cross-correlations in the ocean. The work in this thesis therefore aims to further the understanding of the Green's function approximation between two points in a shallow water (<100 m) oceanic waveguide without having a source at either location. The approach of inferring the Green's function between two receivers from signal cross-correlation in the ocean is referred to here as *ocean acoustic interferometry*, due to its relationship to classical and seismic interferometry [28]. This thesis focusses upon ocean acoustic interferometry using two source types: active sources, and opportunistic ship noise. Ship noise has the advantage of no additional source instrumentation being required. Active sources have the advantage of higher frequencies, which give sharper arrival peaks, as well as controllability and continuous monitoring. Theoretical descriptions, simulated results, and experimental results, are presented for each case.

1.1 Gaps in the literature

A detailed discussion of literature relevant to this research is presented in **Chapter 2**. A conceptual explanation of the emergence of Green's function characteristics from cross-correlations, and an inter-disciplinary discussion of relevant cross-correlation literature, are presented. The chapter concludes with a more specific discussion of previous publications concerning Green's function estimation from cross-correlations in the ocean environment.

This thesis will address the following gaps in the literature which have been identified:

1. It has been shown theoretically using a modal approach in the frequency domain, and through simulation, that the Green's function between two receivers in a waveguide can be determined by summing the cross-correlations from a vertical line of sources that are located in the same vertical plane as the receivers, external to them [29]. Theoretical arguments based on the method of stationary phase have been used by others to formulate the time domain Green's function for time-averaged surface generated ambient ocean noise cross-correlation [15] and seismic interferometry [30]. Stationary phase arguments have not previously been applied to active source configurations in the ocean. In addition, detailed theoretical descriptions of horizontal active source configurations have not been considered previously.

Stationary phase descriptions of both vertical and horizontal source configurations will be presented within this thesis. These theoretical formulations will be supported by simulations. This work is presented in Chapter 3.

2. It has been shown experimentally that for a ship track passing through the end-fire plane of a pair of hydrophones (i.e., the vertical plane containing the hydrophones), if sufficiently long time windows are used, then the signal from the end-fire location dominates the cross-correlation function [25]. An in-depth analysis of cross-correlations

from ship dominated ocean noise has not, however, previously been presented.

Results from cross-correlation of ship dominated ambient noise data will be presented and analysed in detail in this thesis. The arrival time structure of empirical Green's function approximations determined from these cross-correlations will be compared to that of simulated Green's functions. This work is presented in Chapter 5.

3. The first gap in the literature pertained to theoretical descriptions of Green's function approximation from cross-correlation of active noise sources. Experimental validation of the theory has not previously been presented.

An experiment in which a source is lowered vertically through the waveguide, and one in which a source is towed along a straight line towards an array, are described in this thesis. Results from these experiments are presented and compared with simulated results and theory in Chapter 6. The results are also compared and contrasted to those obtained from ship dominated ambient noise cross-correlations.

4. Acoustic travel times extracted from ambient noise cross-correlations have been used by others [27] for array localisation and synchronisation. Other practical applications for the extracted travel time data have not been explored.

A practical application of noise cross-correlation for the diagnosis of a multichannel ocean hydrophone array is derived and presented in Chapter 7 of this thesis.

1.2 Document structure

For the benefit of non-experts in the field of ocean acoustics, background ocean acoustic theory is provided in Section 1 of **Chapter 2**. The propagation of sound in the ocean and the associated governing equations are

introduced. A summary of how the Green’s function can be derived from the wave equation for a simple point source is then presented, along with a discussion of the various numerical models that are used to solve the wave equation in realistic ocean environments. Section 2 of **Chapter 2** is a critical literature review that confirms the gaps in the literature outlined in the previous section.

Chapter 3 addresses the first gap in the literature. A stationary phase argument is used to describe the relationship between the stacked cross-correlations from a line of vertical sources, located in the same vertical plane as two receivers, and the Green’s function between the two receivers. Theory and simulations demonstrate the approach and are in agreement with those of a modal based approach presented by others. Results indicate that the stacked cross-correlations can be directly related to the shaded Green’s function, provided the modal continuum of any sediment layers is negligible. A horizontal source configuration can be used instead of a vertical column. The relationship between the summed cross-correlation for a horizontal line source configuration and the Green’s function is given. If range independence is assumed, it is demonstrated that the Green’s function can be approximated from cross-correlations of a horizontal hyperbolic towed source with its apex at a location horizontally between two physical hydrophones. The chapter concludes with a brief comparison of the three active source configurations.

In **Chapter 4** an overview of the Shallow Water 2006 (SW06) experiment is given. The direct acoustic path, that is, the acoustic path that does not interact with the sea surface and seafloor, is shown to be highly sensitive to changes in sound speed profile. This makes reflection coefficient inversion difficult, although attempts to do so suggest a critical angle and sediment sound speed in agreement with that estimated by others.

Chapter 5 addresses the second gap in the literature. Cross-correlation of ocean noise in the 20–100 Hz frequency range is discussed. Ocean noise data, collected by three L-shaped arrays during the SW06 sea tri-

als, were cross-correlated in order to approximate Green's functions, and subsequently acoustic travel times of the main propagation paths, between hydrophone pairs. Examination of the individual noise spectra and their mutual coherence reveals that the propagating noise is most coherent at ship noise dominated frequencies of less than 100 Hz. Both time and frequency domain preprocessing techniques, and their effect upon the cross-correlations, are investigated. Travel times corresponding to the envelope peaks of the noise cross-correlation time-derivatives are in agreement with the expected direct and surface reflected inter-hydrophone travel times. Summing the cross-correlations between equi-spaced hydrophone pairs in a horizontal line array (HLA) is shown to increase the signal-to-noise ratio. Temporal changes in short-time cross-correlations highlight individual ship tracks and show that the sound field is more diffuse during the passing of a tropical storm.

The third gap in the literature is addressed in **Chapter 6**. Cross-correlations obtained using two active source configurations (source lowering and towed source) are compared and contrasted with cross-correlations from a noise field dominated by shipping, and also with cross-correlations of noise generated during the source lowering event by the ship from which the source was being controlled. The various source configurations are investigated theoretically, and experimental results for each source type, from cross-correlation of data collected during the SW06 sea trials, are compared.

Chapter 7 details two practical applications of noise cross-correlation: the analysis of *channel switching* on an ocean hydrophone array, which addresses the fourth gap in the literature; and array element self-localisation, using a methodology similar to that of others [27]. Channel switching refers to the event where signals from a given hydrophone that were originally recorded on a certain channel are subsequently recorded on a different channel. Acoustic data were recorded on the horizontal portion of an array on the New Jersey Shelf during the passing of Tropical Storm Ernesto on September 2 2006. Results obtained from active source measurements prior to

and after the passing of the storm revealed that several channels switched during the storm. Noise cross-correlation of data recorded during the storm was performed, and changes in the cross-correlation showed when, and in what manner, the channel switching took place. In addition to the channel switching, it was noticed that travel times of acoustic data recorded on the array showed inconsistencies with the given array geometry; differences in travel times from any given source to HLA hydrophone pairs were consistently less than expected. It was therefore hypothesised that the HLA was not lying in a straight line on the seafloor. Travel times extracted from day long ambient noise cross-correlations, with the channel switching taken into account, are used in a non-linear least squares inversion to estimate array geometry. The resulting geometry is consistent with acoustic travel times of active acoustic sources.

Conclusions from the research are presented in **Chapter 8**. Possible directions for future work are outlined. Much of the work presented in this thesis has been either published or submitted for publication by the author in international journals and conference proceedings, as listed in Appendix D.

Chapter 2

Literature Review

This chapter is organised into two main sections: background ocean acoustic theory is presented in Section 2.1, and a critical review of the literature pertinent to the work in this thesis is presented in Section 2.2.

2.1 Background

In order to fully appreciate why one would want to “approximate the acoustic Green’s function in the ocean via cross-correlation methods”, one must first have a basic understanding of what the Green’s function represents and hence why it is useful to obtain an approximation of it, as well as of the potential benefits of estimating the Green’s function via cross-correlation as opposed to traditional methods.

The physical and chemical factors that affect how sound propagates in the ocean are described in Section 2.1.1. The equations that govern the propagation of sound: the acoustic wave equation, and its frequency equivalent, the Helmholtz equation, are subsequently introduced in Section 2.1.2. The Green’s function between two points, defined as the solution to the Helmholtz equation at the second point given a unit impulse applied at the first point, is then introduced in Section 2.1.3. In simpler terms, the Green’s function takes every little detail of the ocean environment into account, and

2. LITERATURE REVIEW

for any given sound source at one location, it specifies the signal that will be received at another location.

The Green's function can be derived theoretically from the acoustic wave equation for a simple source and geometric configuration, and a summary of the derivation for the example of a point source in an unbounded homogeneous medium is presented in Section 2.1.3. In more realistic ocean environments the governing boundary value problem becomes too complex to solve analytically, and numerical solutions are required. The most common types of numerical models used to generate solutions to the wave equation are briefly described in Section 2.1.4.

2.1.1 Propagation of sound in the ocean

The propagation of sound in the ocean is influenced by many factors including the physical and chemical properties of the water column, the structure and properties of the seafloor, and roughness at the sea surface interface.

Sound speed profile (SSP)

The speed of sound in water, c , is a function of static pressure (related to depth [31]), salinity, and temperature. A commonly used approximation for the relationship is [32]

$$c = 1449.2 + 4.6T - 0.055T^2 + 0.00029T^3 + (1.34 - 0.01T)(S - 35) + 0.016z, \quad (2.1)$$

where T is the temperature in degrees Celcius ($0 \leq T \leq 35^\circ \text{C}$), S is the salinity in parts per thousand ($0 \leq S \leq 45 \text{ ppt}$), and z is the depth in metres ($0 \leq z \leq 1000 \text{ m}$). More complex formulae for the relationship, which should be considered if high accuracy is needed, also exist [33, 34].

Temperature and pressure effects dominate salinity effects. In a shallow water environment the sound speed is generally either dominated by a negative thermocline, a thin layer in which temperature and hence sound speed decrease rapidly with depth, or is nearly constant over depth. The upper

surface layer (i.e., the layer above the thermocline) is highly susceptible to weather influences. Diurnal heating warms the ocean surface and wave action mixes this warmer water with underlying cooler water, yielding a surface layer of approximately uniform temperature and sound speed. Below this mixing layer the temperature decreases rapidly, resulting in a steep negative thermocline. At even greater depths pressure effects dominate, and the sound speed then increases slowly with depth.

The propagation of sound through the ocean is described by Snell's law:

$$\frac{\cos \theta}{c} = \text{constant}, \quad (2.2)$$

where θ is the ray angle relative to the horizontal and c is the local sound speed. Sound is therefore locally refracted towards regions of low sound speed. Shallow water environments with a strong negative thermocline are downward refracting, and hence long range acoustic propagation is dominated by bottom-interacting acoustic paths. At shorter ranges acoustic propagation will be a combination of direct, surface reflected, seafloor reflected, and multiple-reflected paths.

Spreading and attenuation losses

The amplitude of propagating sound decreases due to a combination of attenuation and spreading effects. Geometric spreading is dominated by spherical or cylindrical effects, while attenuation is dominated by volume absorption, bottom reflection loss, and scattering losses at the surface and seafloor.

Spherical spreading occurs when sound propagates away from a source uniformly in all directions. This type of model is valid in the near-field ($r \leq D$, where D is ocean depth) of point sources located away from the ocean waveguide boundaries. Consider sound spreading spherically from a sphere of radius r_0 to a larger sphere of radius r . The power radiates equally in all directions, and neglecting attenuation, remains constant with

2. LITERATURE REVIEW

range:

$$P = 4\pi r_0^2 I_0 = 4\pi r^2 I, \quad (2.3)$$

where I is the acoustic intensity. The transmission loss (TL) between two points due to spreading is defined by the ratio of the intensity at the second point with reference to the intensity at a radius of $r_0 = 1$ m from an acoustic source:

$$\text{TL} = -10 \log_{10} \left(\frac{I}{I_0} \right) = 10 \log_{10} (r^2) = 20 \log_{10} (r). \quad (2.4)$$

Due to the upper and lower boundaries of the ocean, at ranges far from the source ($r \gg D$) sound propagates with cylindrical wavefronts. The power across the wavefront becomes

$$P = 2\pi r_0 D I_0 = 4\pi r D I, \quad (2.5)$$

and the transmission loss is therefore

$$\text{TL} = 10 \log_{10} (r). \quad (2.6)$$

Volume absorption is the dominant attenuation factor for a path that does not have any boundary interactions. It is caused by viscosity and chemical relaxation, and is dependent upon temperature, salinity, acidity, and frequency. Several algorithms exist for calculating absorption in a given environment. Fisher and Simmons [35] presented an equation that is valid for a standard salinity of 35 ppt and a pH of 8. Francois and Garrison [36] presented a more complex relationship that is valid for a greater range of water properties, and Ainslie and McColm [37] subsequently presented a simplified relationship that is also valid for a standard range of oceanographic conditions. An example of absorption plotted as a function of frequency [36] is shown in Figure 2.1. Volume absorption can be seen to increase significantly with frequency, and hence long range propagation is dominantly at lower frequencies.

Sound that interacts with the seafloor is governed by Eq. (2.2). The sound speed and density, and hence the characteristic acoustic impedance, ρc , of the sediment at the seafloor is usually significantly greater than within

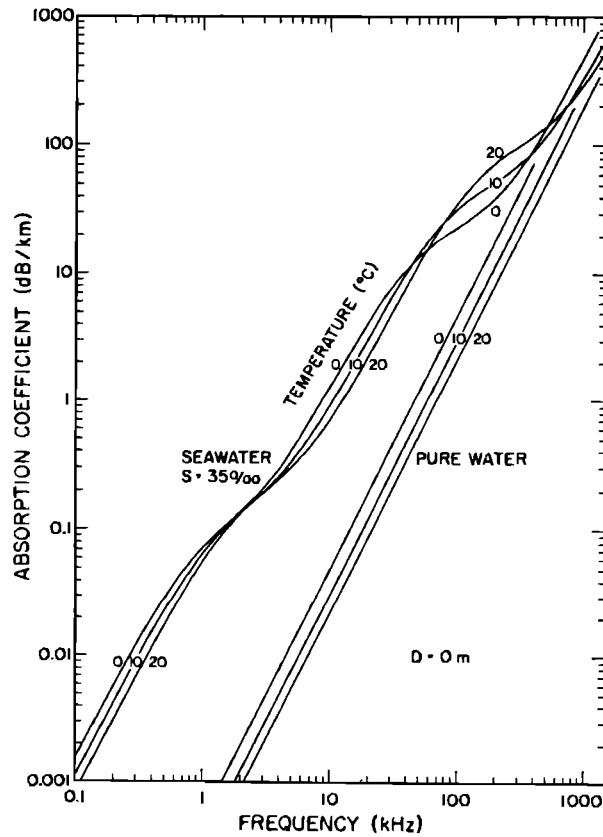


Figure 2.1: Absorption of seawater at three temperatures ($^{\circ}\text{C}$) as a function of frequency for salinity of 35 ppt and pH of 8. Pure water attenuation is also shown as a reference (source: Francois and Garrison [36]).

the water column, and therefore the effect on acoustic propagation can be large. If the water is defined as medium 1 and the sediment as medium 2, Snell's law can be rewritten as $\frac{\cos \theta_1}{c_1} = \frac{\cos \theta_2}{c_2}$, where θ_1 is the horizontal angle, defined as the grazing angle, of the incident acoustic path, and θ_2 is the angle of the acoustic path in the second medium. In general, some of the incident acoustic energy is reflected from the interface with a reflection angle of θ_1 , while some of the energy transmits to the sediment with a refraction angle of θ_2 . The proportion of the energy that is reflected depends upon the ratio of impedances as well as the incident grazing angle. Since

2. LITERATURE REVIEW

$c_2 > c_1$, there exists a real valued grazing angle, defined as the *critical angle*, $\theta_1 = \theta_c = \arccos(c_1/c_2)$, below which θ_2 becomes complex. An acoustic path with a grazing angle less than or equal to the critical angle will therefore experience perfect reflection with an associated phase change. At angles above the critical angle, some of the energy is transmitted into the sediment; the steeper the grazing angle, the greater the transmission. Hence, at high grazing angles bottom reflection losses become the dominant loss mechanism. The bottom loss as a function of grazing angle for a typical environment [38] is shown in Figure 2.2.

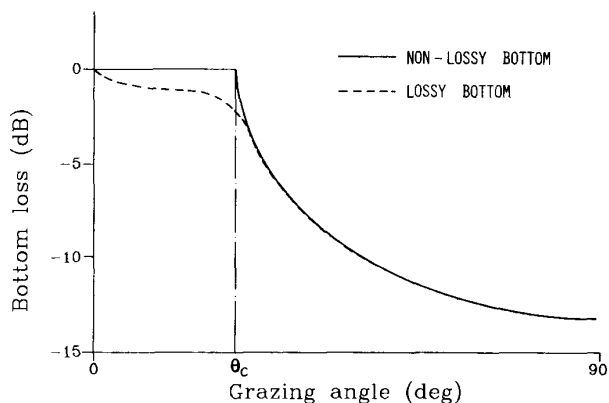


Figure 2.2: Bottom reflection loss versus angle for a non-lossy bottom, defined as a bottom with no p-wave attenuation, and also for a lossy bottom, defined as one with a high p-wave attenuation factor. (source: Jensen [38]).

Scattering is redirection of sound, through transmission, reflection, and diffraction, as it encounters an inhomogeneity. Sound in the ocean is scattered by roughness at both the sea surface and the seafloor. The amount of scattering increases with surface roughness, frequency, and grazing angle. The process of boundary scattering is physically complex and as such the literature is extensive (see Ogilvy [39] for a review). Volume scattering in the ocean occurs due to sound interaction with air bubbles, marine life and small-scale ocean structure such as internal waves (see Medwin and Clay [3] for a review).

2.1.2 Overview of the acoustic wave equation

Forward propagation models are based upon the acoustic wave equation. The wave equation in an ideal fluid stems from hydrodynamics and the adiabatic relationship between pressure and density. From the first order representation of the conservation of mass, Euler's equation, and the adiabatic equation of state, the linear acoustic homogeneous three-dimensional wave equation for pressure is derived to be [4]

$$\rho \nabla \cdot \left(\frac{1}{\rho} \nabla p \right) - \frac{1}{c^2} \frac{\partial^2 p}{\partial t^2} = 0, \quad (2.7)$$

where ρ is the density, p is the pressure, c is the speed of sound within the fluid, t represents time, $\nabla = \mathbf{i}(\partial/\partial x) + \mathbf{j}(\partial/\partial y) + \mathbf{k}(\partial/\partial z)$ is the del operator, and $\nabla \cdot \left(\frac{1}{\rho} \nabla p \right)$ is the divergence of $\left(\frac{1}{\rho} \nabla p \right)$. If density is assumed spatially constant, Eq. (2.7) simplifies to

$$\nabla^2 p - \frac{1}{c^2} \frac{\partial^2 p}{\partial t^2} = 0, \quad (2.8)$$

where ∇^2 is the *Laplacian*, which, in rectangular co-ordinates, is defined as $\nabla^2 = \nabla \cdot \nabla = \frac{\partial^2}{\partial x^2} + \frac{\partial^2}{\partial y^2} + \frac{\partial^2}{\partial z^2}$. Assuming time-harmonic waves where the pressure fluctuates sinusoidally with frequency, application of the Fourier transform to Eq. (2.8) yields the frequency domain form of the wave equation, the Helmholtz equation:

$$[\nabla^2 + k^2]p = 0, \quad (2.9)$$

where k is the wavenumber, defined as the ratio between frequency and sound speed:

$$k = \frac{\omega}{c}. \quad (2.10)$$

The linear homogeneous Helmholtz equations for velocity potential, ϕ , and displacement potential, ψ , are of the same form as Eq. (2.9), and are given by

$$[\nabla^2 + k^2]\phi = 0, \quad (2.11)$$

and

$$[\nabla^2 + k^2]\psi = 0. \quad (2.12)$$

2. LITERATURE REVIEW

2.1.3 Overview of the acoustic Green's function

The general Green's function, G , between two points, \mathbf{r} and \mathbf{r}_0 , is the signal that would be received at one point given a unit impulsive source at the other. It satisfies the inhomogeneous Helmholtz equation:

$$[\nabla^2 + k^2]G(\mathbf{r}, \mathbf{r}_0) = -\delta(\mathbf{r} - \mathbf{r}_0), \quad (2.13)$$

where δ is the Dirac delta function. The general Green's function is therefore fully dependent upon the geometry and environment under consideration, and as such, can be used to determine information about the environment through which acoustic transmission between the two points takes place, in this case the ocean waveguide and the underlying sediment.

Green's function in an unbounded homogeneous medium

Consider an acoustic point source (vibrating sphere) in an unbounded medium as shown in Figure 2.3. A detailed derivation of the Green's function for this configuration is given by Jensen *et al.* [4] (pages 69–73). A summary of the more important concepts and equations is presented here.

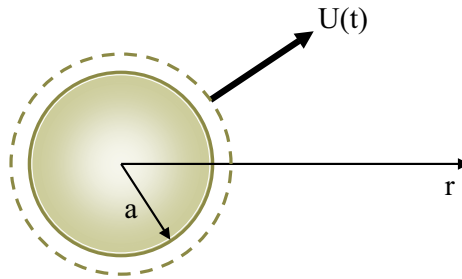


Figure 2.3: Vibrating sphere in an infinite fluid medium (source: MIT OCW [40], adapted from Jensen *et al.* [4]).

For a homogeneous point source in a spherical co-ordinate system, the homogeneous Helmholtz field equation, Eq. (2.12), reduces to

$$\left[\frac{1}{r^2} \frac{\partial}{\partial r} r^2 \frac{\partial}{\partial r} + k^2 \right] \psi(r) = 0, \quad (2.14)$$

which has two linearly independent solutions:

$$\psi(r) = \begin{cases} (A/r)e^{ikr} \\ (B/r)e^{-ikr}, \end{cases} \quad (2.15)$$

where A and B are constants. The two solutions represent outward- and inward-propagating spherical wave solutions respectively, with time dependence $\exp(-i\omega t)$.

Consider a small sphere of radius a with surface displacement $u(t, a) = U(t)$, or in the frequency domain $u(a) = U(\omega)$. The radial displacement of the field is

$$u(r) = \frac{\partial \psi(r, t)}{\partial r}. \quad (2.16)$$

By considering Eq. (2.15) and Eq. (2.16) together, incorporating the surface displacement boundary condition, and using the $ka \ll 1$ approximation, the amplitude of the outward propagating solution to the displacement potential, the first solution of Eq. (2.15), is determined to be $A = -a^2 U(\omega)$. The displacement field becomes

$$\psi(r) = -S(\omega) \frac{e^{ikr}}{4\pi r}, \quad (2.17)$$

where $S(\omega) = 4\pi a^2 U(\omega)$ is the volume source strength.

The Green's function, g , is the field solution, Eq. (2.17), for an impulse input, $S(\omega) = -1$:

$$g(r, 0) = \frac{e^{ikr}}{4\pi r}, \quad (2.18)$$

which, for a source at $\mathbf{r} = \mathbf{r}_0$, generalises to

$$g(\mathbf{r}, \mathbf{r}_0) = \frac{e^{ikR}}{4\pi R}, \quad (2.19)$$

where $R = |r - r_0|$.

Green's function in a homogeneous environment

The Green's function, $g(\mathbf{r}, \mathbf{r}_0)$, of Eq. (2.19) is a particular solution to Eq. (2.13) that satisfies the free-field radiation condition. In a bounded

2. LITERATURE REVIEW

medium such as an ocean waveguide, the general Green's function, G , satisfying Eq. (2.13), is the sum of a particular solution, g , and a homogeneous solution, H :

$$G(\mathbf{r}, \mathbf{r}_0) = g(\mathbf{r}, \mathbf{r}_0) + H(\mathbf{r}), \quad (2.20)$$

where H satisfies the homogeneous Helmholtz equation:

$$[\nabla^2 + k^2]H(\mathbf{r}) = 0. \quad (2.21)$$

Analytical solutions for the general Green's function can be determined for simple environments such as a source in a fluid halfspace [4, 41].

2.1.4 Numerical solutions to the wave equation

Although the wave or Helmholtz equation can be solved theoretically for simple environments such as an acoustic point source in an unbounded medium, numerical models need to be employed to generate a solution for more complex environments. One of four numerical methods are typically used to solve the Helmholtz equation: ray theory, wave number integration, normal modes, and parabolic equation approaches. The time-domain wave equation can be solved using finite differences or finite elements.

The assumptions upon which a numerical method is based determines the complexity of the environment to which it can be successfully applied. Range independent environments are those with environmental parameters that are invariant with range. They are commonly referred to as *horizontally stratified* environments and can be modelled using any of the numerical methods. Range dependent environments are those in which the environmental parameters are not assumed to be constant with range. Only numerical methods that do not assume horizontal stratification can be successfully applied to these more complex environments.

Although many environments can be considered close to horizontally stratified, there exist numerous situations in which this assumption cannot be made. Environments that exhibit significant variations in the sound speed profile as a function of range, such as oceanic fronts, must be treated

as range dependent. Variations in seafloor bathymetry, such as sea mounts, and intrusions of basement material, such as uplifted faults, must also be analysed using a range dependent model.

Ray methods

Ray theory uses ray tracing methods to calculate the transmission loss through the fluid medium. The solution to the Helmholtz equation is assumed to have amplitude and phase components. The surfaces of constant phase are the wavefronts and the normals to these are the rays.

The rays passing through any specific point, termed the *eigenrays*, are a combination of direct rays and those experiencing boundary reflections. The pressure field at a point is the sum of the complex pressures of the eigenrays.

Ray methods use a geometrical acoustic approximation that limits them to the high frequency domain. In general, they are accurate in situations where the acoustic wavelength is smaller than any physical scale in the problem.

Although conceptually simple, ray methods are mathematically complex and hence 1-Dimension or 2-Dimension versions are generally preferred over 3-Dimension versions. The theory can be applied to range dependent applications using various range-partitioning techniques as discussed in the literature [5].

Ray methods experience difficulties in the vicinity of shadow zones and caustics, which are formed due to the refractive properties of the ocean environment focussing a number of adjacent rays into very close proximity. To eliminate the difficulties resulting from this, Gaussian beam tracing, which incorporates beamwidth and curvature equations, can be used [42, 43]. Shadow zones are regions through which no real-valued eigenrays pass; however, in practice sound will still pass through these regions. To overcome this anomaly, complex eigenrays need to be accounted for in the problem. Ray models assume specular reflection with a certain bottom reflection loss.

2. LITERATURE REVIEW

In reality the seafloor is not specular. Sound may be scattered, absorbed, refracted, attenuated, and then transmitted back into the water column at another location. Modifications to basic ray theory need to be made to overcome this [4, 5].

The advantages of ray models over other forward modelling techniques are that they are quick, intuitive, and ideal for obtaining arrival structure information, which is important for computing the directionality of ambient noise. The main disadvantage is that they are difficult to accurately apply to low frequency situations.

Wavenumber integration techniques

Wavenumber integration is a numerical implementation of the integral transform technique for range independent media [4]. The assumption of range independence means that the coefficients of the Helmholtz equation and the boundary conditions will be independent of the range coordinates. The dimensions of the wave equation and boundary conditions can therefore be reduced through use of integral transforms (separation of variables), yielding the *depth-separated wave equation*. Numerous different quadrature schemes for solving the depth-separated wave equation, such as direct trapezoidal integration, with varying degrees of versatility and numerical stability, exist. Jensen *et al.* [4] discusses the more common schemes in detail.

Wavenumber integration has the advantages of being accurate in the near field and valid at all frequencies. The main disadvantages are that it is computationally inefficient to apply to range-dependent environments, and correct application of the technique requires considerable user expertise.

Normal modes

The normal mode method has the same mathematical basis as wavenumber integration. The difference is that an unforced version of the depth-separated wave equation is initially assumed [4]. The unforced equation

has a set of resonant modes, analogous to the modes of vibration of a simple beam. The modes are characterised by a mode shape function, an eigenfunction, and a propagation constant analogous to a beam resonance frequency, an eigenvalue. Taking the source pressure into account, the complete acoustic field is constructed by summing the contributions of each mode (sum of the residues), weighted in accordance with the source depth. The accuracy of the solution is strongly dependent on the number of modes assumed for computational purposes, and hence a number of modes sufficient to achieve solution convergence should be used. Extension of the normal modes method to range dependent problems can be achieved through mode coupling, which is computationally demanding, or through adiabatic approximation [5].

Normal modes have the advantage of computational efficiency and high accuracy at low frequencies. Their main disadvantage is that they are not completely accurate for near field computations.

Parabolic equations

The implementation of parabolic equations is the most popular method for solving range dependent underwater propagation problems [4]. The Helmholtz equation, Eq. (2.9), is rewritten in cylindrical co-ordinates:

$$\frac{\partial^2 p}{\partial r^2} + \frac{1}{r} \frac{\partial p}{\partial r} + \frac{\partial^2 p}{\partial z^2} + k_o^2 n^2 p = 0, \quad (2.22)$$

where $k_o = \omega/c_o$ is the reference wavenumber and $n = c_o/c$ is the refraction index. A solution of the form

$$p(r, z) = \Psi(r, z) S(r), \quad (2.23)$$

is assumed, where $\Psi(r, z)$ is an envelope function and S is a range dependent function. The assumed solution is substituted back into Eq. (2.22) and separation of variables is applied, yielding

$$\frac{\partial^2 S}{\partial r^2} + \frac{1}{r} \frac{\partial S}{\partial r} + k_o^2 S = 0, \quad (2.24)$$

2. LITERATURE REVIEW

and

$$\frac{\partial^2 \Psi}{\partial r^2} + \left(\frac{1}{r} + \frac{2}{S} \frac{\partial S}{\partial r} \right) \frac{\partial \Psi}{\partial r} + \frac{\partial^2 \Psi}{\partial z^2} + k_o^2 n^2 \Psi - k_o^2 \Psi = 0. \quad (2.25)$$

Equation 2.24 is a first order Bessel equation, the solution of which is a first order Hankel function:

$$S = H_o^{(1)}(k_o r). \quad (2.26)$$

Using a far-field approximation, $k_o r \gg 1$, Eq. (2.26) simplifies to

$$S \approx \sqrt{\frac{2}{\pi k_o r}} e^{i(k_o r - \pi/4)}. \quad (2.27)$$

Substituting Eq. (2.27) into Eq. (2.25) and simplifying yields

$$\frac{\partial^2 \Psi}{\partial r^2} + 2ik_o \frac{\partial \Psi}{\partial r} + \frac{\partial^2 \Psi}{\partial z^2} + k_o^2 n^2 \Psi - k_o^2 \Psi = 0. \quad (2.28)$$

Introducing the paraxial approximation, which assumes that the contribution from the second radial partial derivative is negligible, yields the *standard parabolic equation*:

$$2ik_o \frac{\partial \Psi}{\partial r} + \frac{\partial^2 \Psi}{\partial z^2} + k_o^2 (n^2 - 1) \Psi = 0. \quad (2.29)$$

The parabolic equation can be applied to range dependent environments. It has the computational advantage over the elliptic reduced wave equation in that it is a one-way wave equation that can be solved by a highly efficient range-marching solution technique using a range step greater than the acoustic wavelength. The main disadvantage of parabolic equations is that their application requires considerable user expertise.

Numerous different numerical means of solving the parabolic equation exist. These are discussed in detail in the literature [4, 5, 44, 45]. Standard parabolic equation methods have an intrinsic problem with energy conservation. Energy loss can occur in propagation up a positive slope, whilst energy gain can occur in propagation down a slope. This is due to the slope being considered as a finite number of horizontally stratified segments, with discontinuous boundaries. To overcome the energy conservation problem either the interface conditions need to be selected carefully, or a direct sloping-boundary condition can be implemented [46].

Finite differences and finite elements

Finite differences and finite elements are usually implemented in the time domain. The finite difference method discretises the inhomogeneous wave equation in space and time. The finite element method discretises the environment into regions within which the inhomogeneous wave equation can be solved analytically, resulting in a linear system of equations. Both methods, which are geometrically flexible, can provide highly accurate solutions, as generality is not sacrificed through assumptions and approximations. If a pulse source is assumed, the energy partitioning of the wave field, that is, the form and location of the acoustic energy, can be determined as a function of time [47]. From this, insight into the physical propagation effects can be obtained. An excessively large computation effort is required. The field coefficients at each grid point into which the governing wave equation (finite differences) or physical domain (finite elements) is discretised, are stored in matrices, which tend to be large, and it is the inversion of these large matrices that requires intensive computation. Finite differences and elements are therefore usually just used for providing benchmark solutions to a problem.

Numerical solutions used in this thesis

Ray tracing and wavenumber integration are the two numerical techniques for solving the acoustic wave equation used in this thesis. Bellhop [48] ray tracing software is used for path visualisation because ray tracing is fast, intuitive, and the results are easily visualised. The environments considered here are assumed range independent and propagation is over a short range and wide frequency band. OASES (*Ocean Acoustics and Seismic Exploration Synthesis*) wavenumber integration software [49] was therefore considered ideal for all other modelling.

2.2 Literature review on Green's function extraction

Within this section the theory of cross-correlation is introduced. The earliest works showing that the Green's function between two points can be determined from their temporal cross-correlation are described in Section 2.2.1, and the theory of why this is true is presented in Section 2.2.2 for cross-correlations in a uniform homogeneous medium. Further inter-disciplinary works in Green's function extraction are then reviewed in Section 2.2.3.

A conceptual argument relating the cross-correlation of surface sources to the Green's function between two points in a waveguide is presented in Section 2.2.4. This chapter concludes with Section 2.2.5, a discussion of recent literature describing Green's function approximation from cross-correlations of sound in the ocean.

2.2.1 Early research on Green's function extraction from cross-correlations

It was shown theoretically many years ago [50, 51] that under certain conditions the auto-correlation of an earthquake seismogram mimics the echo of an explosive at the correlation location. From this theory, it was hypothesised that the cross-correlation of noise traces at two different locations was related to the Green's function between these locations [52]. Before this was conclusively shown on Earth, Duvall Jr *et al.* [53] showed that time-distance information could be extracted from temporal cross-correlations of the intensity fluctuations on the solar surface. Farrar and James III [54] related the cross-correlation of two response measurements on an ambiently excited structure to the Green's function of the system.

2.2.2 Conceptual description of cross-correlations in a uniform homogeneous medium

Temporal correlation is a measure of the degree of similarity between two signals as a function of time. The comparison of a signal with a time-lagged version of itself is termed *auto-correlation*, while the comparison of two different signals is termed *cross-correlation*.

It has been shown [13, 16, 55] that for a homogeneous medium with sound speed c , the cross-correlation of a uniformly distributed broadband sound field recorded at two receivers separated by distance L , is continuous for $|t| < L/c$, noncontinuous at $t = \pm L/c$, and zero for $|t| > L/c$. A graphical explanation of this is presented here.

The cross-correlation of signals recorded at receivers A and B , as a function of time delay τ , is defined as

$$C_{AB}(\tau) = \int_{-\infty}^{\infty} P(\mathbf{r}_A, t)P(\mathbf{r}_B, t + \tau)dt, \quad (2.30)$$

where P is pressure, \mathbf{r}_A and \mathbf{r}_B are the locations of receivers A and B with respect to an origin, and t is time. The free-field cross-correlation of a broadband signal from an impulse source at location \mathbf{r}_s will therefore be an impulse at time delay

$$\tau = \frac{|\mathbf{r}_B - \mathbf{r}_S| - |\mathbf{r}_A - \mathbf{r}_S|}{c} \leq \frac{L}{c}. \quad (2.31)$$

Sources that yield a cross-correlation at the same time delay therefore lie on a hyperbola with its focus at one of the receivers and its asymptotes intersecting mid-way between the receivers.

The cross-correlations from various source impulse locations are shown in Figure 2.4. The source/receiver geometries are shown on the left with their corresponding cross-correlations to the right according to the following: (a) a source impulse from anywhere along the line perpendicular to the A - B axis, and equi-distant from A and B , will be received at both A and B simultaneously; and (b) the cross-correlation will therefore yield an impulse with zero time delay. In (c) a source located on the A - B axis closer

2. LITERATURE REVIEW

to A and external to the sources is received at B at a time L/c after it is received at A and hence yields (d) a cross-correlation at $\tau = L/c$. In (e) any other source that is received at A prior to B yields (f) a cross-correlation at a time delay of $0 < \tau = (L - 2(|A| - |x|))/c < L/c$. In (g) summation of cross-correlations from sources that span the region from $\tau = 0$ through $\tau = L/c$ yields (h) a boxcar function. In (i) inclusion of sources that are received at B before A (j) fills in the acausal side of the cross-correlation. Figure 2.4 only shows sources on a semi-ellipse, but due to symmetry a full ellipse produces an identical response.

The boxcar function and its derivative

$$\frac{dC}{dt} = -\delta(t - L/c) + \delta(t + L/c), \quad (2.32)$$

are shown in Figure 2.5. The cross-correlation derivative is seen to be proportional to the sum of the causal and acausal Green's functions:

$$\frac{dC}{dt} = -G(t) + G(-t). \quad (2.33)$$

Realistically a band-limited signal is recorded and correlated. A 0.05–0.2 Hz filtered cross-correlation and its time derivative are also shown in Figure 2.5. Note that the cross-correlation rapidly drops to near zero at times less than the inter-receiver travel time. The band-limited signal does not have a zero-frequency component and therefore the phase characteristics result in peaks in the cross-correlation that do not correspond to peaks in the Green's function destructively interfering with one another. The band-limited cross-correlation time derivative has a waveform like structure. The peak of this occurs at the same time as for the simplified broadband case. An isotropic noise distribution yields a symmetric cross-correlation; a one-sided distribution would give an approximation of only the causal Green's function.

The general relationship between the cross-correlation function and the Green's function is

$$-\frac{dC}{dt} \simeq G(t) - G(-t). \quad (2.34)$$

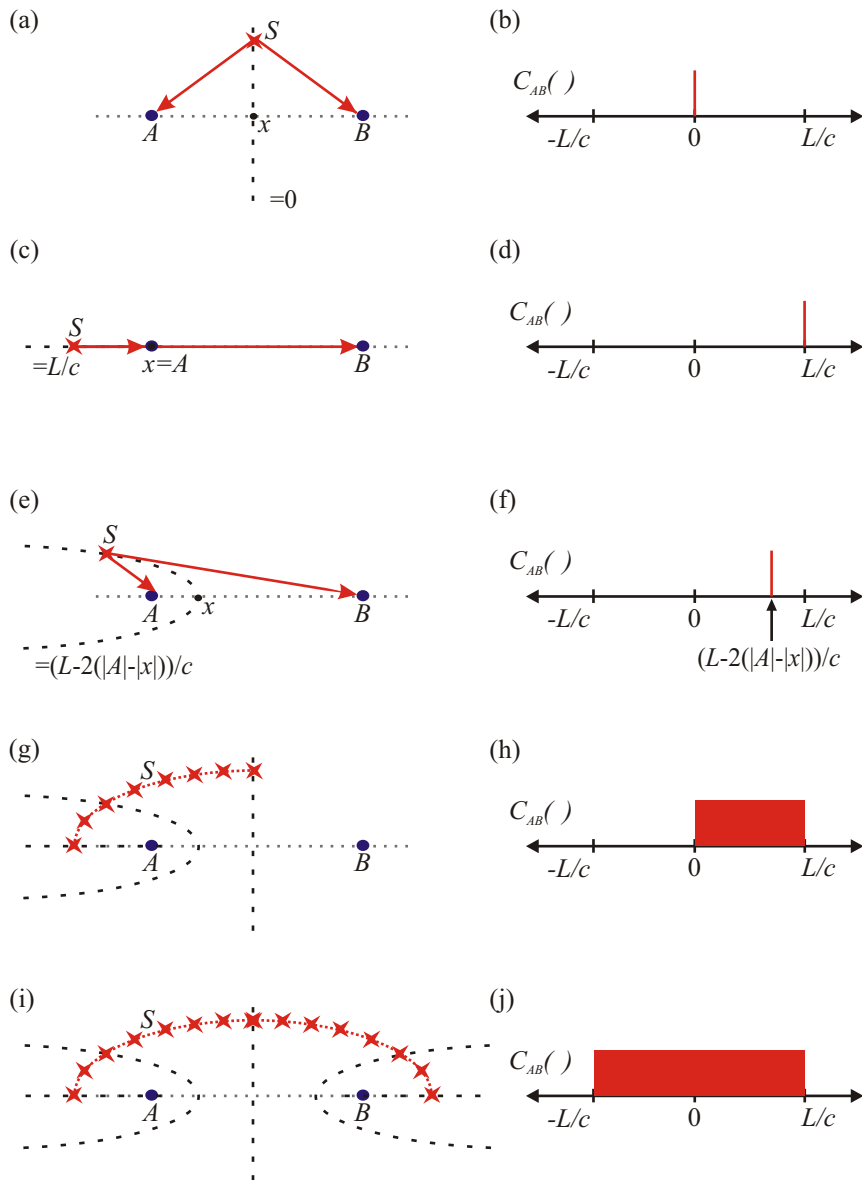


Figure 2.4: Cross-correlation of a source impulse in free space. Figure details are described in the main text.

2. LITERATURE REVIEW

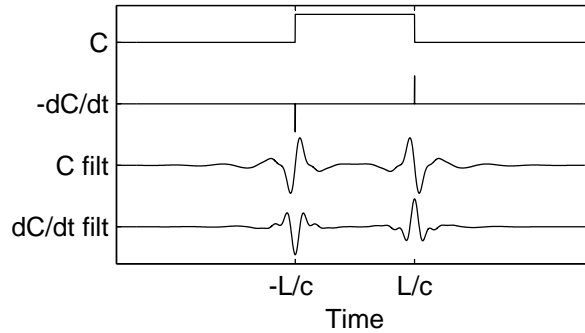


Figure 2.5: Free-field cross-correlation examples. Top to bottom: broadband noise correlation function (NCF), derivative of the broadband NCF, filtered (0.05–0.2 Hz) NCF, and derivative of the filtered NCF (adapted from Gerstoft *et al.* [16]).

Equality is not absolute in Eq. (2.34). Reasons for this will be discussed in Section 3.1.1.

2.2.3 Interdisciplinary review of Green’s function extraction from cross-correlations

Approximation of the Green’s function between two points in both open and closed environments has been more widely studied since Lobkis and Weaver [7] showed, both theoretically and experimentally, that an approximation of the Green’s function between two points can be determined from their temporal cross-correlation within a diffuse ultrasonic field. Their experimental arrangement and results, as shown in Figure 2.6, are briefly described here as they provide a simple explanation of the general concepts governing the extraction of Green’s functions from noise cross-correlations. A broadband (0.1–0.9 MHz) ultrasonic impulse was input to an aluminium block at point \mathbf{s} . Due to the irregular block shape, a long-time pseudo-diffuse field was created. The pseudo-diffuse field was measured at two receivers, \mathbf{x} and \mathbf{y} , and cross-correlated. The cross-correlation was then compared to the Green’s function between receivers \mathbf{x} and \mathbf{y} , obtained by measuring the signal received at \mathbf{y} from an impulsive input source at \mathbf{x} .

The cross-correlated field and the Green's function show good agreement, but there are discrepancies, particularly in amplitude.

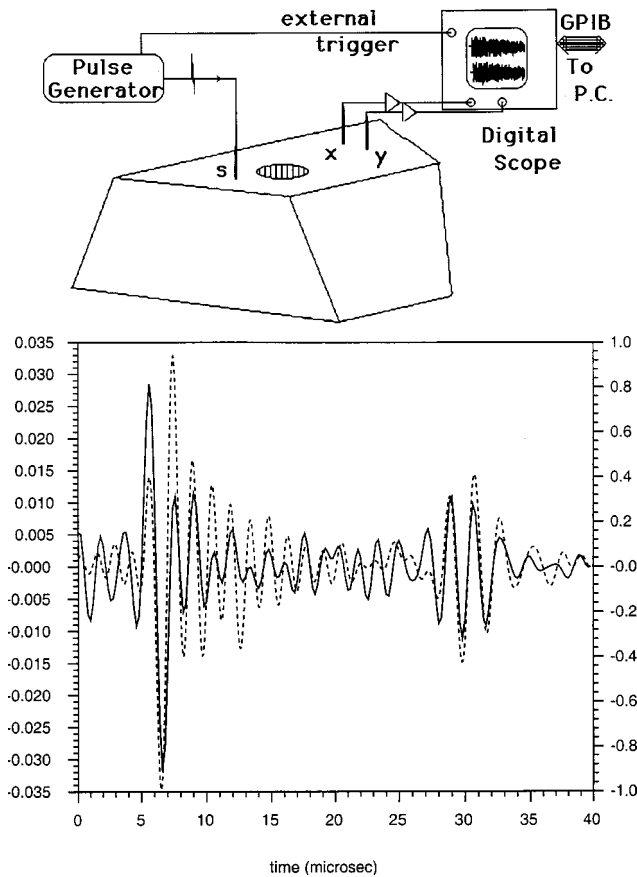


Figure 2.6: (top) Impulse source creates pseudo-diffuse field in a block, which is detected at receivers x and y ; (bottom) the cross-correlation of the signals (solid line) is compared to the signal (dashed line) which would be received at y given an impulse source at x (source: Lobkis and Weaver [7]).

A *diffuse* field is one in which the modal amplitudes are uncorrelated random variables. Although the block specimen was irregular, it was not lossless, and hence a source input at only one location would not precisely satisfy the diffuse field requirement, explaining why only a *pseudo-diffuse* field was created experimentally. The theory of Lobkis and Weaver explained how the relationship between the cross-correlation and Green's function is dependent upon the work done by the source on each mode, and hence am-

2. LITERATURE REVIEW

plitude equality will not be obtained if the diffuse field requirement is not met. They showed that increased temporal averaging and increased spatial averaging through the use of multiple source locations results in a field that more closely satisfies the diffuse field requirement, and therefore decreases the discrepancies between the cross-correlation and the Green's function.

The concepts of Lobkis and Weaver [7] were extended by Derode *et al.* [56] who showed that the Green's function can be conditionally recovered in an open scattering medium. They concluded that although the Green's function can be determined from cross-correlations from a single source within a lossless closed cavity in which it is assumed that the eigenmodes do not degenerate, the Green's function will only emerge from cross-correlations within an open scattering medium if they are summed over a perfect time-reversal mirror. Wapenaar [57] and Van Manen *et al.* [58] demonstrated that retrieval of the Green's function through summed cross-correlations can also be achieved in an inhomogeneous medium.

Extraction of the Green's function by cross-correlation has been applied to practical applications not just in helioseismology, structural engineering and ultrasonics, but also in other fields. In addition to the works of Lobkis and Weaver [7] and Derode *et al.* [56], numerous other significant contributions in cross-correlations of ultrasonic diffuse wavefields exist [8–10, 59]. Extensive studies on cross-correlations of ambient seismic noise have been presented [12–15, 17–19, 60, 61]. Curtis *et al.* [28] published an extensive review paper on seismic noise cross-correlation, and Bensen *et al.* [62] included a comprehensive review and comparison of existing seismic noise data processing techniques in their work. Green's function estimates from noise have also been applied to structural health monitoring [63], moon seismic noise [20], and human skeletal muscle noise [21].

2.2.4 Conceptual description of cross-correlations in a simplified isovelocity ocean waveguide

In its most general form the ocean can be considered as a waveguide bounded by a free-surface above and the seafloor below. If spreading and attenuation losses are ignored, an impulse source signal at location A will be recorded at a second location B as an infinite set of impulses at time lags that correspond to the acoustic travel paths between A and B . Consider the first three arrivals only: the direct path, surface reflected path, and bottom reflected path. The order of arrival of the latter two depends upon the locations of A and B . These three paths and the corresponding arrivals recorded at B are shown in Figure 2.7(a).

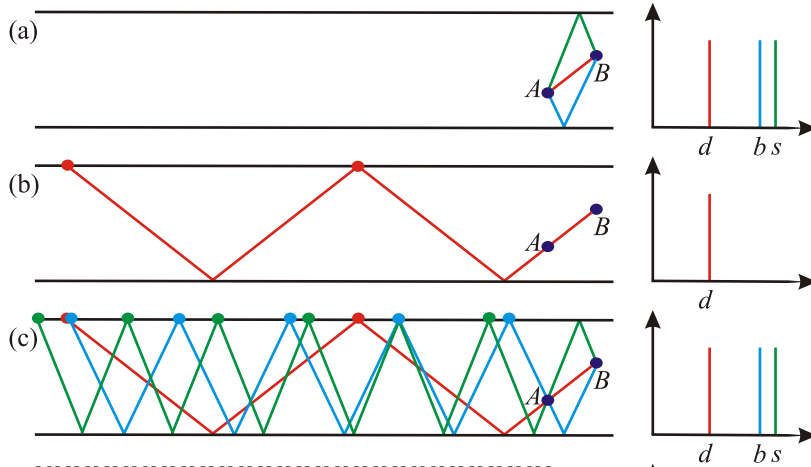


Figure 2.7: Waveguide without losses. (a) Green's function between receivers A and B showing direct (red), surface reflected (green), and bottom reflected (blue) paths with corresponding Green's function shown to the right. (b)–(c) Surface sources that yield (b) direct path, and (c) direct and single reflected paths, with corresponding cross-correlations shown at the far-right (adapted from [64]).

The ocean sound field is dominated by sources at or near the surface. Surface sources that are received by both A and B with a lag time equal to the direct path travel time are shown in Figure 2.7(b). Note that for the lag time to be correct, the ray path from the sources must pass through both

receivers. The cross-correlation of these sources at A and B is an impulse at the direct path arrival time. All surface sources that contribute to the first three arrivals are shown in Figure 2.7(c).

The sources that sum constructively in the Green's function approximation do not span the ocean surface uniformly. If ocean surface noise is assumed to be uniform in generation, signals from sources whose paths do not contribute to Green's function time lags will be recorded and correlated. These cross-correlations would, by themselves, yield an arrival at an incorrect time; however, if a uniform band-limited source field exists, all of the cross-correlations from source signals that do not pass through both receivers cancel due to destructive phase interference. The finer mathematical details of why this occurs are too extensive to present here; however, a detailed stationary-phase theoretical explanation of this concept is presented in Sections 3.1.1, 3.1.2, and 3.1.3.

2.2.5 Review of Green's function extraction from cross-correlations in the ocean

Realistic ocean environments are far more complex than the generalised environment considered in Section 2.2.4. Refraction within the water column and at the water-sediment interface, spreading and attenuation losses, and uneven source distributions, mean that Green's function approximation is not as straightforward as the conceptual argument presented here may suggest. Several papers that have investigated important concepts relating cross-correlations in realistic ocean environments are discussed here.

Roux and Fink [29] showed theoretically and through simulation that the Green's function between two points can be determined by summing either the cross-correlations from a vertical line of sources that are located in the same plane as the two receivers, external to the two receivers, or from summing the convolution of the signals received from a vertical line of sources located co-planar between the two receivers. Their theory is based upon three main assumptions: the medium of interest is reciprocal

(i.e., fluctuations of the signal due to changes in the channel environment, such as currents or internal waves, can be assumed to be negligible); modal orthogonality holds (i.e., the water column contains sufficient sources that span the entire water column and density gradients are negligible); and the modal continuum of the acoustic bottom can be neglected (i.e., the range between the two receivers is sufficiently large). Using time-reversal, they compared back-propagated fields generated by the estimated Green's function with those generated by the exact Green's function and concluded that for both range independent and range dependent environments:

- the size and location of the focal point is virtually independent of source spacing;
- the spatial and temporal side-lobes within the back-propagated signal are suppressed sufficiently if the depth between successive sources is not greater than the smallest wavelength of the source spectrum;
- the focal spot is distorted if the sources do not span the entire water column;
- if there are insufficient sources, modal orthogonality does not hold and the estimated Green's function is erroneous in both phase and amplitude; and
- even if there are sufficient sources within the water column, the phase term of the estimated Green's function will be correct, but the amplitude term will remain erroneous.

Sabra *et al.* [15] presented theory and simulations demonstrating the relationship between time-averaged cross-correlations of noise generated at the sea surface by wave processes, and the Green's function between two hydrophones. Sabra *et al.* [27] also correlated noise from 150–700 Hz experimental noise data. Their sound field was dominated by croaker fish rather than surface generated noise, but due to the near isotropic distribution of the fish, they were able to obtain good estimates of the direct path travel

2. LITERATURE REVIEW

times between elements of a bottom mounted hydrophone array. They used these times to perform array self-localisation and self-synchronisation.

Using a vertical array of hydrophones, ocean noise cross-correlation has been used to approximate seafloor structure via passive fathometry [65, 66]. If the noise source is assumed to be completely uncorrelated surface noise, the estimated layer profile has been shown to have amplitudes that are proportional to those of an echo sounder at the same depth as the array [67].

Roux *et al.* [25] theoretically investigated the relationship between the time-averaged cross-correlation function and the Green's function for volume and surface sources as well as shipping noise. Their simulations of the cross-correlation function for the surface noise model agreed with the temporal structure of the Green's function. Roux *et al.* [25] also showed experimentally that if sufficiently long cross-correlation time windows are used, for a single ship track passing through the end-fire plane, which is defined as the plane containing the hydrophone array, of a pair of hydrophones, the signal from the end-fire location dominates the cross-correlation function. They presented simulations for sources located at various distances along the end-fire direction from the hydrophones and showed that the resulting summed cross-correlation peaks emphasised different parts of the Green's function, depending on the source range. From this they concluded that if a sufficiently large collection of random events is recorded, the structure of the complete Green's function can be obtained.

The works described in this section all further the understanding of Green's function extraction from ocean noise cross-correlation. The gaps in the literature identified in Section 1.1 are not due to weaknesses in previous works, rather the field of ocean acoustic interferometry is young, and many ideas have therefore yet to be fully explored.

Chapter 3

Active Source Ocean Acoustic Interferometry Theory

Using a stationary phase argument, this chapter explores the relationship between cross-correlations from active source configurations to two receivers within a waveguide, and the time domain Green's function between the two receivers. This approach is termed active source ocean acoustic interferometry (OAI), as it is related to classical and seismic interferometry [28], where interferometry refers to the determination of information from the interference phenomena between pairs of signals. The theoretical formulations and simulations presented here provide a basis for understanding active source OAI, and will be useful for explaining experimental results in Chapter 6.

The method of stationary phase is applied to simple reflective water column environments, providing an alternative theoretical means of describing and understanding the physics governing the cross-correlation of such a source configuration, and how this can be used to extract an amplitude shaded time domain Green's function (i.e., a Green's function convolved with amplitude factors). This work is distinct from work presented by Roux and Fink [29], Sabra *et al.* [15], and Snieder *et al.* [30], in that a stationary phase derivation is applied here to a vertical column of sources in a waveguide. A detailed physical and mathematical discussion of spurious ar-

rivals obtained in connection with OAI is presented. Numerical simulations of these environments support the theory. A refractive environment with more realistic water column, sediment, and bottom parameters is also analysed through numerical simulations. Although these geometrically simple scenarios are chosen as they allow for easier understanding of the results, the underlying concepts are also applicable to complex environments. Both the unstacked (unsummed) cross-correlations as a function of depth and the stacked (summed over depth) cross-correlations are analysed. The effect of limiting the sources to the water column is discussed and it is shown that the accuracy of OAI increases if the source column is extended through the sediment. The spurious arrivals obtained here are compared with those obtained by Sabra *et al.* [15] and Snieder *et al.* [30]. The manifestation of these aberrations are distinct in each case and these differences are explained by considering the different environments and geometrical set-up used in each case.

Three specific source configurations are introduced and explained: vertical source column, horizontal straight line towed source, and horizontal hyperbolic towed source.

A significant proportion of the work in this chapter has been published by the author in a 2007 journal paper [26].

3.1 Vertical source column

Consider the waveguide depicted in Figure 3.1. The x , y and z directions are defined as the horizontal axis, the axis in-and-out of the page, and the vertical axis, respectively. A vertical plane of sources spanning the water column (i.e., the z -direction) and extended towards infinity in the y -direction, and spaced sufficiently close to one another such that the highest-order mode that significantly contributes to the Green's function is sufficiently sampled, would form a perfect time-reversal mirror, meeting the requirements for determination of the Green's function between two points via cross-correlation

methods [29, 56]. However, it has previously been shown that only sources in the end-fire plane, that is, the same vertical plane as the two receivers (in Figure 3.1 this is the plane of the page), will contribute significantly to the cross-correlation

An expression for the cross-correlations of the signals received at two locations A and B , from a vertical column of sources, has previously been derived by Snieder *et al.* [30]. A summary of this derivation, adapted to the geometry being considered, is presented here. The signals from a set of sources received at A and B are

$$\begin{aligned} u_A(\omega) &= \sum_S \rho_s G(\mathbf{r}_A, \mathbf{r}_S) S_S(\omega) \\ u_B(\omega) &= \sum_{S'} \rho_{s'} G(\mathbf{r}_B, \mathbf{r}_{S'}) S_{S'}(\omega), \end{aligned} \quad (3.1)$$

where ρ_s is the density of the acoustic medium, in this case the water column, at the source, S , $G(\mathbf{r}_\psi, \mathbf{r}_S)$ is the full Green's function between the source and receiver ψ , where $\psi = A$ or B , and $S_S(\omega)$ and $S_{S'}(\omega)$ are complex frequency source spectra of sources S and S' respectively. Cross-correlating the two expressions in Eq. (3.1) yields

$$C_{AB}(\omega) = \sum_{S, S'} \rho_s \rho_{s'} G(\mathbf{r}_A, \mathbf{r}_S) G^*(\mathbf{r}_B, \mathbf{r}_{S'}) S_S(\omega) S_{S'}^*(\omega), \quad (3.2)$$

where $*$ denotes the complex conjugate. If it is assumed that the sources are uncorrelated, the cross-terms, $S \neq S'$, equate to zero, and hence Eq. (3.2) simplifies to

$$C_{AB}(\omega) = \sum_S \rho_s^2 G(\mathbf{r}_A, \mathbf{r}_S) G^*(\mathbf{r}_B, \mathbf{r}_S) |S(\omega)|^2. \quad (3.3)$$

For a vertical line of sources that is uniformly distributed (source spacing $\leq \lambda_{min}$) within the vertical plane containing receivers A and B , external to the two receivers, and closer to B , the cross-correlation becomes:

$$C_{AB}(\omega) = |\rho_s S(\omega)|^2 n \int_0^D G(\mathbf{r}_A, \mathbf{r}_S) G^*(\mathbf{r}_B, \mathbf{r}_S) dz, \quad (3.4)$$

where n is the number of sources per unit length. The lower bound of the integral is 0 since the waveguide has a free surface at $z = 0$ and the upper

3. ACTIVE SOURCE OCEAN ACOUSTIC INTERFEROMETRY THEORY

bound is the waveguide depth, D , since there are no reflective surfaces below this depth. This summed cross-correlation can, in the time domain, be determined from real or simulated data by calculating the cross-correlation for each source depth and then summing (also known as ‘stacking’) the result. The sum of the cross-correlations is related to the Green’s function between A and B . This relationship is derived here for reflective environments using the method of stationary phase [68].

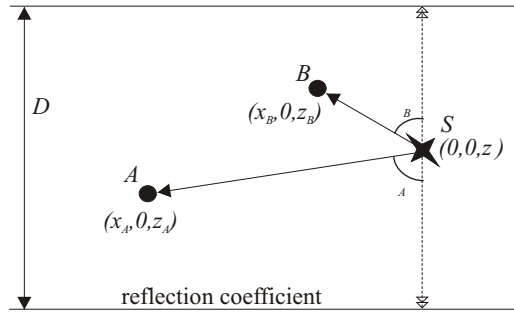


Figure 3.1: Source-receiver geometry and notation: the source S is located at $(0, 0, z)$, and receivers A and B are located at $(x_A, 0, z_A)$ and $(x_B, 0, z_B)$ respectively within a waveguide of depth D .

The 3D Green’s function within a homogeneous medium is [4]

$$G_f(R) = \frac{e^{ikR}}{4\pi R}, \quad (3.5)$$

where k is the wave number and R is the distance from the source. The full Green’s function at each receiver can be written as the superposition of the direct and reflected waves. If the medium is an isovelocity waveguide, bounded above by a free surface and below by a reflective bottom with amplitude reflection coefficient Γ , the Green’s function between the source, S , and receiver, ψ , is written in terms of the waveguide and source-receiver geometry [1] as

$$G(\mathbf{r}_\psi, \mathbf{r}_S) = \sum_{b_\psi=0}^{\infty} \Gamma^{b_\psi} G_f \left(\sqrt{x_\psi^2 + (2b_\psi D + z \pm z_\psi)^2} \right) + \sum_{b_\psi=1}^{\infty} \Gamma^{b_\psi} G_f \left(\sqrt{x_\psi^2 + (2b_\psi D - z \pm z_\psi)^2} \right), \quad (3.6)$$

where b_ψ is the number of bottom bounces for a given path, and D is the depth of the waveguide. The first term on the RHS includes all up-going waves and the second term includes all down-going waves as measured from the source.

Inserting Eq. (3.6) into the summed cross-correlation, Eq. (3.4), yields an expression for the cross-correlation that consists of the sum of the integrals of all possible combinations of the interaction between any path to the first receiver and any path to the second. Although the cross-correlation includes the sum of all path interactions, each path interaction can be analysed separately and summed together at the end to yield the complete solution. Hence, only one of these individual interactions is considered here. Substitution of Eq. (3.5) into Eq. (3.4) (i.e., cross-correlation between two arbitrary paths), yields, for the integral term:

$$I = \frac{\Gamma^{b_A+b_B}}{(4\pi)^2} \int \frac{e^{ik(L_A-L_B)}}{L_A L_B} dz, \quad (3.7)$$

where b_ψ is the number of bottom bounces for the path to receiver ψ , where $\psi = A$ or B , and $L_\psi = \sqrt{x_\psi^2 + (2b_\psi D \pm z \pm z_\psi)^2}$ is the length of the given path between the source, S , and receiver, ψ . The sign in front of z is positive when the wave departing the source is up-going and negative when it is down-going. Similarly, the sign in front of z_ψ is positive when the wave arriving at the receiver is down-coming and negative when it is up-coming.

3.1.1 Stationary phase evaluation

Consider the integrand of Eq. (3.7). Since $1/(L_A L_B)$ varies slowly and the phase $k(L_A - L_B)$ varies quickly within the region of interest, rapid oscillations of the numerator $e^{ik(L_A-L_B)}$ over the integrand allow for the integral, Eq. (3.7), to be solved via the method of stationary phase [68]. Similar interferometric integrals have been solved by others [13, 15, 30]. Here the idea of Snieder *et al.* [30] is followed, but a vertical rather than horizontal line of sources is assumed, and also the theory is extended to a waveguide.

3. ACTIVE SOURCE OCEAN ACOUSTIC INTERFEROMETRY THEORY

Consider the phase term $k(L_A - L_B)$. The length dependent component, $L_A - L_B$, is the only part that fluctuates over the line integral. The stationary points of the integrand are therefore found by evaluating the partial z derivative of the length dependent part of the phase term, and setting this equal to zero. The source location dependent phase term is

$$\begin{aligned} L &= L_A - L_B \\ &= \sqrt{x_A^2 + (2b_A D + \alpha_A z \pm z_A)^2} \\ &\quad - \sqrt{x_B^2 + (2b_B D + \alpha_B z \pm z_B)^2}, \end{aligned} \quad (3.8)$$

where $\alpha_\psi = 1$ denotes an up-going wave, and $\alpha_\psi = -1$ denotes a down-going wave, as measured from the source. The partial differential of Eq. (3.8) with respect to z is

$$\frac{\partial L}{\partial z} = \alpha_A \left(\frac{2b_A D + \alpha_A z \pm z_A}{L_A} \right) - \alpha_B \left(\frac{2b_B D + \alpha_B z \pm z_B}{L_B} \right). \quad (3.9)$$

Writing Eq. (3.9) in terms of the acute angle between the path and the vertical, ϕ_ψ , at the point of departure from the source (see Figure 3.1), yields

$$\frac{\partial L}{\partial z} = \alpha_A \cos \phi_A - \alpha_B \cos \phi_B. \quad (3.10)$$

Setting the partial z -derivative to zero yields $\phi_A = \phi_B$ when $\alpha_A = \alpha_B$ (i.e., both waves depart as either up-going or down-going), and $\phi_A = \pi - \phi_B$ when $\alpha_A = -\alpha_B$ (i.e., one wave departs as up-going and the other as down-going). Since both ϕ_A and ϕ_B are less than $\pi/2$, the latter equation has no solutions. Thus a stationary point, defined as a point with geometry satisfying $\frac{\partial L}{\partial z} = 0$, will only occur when both signals depart the source at the same angle. Therefore, the path to the further receiver passes through the closer receiver, as shown in Figure 3.2 for four different paths. Remember that the above derivation holds for any single set of path combinations (i.e., it is true for the direct paths to A and B , for the bottom reflected path to B and the bottom-surface-bottom reflected path to A , and for any other two path combinations), but that the cross-correlation includes the sum of all these path combinations. Not all path combinations will exhibit a

stationary point; for example, the direct path (i.e., no reflections) to A and any boundary interacting path to B will never satisfy $\phi_A = \phi_B$ since ϕ_B will always be less than ϕ_A .

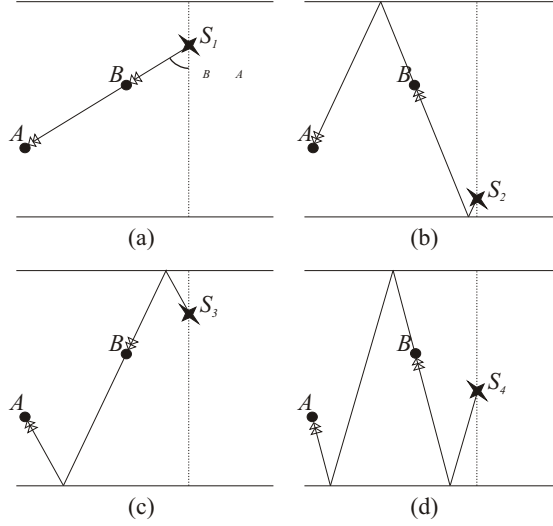


Figure 3.2: Examples of wave paths that correspond to stationary points satisfying $\phi_A = \phi_B = \phi$: (a) direct wave, (b) surface reflected wave, (c) bottom reflected wave, and (d) surface and bottom reflected wave, between the receivers.

The cross-correlation integral, I , Eq. (3.7), can be rewritten within the region of a given stationary point, z_s , as

$$I(z_s) \approx \frac{\Gamma^{b_A+b_B}}{(4\pi)^2} \frac{1}{L_A(z_s)L_B(z_s)} \int_{-\infty}^{\infty} e^{ik(L_A(z)-L_B(z))} dz. \quad (3.11)$$

Realistically, the sources exist over the finite limit $(0, D)$; however, extension of these limits to infinity is valid as virtual sources exist over an infinite limit. The phase term can be approximated as a truncated Taylor series within the neighbourhood of any stationary point:

$$L(z) \approx L(z_s) + \frac{(z - z_s)^2}{2} \left(\frac{\partial^2 L}{\partial z^2} \Big|_{z=z_s} \right), \quad (3.12)$$

with

$$\frac{\partial^2 L}{\partial z^2} \Big|_{z=z_s} = \sin^2 \phi_s \left(\frac{1}{L_A(z_s)} - \frac{1}{L_B(z_s)} \right), \quad (3.13)$$

3. ACTIVE SOURCE OCEAN ACOUSTIC INTERFEROMETRY THEORY

where $\phi_s = \phi_A = \phi_B$ is the acute (relative to the vertical) departure angle from the source at the stationary point, z_s . Since Eq. (3.12) is evaluated in the region of a stationary point, which is defined as a location where $\frac{\partial L}{\partial z} = 0$, the first order term in the Taylor expansion is also equal to zero. Substituting the phase term and its second derivative, at the stationary point, into the truncated Taylor series, Eq. (3.12), and rewriting the integral, Eq. (3.11), assuming that $L_A(z_s) > L_B(z_s)$ (which is valid since the source is closer to B than to A), yields

$$I(z_s) = \frac{\Gamma^{b_A+b_B} e^{ik(L_A(z_s)-L_B(z_s))}}{(4\pi)^2 L_A(z_s)L_B(z_s)} \times \int_{-\infty}^{\infty} \exp\left(-ik\frac{(z-z_s)^2}{2}\xi \sin^2 \phi_s\right) d(z-z_s), \quad (3.14)$$

where $\xi = \frac{L_A-L_B}{L_AL_B} = \frac{1}{L_B(z_s)} - \frac{1}{L_A(z_s)}$ is the ratio of the difference in path lengths to their product. The term outside the integral takes into account the path lengths and reflection coefficients for the stationary point, and the term inside the integral accounts for the propagation variation in depth relative to the stationary point depth. Equation (3.14) is a Fresnel integral and can therefore be solved by making the substitution $k\frac{(z-z_s)^2}{2}\xi \sin^2 \phi_s = \frac{\pi}{2}\tau^2$:

$$\begin{aligned} I(z_s) &= \frac{\Gamma^{b_A+b_B} e^{ik(L_A(z_s)-L_B(z_s))}}{(4\pi)^2 L_A(z_s)L_B(z_s)} \\ &\quad \times 2\sqrt{\frac{\pi}{k\xi \sin^2 \phi_s}} \int_0^{\infty} \exp\left(-i\frac{\pi}{2}\tau^2\right) d\tau \\ &= e^{i(3\pi/4)} \frac{\Gamma^{b_A+b_B}}{\sin \phi_s} \sqrt{\frac{\xi}{8k\pi}} G_f(R(z_s)), \end{aligned} \quad (3.15)$$

where $R(z_s) = L_A(z_s) - L_B(z_s)$ is the path length between A and B . Inclusion of the source factor, $n|\rho_s S(\omega)|^2$, from Eq. (3.4), and the relationship

$k = \omega/c$, yields for the cross-correlation between signals at A and B :

$$\begin{aligned}
 C_{AB}(\omega) &= \sum_{z_s} n |\rho_s S(\omega)|^2 I(z_s) \\
 &= e^{i(3\pi/4)} n |S(\omega)|^2 \\
 &\quad \times \sum_{z_s} \left(\frac{\Gamma^{b_A+b_B} \rho_s^2 G_f(R(z_s))}{\sin \phi_s} \sqrt{\frac{\xi c}{8\pi\omega}} \right),
 \end{aligned} \tag{3.16}$$

where the summation is over all stationary points.

The relationship in Eq. (3.16) between the cross-correlation of the signals received from a vertical column of sources located in the same vertical plane as two receivers, $C_{AB}(\omega)$ (LHS), and the Green's function, G_f (RHS), is seemingly complicated. The cross-correlation yields an estimation of an amplitude and phase shaded Green's function (i.e., a Green's function that is multiplied by amplitude and phase dependent weighting coefficients). The phase shading is simply a $3\pi/4$ phase shift. If the summed cross-correlations are multiplied by $e^{-i(3\pi/4)}$, phase information, and hence travel times, of the amplitude shaded Green's function can be determined.

The amplitude shading consists of numerous components:

- constant - inverse source spacing term n , medium density term ρ_s^2 , sound speed term \sqrt{c} , and a $1/\sqrt{8\pi}$ factor;
- path dependent - phase term $\Gamma^{b_A+b_B}$, source departure angle term $\sin \phi_s$, and path length term $\xi = \frac{1}{L_B(z_s)} - \frac{1}{L_A(z_s)}$; and
- frequency dependent - source spectrum term $|S(\omega)|^2$ and frequency factor $1/\sqrt{\omega}$.

Correcting for the constant components is straightforward if the source geometry and medium density and sound speed are known. The frequency dependent terms can be corrected for only if the source spectrum is known. It will, however, be difficult to obtain the correct amplitudes for the path dependent terms since these will be different at each stationary point.

The cross-correlation equation, Eq. (3.16), is in this particular form due to the mismatch between a 3D Green's function and a 1D source distribution, as commented by Snieder *et al.* [30]. If a 2D plane instead of the 1D column of sources were used, Eq. (3.4) would be a double integral spanning both the z and y directions, which could be solved as a product of two stationary phase integrals. If either a 2D plane of sources or the far-field approximation of the 2D Green's function, $G(R) = e^{ikr}/\sqrt{r}$, were incorporated, there would not be a dimensionality mismatch, and the sum of the cross-correlations from all sources, Eq. (3.16), would be

$$\begin{aligned} \tilde{C}_{AB}(\omega) = & -in|S(\omega)|^2 \\ & \times \sum_{z_s} \left(\frac{\Gamma^{b_A+b_B} \rho_s^2 G_f(R(z_s))}{\sin \phi_s} \times \frac{c}{2\omega} \right), \end{aligned} \quad (3.17)$$

where n is the number of sources per unit surface area for the plane of sources or the number of sources per unit length for the column of sources. Note that there is now no term, apart from the Green's function, containing $L_A(z_s)$ and $L_B(z_s)$, and therefore the amplitude shading is only dependent on the travel path through the $\Gamma^{b_A+b_B}$ and $\sin \phi_s$ terms.

Because of the i/ω factor in Eq. (3.17), the time domain Green's function is proportional to the time-derivative of the summed cross-correlations [11, 13, 15]. Due to a mismatch between the source dimensions and the Green's function, the frequency factor is only $1/\sqrt{\omega}$ in Eq. (3.16). Combining the phase and frequency terms gives $e^{-i(3\pi/4)}/\sqrt{\omega} = i/\sqrt{-i\omega}$. This factor can be corrected for with a $\pi/2$ phase shift, and a 0.5 order fractional time derivative [30, 69]. Note that the $e^{-i(3\pi/4)}$ phase multiplication mentioned earlier is incorporated here.

3.1.2 Incorporation of sediment layers

When the water column is bounded by fully reflective boundaries, as assumed for the preceding derivation, all of the energy is contained within the water column and truncation of the cross-correlation integral in Eq. (3.4) is

avoided. The addition of sediment layers can cause truncation errors since the true integral will then extend to infinity, or at least to the basement (the continental or oceanic crust below the sedimentary layers), to account for sound that interacts with the sediment:

$$C_{AB}(\omega) = |\rho_s S(\omega)|^2 n \int_0^\infty G(\mathbf{r}_A, \mathbf{r}_S) G^*(\mathbf{r}_B, \mathbf{r}_S) dz. \quad (3.18)$$

If the source column is restricted to the water, the calculated integral still ceases at D and the stacked cross-correlations yield a poorer estimation of the frequency and phase shaded Green's function. Consider as an example a purely theoretical reflective environment, with constant sound speed, consisting of a water column and M sediment layers. The length of any path between the source, S , and receiver, ψ , becomes

$$L_\psi = \sqrt{x_\psi^2 + \left(2pD + \sum_{m=1}^M (2q_m D_{sm}) \pm z \pm z_\psi\right)^2}, \quad (3.19)$$

where p and q_m are the multiple order (the number of reflections off the bottom of the layer plus the number of refractions into the layer from below) in the water and each sediment layer, m , and D_{sm} is the depth of the m^{th} sediment layer. The stationary phase condition is still $\phi_A = \phi_B$; however, there exist paths satisfying this condition whose path length differences are not identical to any of the Green's function path lengths, direct or otherwise, between the two receivers. For example, in Figure 3.3(a) the path to receiver B is a reflection from the sediment-water interface. The path to receiver A is a transmission through this interface, a reflection from the basement and a transmission back into the water. The stationary phase condition of $\phi_A = \phi_B$ is satisfied; however, the path length difference is

$$L = \sqrt{x_A^2 + (2D + 2D_s - z - z_A)^2} - \sqrt{x_B^2 + (2D - z - z_B)^2}, \quad (3.20)$$

which, in general, differs from the path length of any wave that travels between the two receivers, and therefore should not contribute to the Green's

3. ACTIVE SOURCE OCEAN ACOUSTIC INTERFEROMETRY THEORY

function. The arrival due to this stationary point is therefore called a ‘spurious’ arrival. Note that the path length difference and hence the time at which spurious arrivals occur is dependent on the horizontal distance separating the source column from the receivers. If the column of sources, S , were extended into the sediment (sources in the sediment are denoted S'), a second stationary point would exist, as shown in Figure 3.3(b), cancelling the contribution of the water-source stationary point.

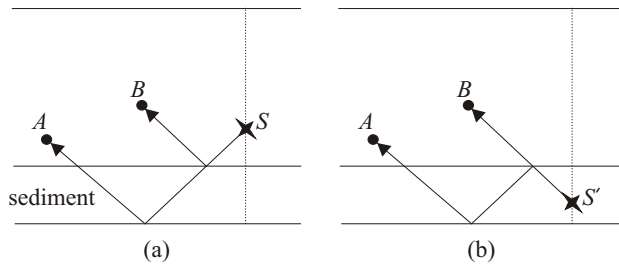


Figure 3.3: Example of (a) water source, S , and (b) sediment source, S' , stationary points that have the same path length to each receiver, and therefore the same path length difference. They are opposite in phase and therefore cancel with one another and do not contribute to the Green’s function.

In order for the equal amplitude criterion to be met, when sources span an area of varying impedance the amplitude of the cross-correlations should be normalised by division with $\frac{\rho_s c}{\sin \theta_s}$. In practice this normalisation factor can be difficult to incorporate since the angle of departure from the source is variable. If, however, only changes in density are considered, then the normalisation is simplified and the cross-correlations need only be divided by the density at the source location before summing.

More complex paths may exhibit multiple stationary points, located in both the water column and the sediment, corresponding to a particular path length difference; however, they will sum to zero so long as the source column spans all paths that have a stationary point.

Truncations in the integral of Eq. (3.18) may also be apparent as peaks in the summed cross-correlation at time intervals corresponding to cross-

correlations between paths from sources located at the water-sediment interface. Consider, as an example, the paths depicted in Figure 3.4(a)-(c). As sources closer to the water-sediment interface are considered, the direct paths, shown as solid lines in Figure 3.4(a), converge to the direct paths from a source in the sediment, shown as dashed lines in Figure 3.4(a). At the bottom of the sediment these paths converge with the bottom bounce paths, shown as solid lines in Figure 3.4(b), which in turn converge to the dashed paths shown in Figure 3.4(c) at the water-sediment interface.

Sediment sources would, of course, be difficult to incorporate experimentally. The theory here is therefore important for understanding how the more realistic configuration in which the sources are limited to the water column will affect the summed (over all sources) cross-correlation. If the sources in the sediment are not included in the summation, discontinuities in the integral will exist at the water-sediment interface for the water source paths in Figure 3.4(a) and (c). The path length difference for this

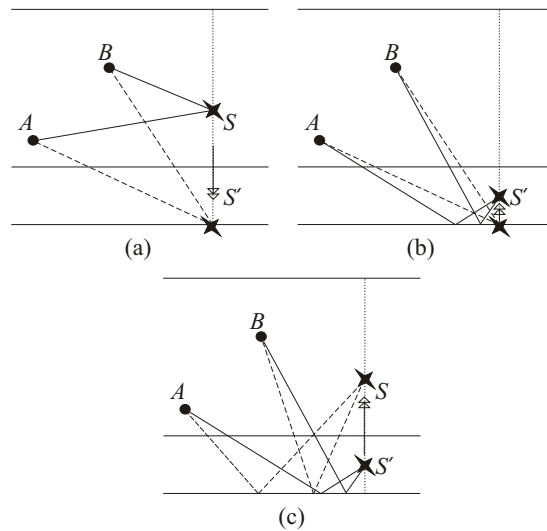


Figure 3.4: The direct paths, solid lines in (a), and bottom bounce paths, dashed lines in (c), are linked via a continuous transition through sediment source configurations (b); a truncation of the integral results in a discontinuity in the arrival structure of the paths if sediment sources are not considered.

discontinuity is

$$\begin{aligned} \Delta L = & \sqrt{(D - z_A)^2 + x_A^2} - \sqrt{(D - z_B)^2 + x_B^2} \\ & - \left(\sqrt{(D - z_A + 2D_s)^2 + x_A^2} - \sqrt{(D - z_B + 2D_s)^2 + x_B^2} \right), \end{aligned} \quad (3.21)$$

where D_s is the depth of the sediment. If the sediment is shallow ($D_s \ll D$), these discontinuities may not be observable in the summed cross-correlations since the path length differences for a source at the sediment-water interface will be small; however, if the sediment is deep, the discontinuity may be observed as two distinct spurious peaks separated temporally by $\Delta L/c$.

Restricting the sources to the water column can therefore lead to spurious peaks in the cross-correlation function. If the sources are extended through the sediment and the cross-correlation function is normalised by the density at the source, these spurious peaks may be avoided.

3.1.3 Spurious arrivals

Snieder *et al.* [30] and Sabra *et al.* [15] determined that spurious arrivals also exist for their particular geometries and environments. The spurious arrivals that they discuss and the ones described here are all due to the volume of interest not being fully enclosed by sources (i.e., acoustic paths exist between the volume of interest and the external environment that are not sampled, or intersected, by the source line or plane). Each of these aberrations are, however, distinct.

The spurious arrivals described in Section 3.1.2 occur when the sources are limited to the water column. The integral does not extend to infinity resulting in two causes of spurious arrivals. As the source approaches the upper and lower boundaries, the surface and the basement, different paths will converge. Hence, when the sources are contained within the water column, paths which would converge at the sediment bottom do not converge, creating a gap in the cross-correlation integral. Spurious peaks therefore occur at these path discontinuities. The second mechanism of spurious ar-

rivals is a stationary-phase contribution from a source in the water column that does not actually contribute to the full Green's function, such as described in Section 3.1.2 in conjunction with Eq. (3.20). This contribution occurs from cross-correlations between waves that are reflected at the water-sediment interface and waves that pass into the sediment. It should cancel with a stationary-phase contribution of equal amplitude and opposite phase from the sediment. For example, the contribution from the cross-correlation of the paths in Figure 3.3(a) cancels with that from Figure 3.3(b). When these sediment sources are not included a false peak will be recorded.

Sabra *et al.* [15] modelled time-averaged surface generated ambient noise using a horizontal plane of point sources at a constant depth in a waveguide. The spurious arrivals they described are caused by stationary-phase contributions from cross-correlations between a wave that initially undergoes a surface reflection and one that does not. For an isovelocity water column one wave departs at an angle of ϕ from the horizontal, and the other departs at an angle of $-\phi$. These stationary points are intrinsic to the horizontal source configuration. If the depth of the plane of sources is reduced, the spurious peaks converge to the same time delay as the true Green's function paths; however, they are π out of phase and will still result in shading of the Green's function.

Snieder *et al.* [30] used a horizontal line of evenly spaced sources in a homogeneous medium, with one or more horizontal reflectors below and no free surface above. The assumption of there being no free surface means that the spurious paths described by Sabra *et al.* did not exist in Snieder's analysis. The spurious arrivals described by Snieder *et al.* are due to false stationary-phase contributions caused by cross-correlation of waves reflected from distinct reflectors, which occur due to the sources only being in the upper layer. To eliminate these spurious multiples, a second surface of sources would have to be included below the bottom reflector.

3.1.4 Variations in sound speed profile

Introduction of a varying sound speed profile will further complicate the problem. A conceptual argument describing the effect of a sloped sound speed profile specific to the source geometry under consideration is presented here.

Consider the geometry of Figure 3.5. The downward refracting sound

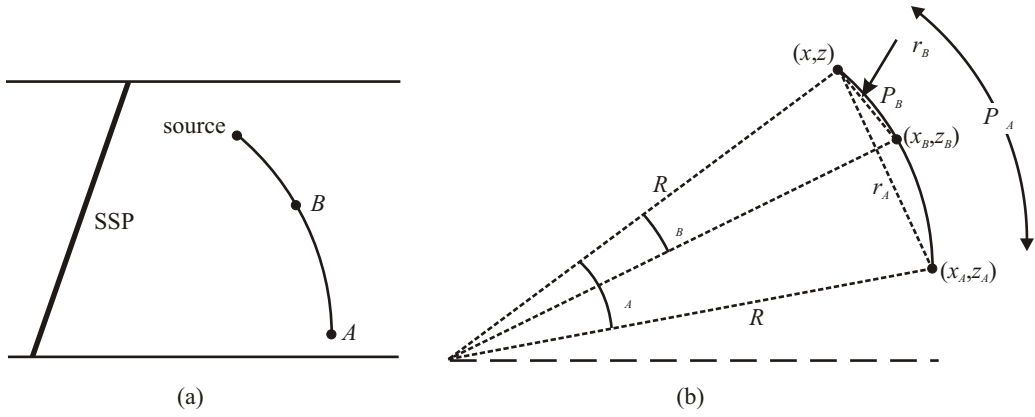


Figure 3.5: (a) Waveguide with a downward refracting sound speed profile. (b) Geometry associated with the curved ray paths, P_A and P_B , from the source to the receivers A and B respectively.

speed profile results in curvature of the ray path towards the region of lower sound speed. The linear distance that sound travels from source to receiver ψ is

$$\Delta r_\psi = \sqrt{(x_\psi - x)^2 + (z_\psi - z)^2}. \quad (3.22)$$

Also, using the cosine rule:

$$\Delta r_\psi^2 = 2R^2 - 2R^2 \cos \theta_\psi. \quad (3.23)$$

Equating Eq. (3.22) and Eq. (3.23), and rearranging to express in terms of θ_ψ yields

$$\theta_\psi = \cos^{-1} \left(1 - \frac{(x_\psi - x)^2 + (z_\psi - z)^2}{2R^2} \right). \quad (3.24)$$

The length dependent component of the phase term of Eq. (3.7) becomes

$$L = P_A - P_B = R(\theta_A - \theta_B). \quad (3.25)$$

Differentiating Eq. (3.25) with respect to z and simplifying yields

$$\frac{\partial L}{\partial z} = \frac{z - z_A}{\sin \theta_A} + \frac{z_B - z}{\sin \theta_B}. \quad (3.26)$$

The partial z -derivative is equal to zero when

$$\frac{z - z_A}{\sin \theta_A} = \frac{z - z_B}{\sin \theta_B}. \quad (3.27)$$

The curvature of the ray path in Figure 3.5(b) has been exaggerated so that the geometry can be more clearly seen. Small changes in sound speed profile will refract the ray path only slightly and hence the radius R becomes large and angles θ_A and θ_B become very small. Using this small angle approximation, equality of Eq. (3.27) is achieved when the origins of arcs P_A and P_B coincide. The stationary phase condition is therefore still achieved when the ray path to receiver A passes through receiver B .

Using a ray-geometric approximation, Snieder *et al.* (Appendix A of [30]) present work that generalises their arguments for the direct wave in a homogeneous medium to a direct wave in a heterogeneous medium with variations in velocity that are sufficiently smooth for ray theory to remain applicable. The environment and geometry used here are different to that of Snieder *et al.*; however, the idea of generalising from a homogeneous to a heterogeneous medium is the same.

3.1.5 Generalised environment

The environments considered in the previous sections all have simplifying assumptions. It needs to be confirmed that the theory does, indeed, carry over to more realistic environments. An understanding of differences that may present themselves, and also of potential limitations that a more realistic environment may present, is therefore important.

In a realistic environment, attenuation as well as the aforementioned variations in sound speed profile and the effect of sediment layers needs to be considered. The inclusion of attenuation adds complications since it will generally result in the paths not cancelling exactly; the degree to which they will cancel one another is environment dependent.

In a generalised environment, the mathematics becomes more complex; however, the fundamental ideas hold. An amplitude and phase shaded Green's function will still be obtained by summing the density normalised source cross-correlations, so long as the source column spans the water column and all underlying sediments. The effect of limiting the sources to the water column, upon the similarity between the summed cross-correlations and the shaded Green's function, is environment dependent.

3.1.6 Simulations

Three simulation environments were selected to clearly demonstrate application of OAI from a physical perspective. The Green's function between two receivers is approximated using the OAI approach for a vertical line of sources. OASES [49] was used for both the OAI approach and to compute the true Green's function between the receivers. The theory derived via the method of stationary phase in previous sections is used only for discussion purposes.

The environments, depicted in Figure 3.6, comprise (a) an isovelocity waveguide with a purely reflective bottom; (b) a completely reflective environment with an isovelocity waveguide and an isovelocity sediment layer; and (c) a more realistic environment with a downward refractive sound speed profile (SSP) waveguide, and an upward refractive SSP sediment layer. Receivers *A* and *B* are located at depths of 80 m and 50 m, respectively. The two receivers are separated 100 m horizontally. A column of sources, spaced at 0.5 m increments, spans the water column in the same vertical plane as the two receivers, 40 m to the right of receiver *B*. The source is a Ricker wavelet with a centre frequency of 350 Hz.

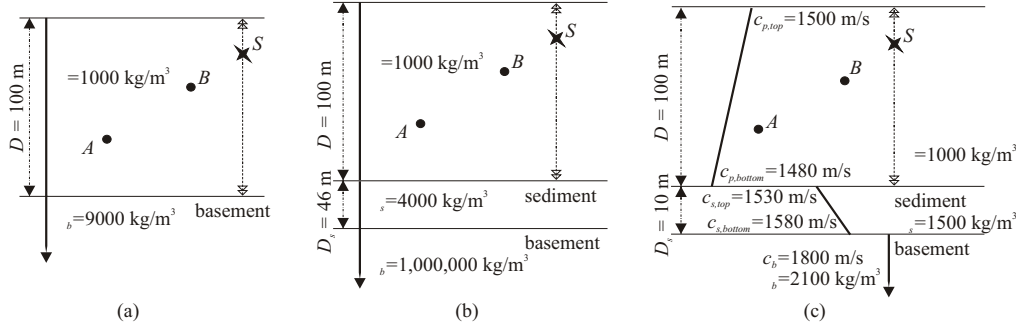


Figure 3.6: Simulated waveguide environments: (a) isovelocity waveguide with a purely reflective bottom (constant $c = 1500$ m/s); (b) isovelocity purely reflective waveguide with a sediment layer (constant $c = 1500$ m/s); and (c) more realistic refractive environment with a sediment layer. A large basement density is used in (a) to increase the amplitudes of bottom-reflected paths, and an unrealistically large value is used in the basement of (b) to give unity reflection at the bottom of the sediment.

The sum of the cross-correlations, Eq. (3.4), is evaluated by treating the integral as a sum over the source column. For each source location the acoustic pressure at A and B is evaluated assuming a constant source spectrum of $S(\omega)$. The pressures are cross-correlated, normalised by the density at the source, and then summed over the source locations and compared to the frequency and phase shaded Green's function between the two receivers:

$$\frac{\rho |S(\omega)|^2}{\omega} e^{i(3\pi/4)} G(R). \quad (3.28)$$

The unstacked cross-correlations, which are the cross-correlations from sources at each depth plotted as a function of source depth, are shown in Figure 3.7 for each simulation environment. Peaks in the cross-correlation functions are visible at times corresponding to differences between the travel time of an acoustic path from the source to receiver A , and the travel time of an acoustic path from the source to receiver B . The path length differences increase or decrease, depending upon the particular paths in question, for sources lower down the water column. The corresponding correlation peak therefore occurs at a later or earlier time. The changes in correlation peak times are visible as curves in the unstacked correlations in Figure 3.7. The

3. ACTIVE SOURCE OCEAN ACOUSTIC INTERFEROMETRY THEORY

curves converge with several others at the top and bottom of the acoustic environment because different paths converge to the same length at these extremities. For example, a direct path and a surface-reflection path will converge at the waveguide surface.

Isovelocity waveguide

Both the unstacked cross-correlations and the stacked response, which is the sum of the cross-correlations over all source depths, $\sum C$, are depicted in Figure 3.7(a) for the isovelocity waveguide. The peaks in the stacked response, $\sum C$, occur due to the Fresnel zones in the vicinity of each stationary point. The $3\pi/4$ phase and $|S(\omega)|^2$ amplitude shaded simulated Green's function, G , is also included for comparative purposes. The peaks in the Green's function, G , occur at the travel times of each acoustic path between receivers A and B , and it is these peaks that the cross-correlations are attempting to replicate.

The direct path stationary point is the temporal maximum of the direct wave cross-correlation arrival structure to each receiver. It occurs at 38 m depth at a time of 0.070 s. The direct path time difference converges to 0.065 s for sources towards the surface, and to 0.052 s for sources towards the bottom. These endpoints do not, however, result in spurious peaks in the stacked response, because they converge with other paths for sources at the given boundary. Stationary points corresponding to arrivals of the reflected paths are more difficult to see as they occur at locations very close to the waveguide boundaries; however, they can still be seen in the stacked response. For example, the peak in the stacked cross-correlations at 0.109 s, circled in red, corresponds to the stationary point of the bottom bounce path to receiver B and the bottom-surface bounce path to receiver A , which occurs at a depth of 98 m and is therefore difficult to distinguish.

Overall, the phase of the stacked cross-correlation shows good agreement with the frequency and phase shaded Green's function, with only minor deviations. The amplitude is not accurate, but this can be explained by

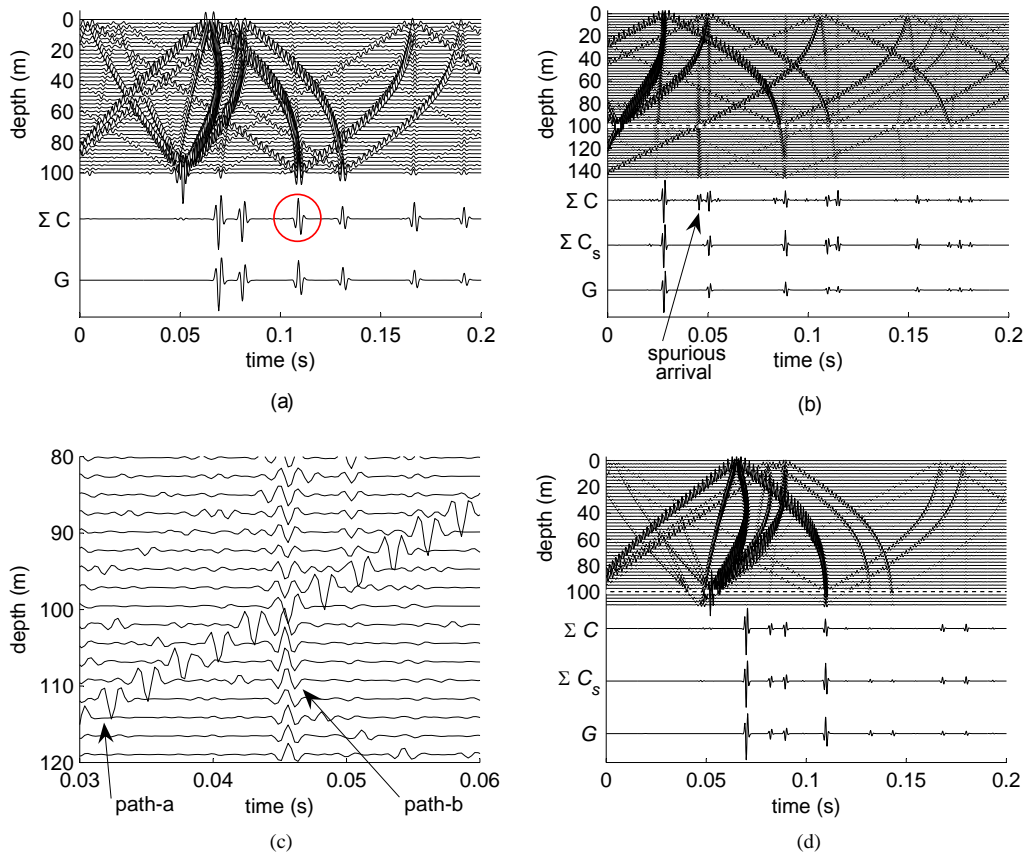


Figure 3.7: The cross-correlations for (a) the isovelocity waveguide, (b) the reflective environment with a sediment, (c) a magnified portion of (b), and (d) the refractive environment, are plotted as a function of depth. The water-sediment interfaces in (b) and (d) are marked by a dashed white line. The stacked cross-correlation from a column of sources in the water, ΣC , the stacked trace with sediment sources included for (b) and (d) only, ΣC_s , and the shaded Green's function, G , are also plotted. The two paths indicated in (c) are the arrivals for the ray paths depicted in Figure 3.8.

the difference in amplitude between the stacked cross-correlations and the Green's function due to path dependent components, $\Gamma^{b_A+b_B}$, ϕ_s and ξ , as derived in Eq. (3.16).

Waveguide with single sediment layer

This particular waveguide environment was chosen in order to see the effect of a sediment layer upon the stacked cross-correlation. In order to emphasise what is happening the receivers are separated only 30 m horizontally, the Ricker wavelet centre frequency has been doubled to 700 Hz, and the source column spacing halved to 0.25 m. The remainder of the source/receiver configuration is identical to that of the isovelocity waveguide example.

Both the unstacked cross-correlations and the stacked responses are shown in Figure 3.7(b). The stacked response for the case when the source column terminates at the water-sediment interface, $\sum C$, contains the arrival paths observable in the shaded Green's function, G ; however, it also contains several spurious arrivals, the most noticeable of which occurs within the time interval 0.044-0.047 s. The stacked response with sediment sources included, $\sum C_s$, is plotted for comparison. Such a configuration would likely not be implemented in practice, but is useful here for explaining the results from the line water column sources. The stacked response with sediment sources does not contain the spurious arrivals. The spurious arrivals observable in $\sum C$ are due to the source column not continuing through the sediment and therefore not producing a perfect time-reversal mirror.

One contribution to this spurious arrival is due to the discontinuities in the arrival structure caused by truncation of the $C_{AB}(\omega)$ integral at the bottom of the water column. The two paths affected are shown in Figure 3.8(a) and (b) and their cross-correlations, depicted in Figure 3.7(c), are denoted path-a and path-b respectively. Path-a and path-b are cross-correlation peaks corresponding to differences in arrival times between paths from the source to each receiver, and as such, should not be confused with the individual acoustic paths. For sources near the water-sediment interface the

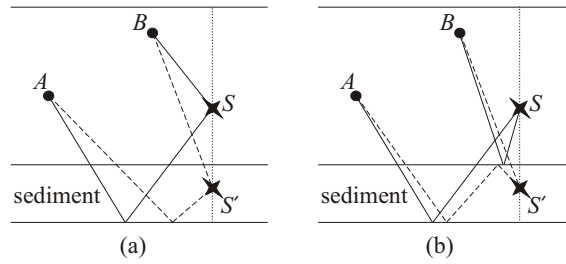


Figure 3.8: Two possible sets of ray paths: (a) direct path to B and the bottom bounce path to A ; and (b) a path to B with one water-sediment bounce and a path to A that has two transmissions through the interface. In both cases the solid lines represent paths from sources in the water, denoted S , and the dashed lines represent paths from sources in the sediment, denoted S' .

arrival time for path-a, the solid line in Figure 3.8(a), transitions smoothly with the solid line, path-b, of Figure 3.8(b). This can be seen by examining the arrival structure in Figure 3.7(c). The two arrivals do not, however, cancel each other. For both path-a and path-b the path length difference between the source and each receiver decreases for sources closer to the sediment, as shown in Figure 3.7(c) and Figure 3.9. The two sets of ray paths are also in phase, as shown in Figure 3.7(c). The two arrivals will therefore sum together to contribute to the largest spurious arrival in trace $\sum C$ of Figure 3.7(b).

If the sources are extended through the sediment to the basement then the summation over the arrival structure corresponding to Figure 3.8 cancels completely at the water-sediment interface. At the interface the cross-correlation of the solid line representation of path-a, see Figure 3.8(a), will transition smoothly into the dashed line representation of path-a both in terms of arrival time and amplitude. For path $A + B$ the number of transmissions through the sediment remains constant. The difference in path length continues to decrease for sources at greater depths and there is no phase change, see Figure 3.7(c). Cancellation at the interface therefore occurs. Path-b also transitions smoothly; however, this time the difference in path length has a local minimum at the water-sediment interface. The vari-

ation in path length difference is small as a function of depth and hence this is difficult to see in Figure 3.9. The phase of the cross-correlation is inverted at the interface, as shown in Figure 3.7(c), resulting in direct cancellation. For sources closer to the basement, the arrival structure and amplitude will transition smoothly into that of other paths. For example, path-a will converge to the same arrival time as all other combinations of direct and single basement bounce paths to A and B , and since the amplitudes of each set of paths will be the same, a smooth transition between the paths will occur.

A second contribution to the largest spurious arrival is a stationary-phase contribution from a source in the water column which does not actually contribute to the full Green's function, as explained in Section 3.1.2. An example schematic of the scenario is shown in Figure 3.3(a). The solid line of path-b should not contribute to the Green's function as the signal received by A never passes through B , regardless of the source depth; however, a stationary point exists when the two paths depart the source at the same angle (i.e., 67.3 m source depth). This stationary point is difficult to see in the stacked response since the difference in path length of Figure 3.8(b) varies by less than a metre ($\sim \frac{\lambda}{5}$) over the entire depth, see Figure 3.9. As seen in Figure 3.9, a second stationary point exists within the sediment at a depth of 133 m. If the sources are extended through the sediment then this stationary point annuls the contribution from the stationary point in the water column.

As expected, the largest spurious peak from the water source column cross-correlation is not observable in the stacked cross-correlation of the column of sources that extends through the sediment in trace $\sum C_s$ of Figure 3.7(b). Other deviations from the expected shaded Green's function are also reduced or removed.

Refractive environment with sediment

The source and receiver geometry and source type are identical to that of the original isovelocity waveguide example. The stacked responses for the

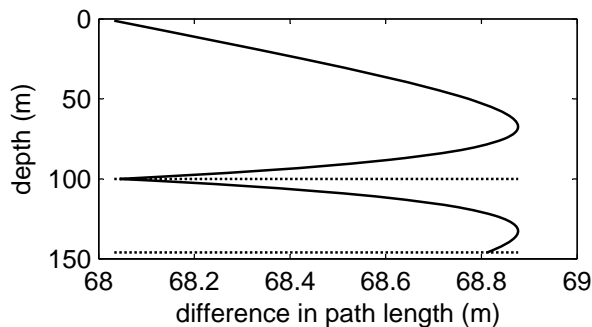


Figure 3.9: The difference between the path lengths from the source to receiver A and the source to receiver B as a function of source depth for the ray path geometry of Figure 3.8(b). The horizontal dotted lines represent the water-sediment interface and the sediment bottom.

water column sources only, $\sum C$, and for the case where the sources extended through sediment, $\sum C_s$, as well as the shaded Green's function, G , are shown in Figure 3.7(d). The phase of the water column stacked response is in reasonable agreement with that of the shaded simulated Green's function. The path time differences have converged almost completely to their sediment-bottom interface value at the water-sediment interface and hence the spurious arrivals which were easily observed in the previous example are not apparent here. Even if the source column could be extended into the sediment, only a minor increase in accuracy would be obtained. These results agree with the simulations of Roux and Fink [29], who concluded that the effect of limiting sources to the water column is negligible when the modal continuum of the sediment is small relative to that of the water.

3.2 Horizontal straight line towed source

Ocean acoustic interferometry can be performed using a horizontal line, rather than a vertical column, of sources. The source is towed along a horizontal line in the end-fire plane of the receivers, starting directly above one receiver, and travelling away from the receivers. The relationship between the summed cross-correlation and the Green's function is derived, using the

methodology of Section 3.1, to be [15, 30]

$$C_{AB}(\omega) = e^{i(3\pi/4)n} |S(\omega)|^2 \sum_{p_s} \left(\frac{\Gamma^{b_A+b_B} \rho_s^2 G_f(R(x_s))}{\cos \phi_s} \sqrt{\frac{\left(\frac{1}{L_B(x_s)} - \frac{1}{L_A(x_s)}\right) c}{8\pi\omega}} \right). \quad (3.29)$$

3.3 Horizontal hyperbolic towed source

OAI using a straight line tow source relies on the fact that the horizontal distance from the source to receiver A is always $x_A - x_B$ further than to receiver B , where the x axis has been specifically defined as the horizontal axis between A and B . A second tow-source configuration in which the horizontal distance to each receiver differs by a constant amount is described here.

Consider Figure 3.10, which is a geometrical view of the source, p_n , and receivers, A and B , from above. The source location, p_n , which varies as a function of ϕ , the angle from the line connecting A and B , is defined as being a constant distance, Δr , further from receiver A than B (i.e., the distance from B is x_n and the distance from A is $x_n + \Delta r$). If the receiver B is defined as the origin then the location of p_n is

$$p_n = (x_n \cos \phi, \pm x_n \sin \phi). \quad (3.30)$$

For the case when $\phi = 0$ (i.e., p_n lies upon the horizontal line joining A and B), p_n and x_n are denoted p_0 and x_0 respectively.

Although the horizontal difference in distance from the source p_n to the receivers A and B is a constant value Δr , this distance is $2x_0$ smaller than the horizontal distance between the receivers, and therefore the hyperbolic configuration is set-up to perform OAI not between receivers A and B , but between receiver A and a virtual receiver V located Δr from A . Note that unlike the straight line tow source this configuration assumes that acoustic paths are azimuth independent, that is, the acoustic path of the signal leaving the source point p_n will be the same over the distance x_n in both

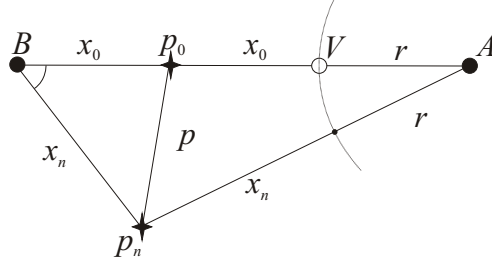


Figure 3.10: Geometrical construct for determining the equation governing the location of point p_n , which is a constant Δr further from A than B .

the direction towards A and the direction towards B , and the acoustic path between A and any point Δr from A will be constant. The technique is therefore only applicable in a range independent environment.

From geometry:

$$(x_n + \Delta r)^2 = x_n^2 + (2x_0 + \Delta r)^2 - 2(x_n)(2x_0 + \Delta r) \cos(\phi). \quad (3.31)$$

Rearranging to express in terms of ϕ yields

$$\phi = \cos^{-1} \left(\frac{2x_0^2 + 2x_0\Delta r - x_n\Delta r}{x_n(2x_0 + \Delta r)} \right). \quad (3.32)$$

The points p_n therefore form a hyperbola which has its asymptotic origin at the point midway between the two physical receivers, A and B , its x -intercept at the midpoint of receiver B and the virtual receiver, V , located between the two physical receivers at the same depth as the first receiver, and its focus at receiver B , as shown in Figure 3.11. If the origin of the system is assumed to be at the first receiver B , and the second physical receiver A lies along the positive x -axis, the governing equation can then be written in the form

$$x^2 = -\sqrt{a^2 \left(1 + \frac{y^2}{b^2} \right)} - c, \quad (3.33)$$

where $a = (2x_0 + \Delta r)/2$, $c = a - x_0$ (x_0 is the location where the hyperbola crosses the x -axis), and $b = -\sqrt{c^2 - a^2}$.

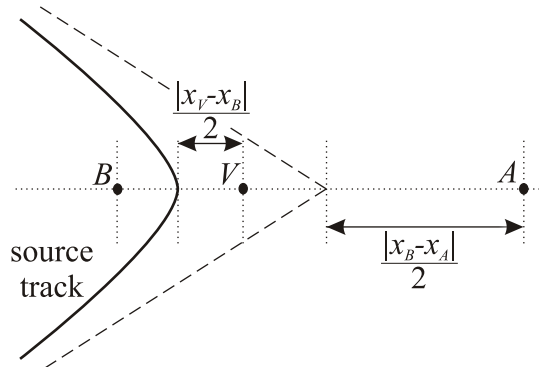


Figure 3.11: Hyperbolic source track as viewed from above. The hyperbola apex passes midway between receiver A and virtual receiver B and the asymptote is midway between B and A .

The hyperbola converges to the straight line scenario as $x_0 \rightarrow 0$. Hence the hyperbolic tow-source can be considered to be a similar geometrical set-up to the straight line scenario, although in this case, the horizontal difference in path length is a constant value of $x_A - x_V$. The resulting cross-correlation sum will therefore relate to the Green's function between the virtual receiver, V , and receiver A rather than the Green's function between the two physical receivers, B and A . It must be remembered, however, that unlike the straight line scenario, the hyperbolic configuration relies upon range independence.

3.4 Conclusion

A stationary phase argument was used to theoretically describe the relationship between the summed cross-correlations from a line of active sources, and the Green's function between two hydrophones. The theory and simulations for the vertical line source presented here were shown to be in agreement with a modal approach presented by others, and results for cross-correlations of towed horizontal line and hyperbolic sources were shown to be in agreement with theoretical work on cross-correlations of wave gen-

erated ocean noise, modelled as a horizontal plane of sources, as well as horizontal lines of seismic surface sources. It was demonstrated that in a range independent environment the Green's function can be approximated from cross-correlations of a horizontal hyperbolic towed source with its apex at a location horizontally between two physical hydrophones.

All three OAI source scenarios: the source column, straight line towed source, and hyperbolic towed source, have their advantages and drawbacks. The source column is located in a region close to both receivers and therefore attenuation is minimal, but suffers from there being no sources in the underlying sediment and hence the modal continuum of the sediment is not fully accounted for [29].

The towed source scenarios are advantageous in that once the source is deployed the only consideration is the ship path; however, they suffer from intrinsic stationary-phase contributions from cross-correlations between a wave that initially undergoes a surface reflection and one that does not. If the source depth is reduced, the spurious arrivals converge to the same travel time as the true Green's function paths; however, they are π out of phase and will result in shading of the Green's function. The hyperbolic towed source method is the only non *end-fire* tow-source geometry that is feasible. The source must, in this case, have its apex at a location horizontally between two physical hydrophones. It has the advantages of being able to approximate the Green's function between a physical receiver and a virtual receiver and, since the sources do not have to be near either receiver, of being accessible even when buoys mark the beginning and end of arrays; however, it suffers from the disadvantages that the hyperbola can be difficult for a ship to navigate, and the theory assumes range independence.

Experimental results for cross-correlation of sound from a vertically lowered source and a horizontally towed source will be presented in Chapter 6, and compared with experimental results from cross-correlation of ship dominated ambient noise.

Chapter 4

Experimental Environment

This chapter describes the underwater environment where all of the experimental data presented in this thesis were obtained, as well as the equipment used. The techniques used to process and analyse the data are described in Chapters 5 and 6.

The empirical data used in this thesis were collected during the Shallow Water 2006 (SW06) experiments [70]. This chapter starts with an overview of the SW06 experimental location, measurement equipment, acoustic sources, and ocean sound speed profiles (SSPs). The effects of the local water SSP upon acoustic propagation are then explained. It is shown that due to the steep thermocline of the ocean SSP, the ocean-only signal (no interactions with surface or bottom of water column) is often not from a direct arrival; rather, it is an interference of many propagation paths. This suggests that it is likely to be difficult to extract meaningful information from a reflection coefficient inversion, which is based on comparison of the amplitude of the direct ocean path to that of the bottom reflected path. A reflection coefficient inversion was performed and was found to only obtain a sediment sound speed within a 60 m/s range, though values estimated by others [71, 72] do lie within these bounds, supporting the validity of the results presented here. A relationship between sub-bottom arrival times, where sub-bottom paths are defined as those that penetrate the underlying

sediment, and sediment sound speed is also estimated using a time-domain analysis, but the limited angular coverage of the bottom interacting acoustic paths prevents the decoupling of sediment thickness and sound speed.

4.1 Overview of experiment

The SW06 experiment was a large scale collaborative shallow water acoustic experiment, combining both low frequency (< 1000 Hz) and medium frequency (1000–10,000 Hz) acoustic tests, conducted off the Eastern US seaboard, at the location shown in Figure 4.1(a). Dozens of research bodies, seven ships, 62 moorings, and aircraft and satellite coverage, were all used in the experiments that ran from mid-July to mid-September 2006 [70]. Data pertinent to this thesis were collected on four hydrophone arrays between August 30 and September 6 using the deployment vessel R/V *Knorr*.

The four hydrophone arrays that were used for acoustic data collection are:

- MPL-VLA1 (*Marine Physical Laboratory - Vertical Line Array 1*), a 16 element array operated by Scripps Institution of Oceanography;
- SWAMI32 (32 hydrophone *Shallow Water Acoustic Measurement Instrumentation*), an L-shaped array operated by ARL-UT (Applied Research Laboratories, The University of Texas at Austin);
- SWAMI52, a 52 hydrophone L-shaped array also operated by ARL-UT; and
- Shark, a 48 element L-shaped array operated by Woods Hole Oceanographic Institute [75].

The locations of these four hydrophone arrays are shown in Figure 4.1(b). Detailed descriptions of the arrays are included in Appendix B. Photographs of the MPL-VLA1, SWAMI32 and Shark instrumentation are included in Figure 4.2.

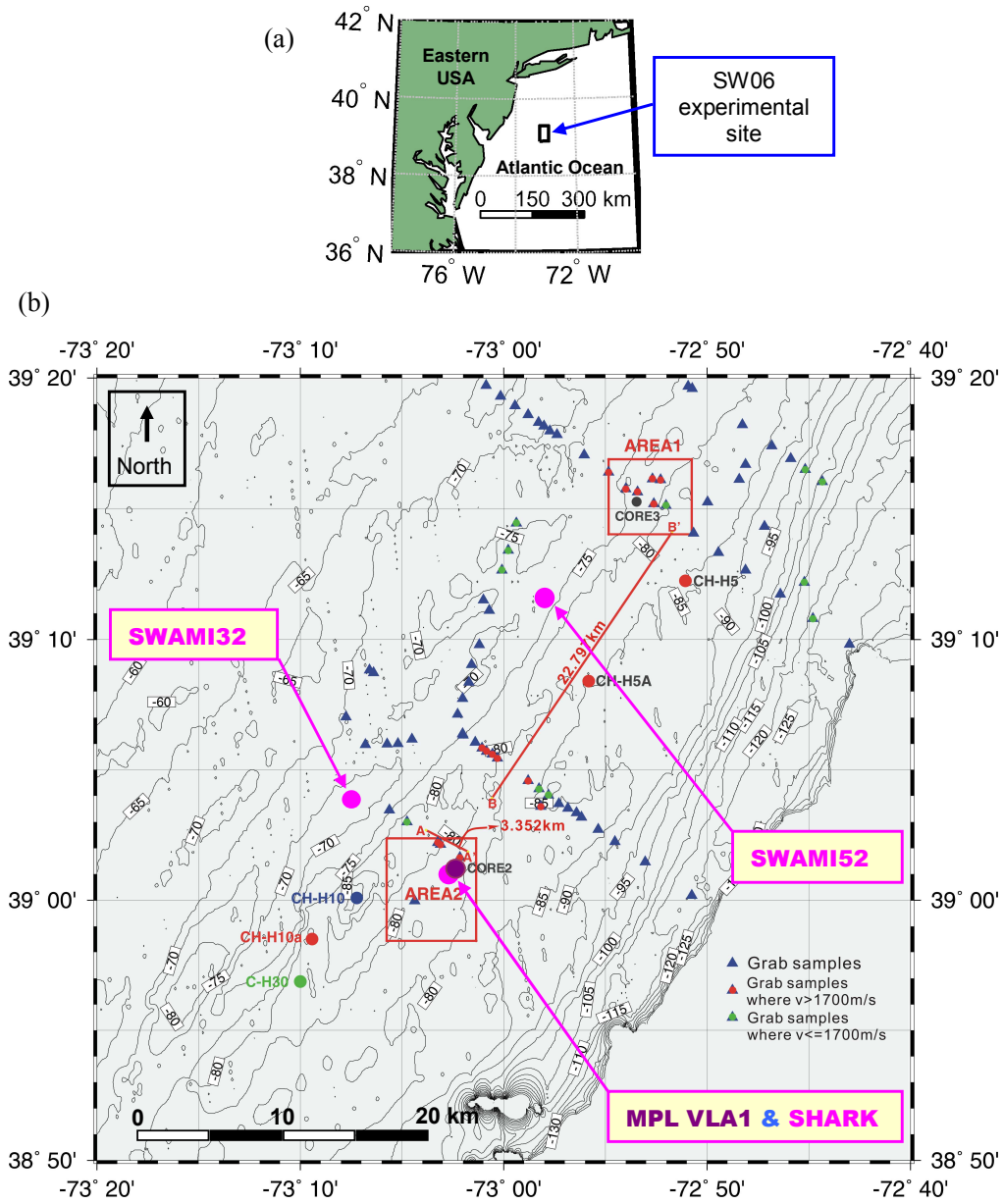


Figure 4.1: (a) Geographic location of the SW06 experimental site on the New Jersey Shelf. (b) Locations of the four hydrophone arrays. Triangles mark locations for which sediment grab sample data (information about the sediment determined from the collection and analysis of small physical samples) exists [73]. The contours represent water depth in metres. (b) is adapted from [74].

4. EXPERIMENTAL ENVIRONMENT

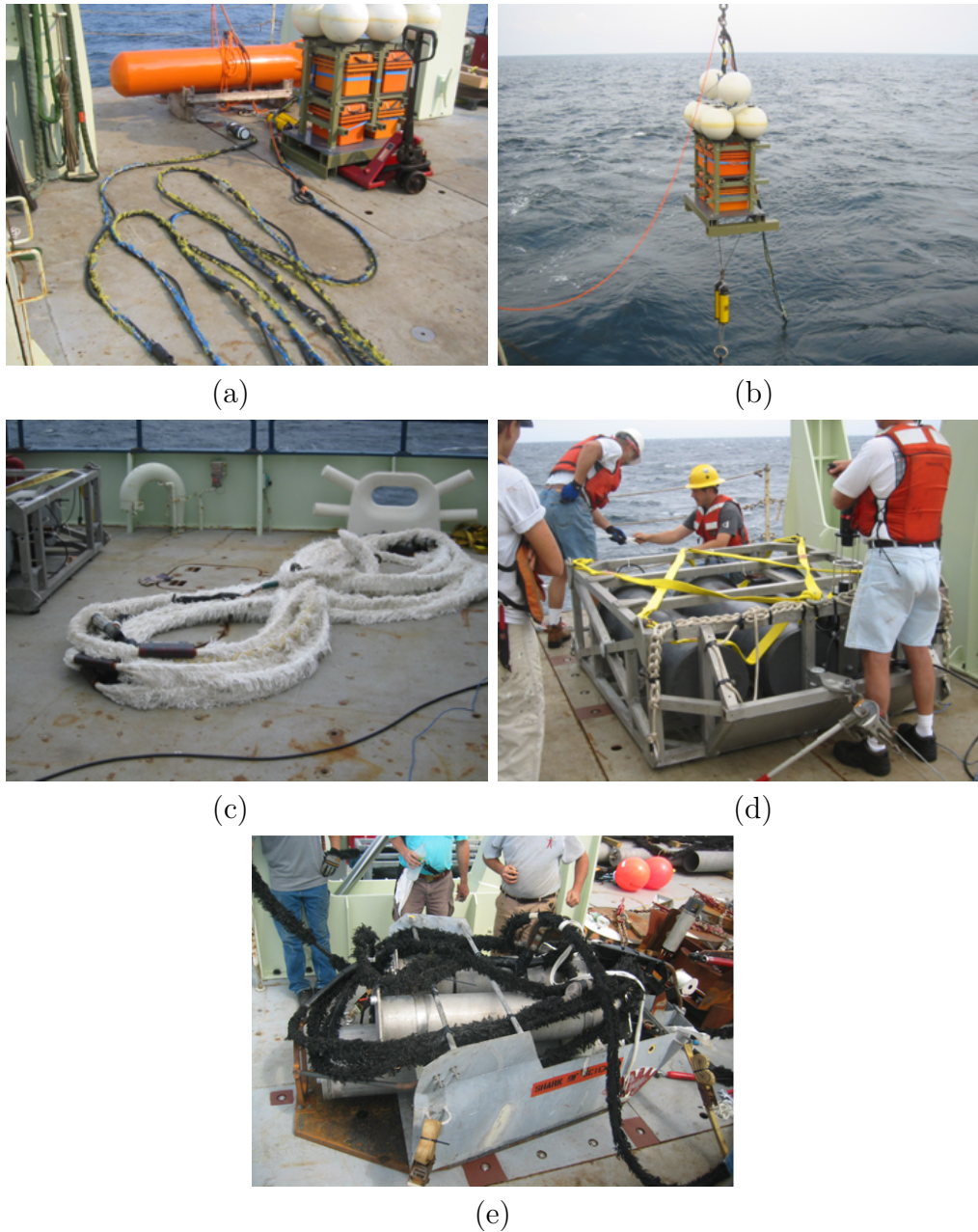


Figure 4.2: Hydrophone array equipment prior to deployment. (a) MPL-VLA1: 16 element hydrophone array (front); electronics module with pressure case and flotation mounted on a fiberglass box structure (right); and torpedo-shaped buoyancy float (back). (b) MPL-VLA1 electronics module being lowered into the ocean. The yellow package just above the water is a dual acoustic release tilt/heading/depth sensor. (c) SWAMI32 vertical line array. (d) SWAMI32 electronics module. (e) Shark electronics battery sled with part of the HLA/VLA coiled on top. (e) is sourced from [75].

Acoustic signals were recorded from several different source types. All of the controlled source signals were emitted by a mid-frequency free flooded ring transducer source (model ITC-2015), as shown in Figure 4.3(a). The source depth was controlled by a ship-board winch, as shown in Figure 4.3(b). The sound sources used were:

- a 1500–4500 Hz linear frequency modulated (LFM) pulse (Section 4.2.2);
- ambient noise (Chapter 5);
- R/V *Knorr* ship noise (Chapter 6);
- a 1100–2900 Hz LFM pulse (Chapter 6 and Section 7.2.2); and
- a broadband 1100–2950 Hz energy pulse (Section 7.2.2).



Figure 4.3: Photographs of (a) the ITC-2015 mid-frequency source, and (b) the source being controlled using a ship-board winch (Note the cable ties that were used to control the joystick position, and hence rate of descent, when the source needed to be lowered at a slow but constant rate!).

4.1.1 Sound speed profiles

Water column properties were recorded using Sea-bird 911*plus* CTD (conductivity, temperature, depth) instrumentation [76]. The profiler records

oxygen content, fluorescence, light transmission, density, salinity and temperature as a function of depth, and the SSP is interpolated from this data. Two CTD profiles were taken during each recording, one as the CTD device was lowered to just above the seafloor, and one as it was raised to the surface. The up-going profile was ignored as the CTD sensors are on the bottom of the device and therefore the device itself would have interfered with measurements on the up-going track. Twenty five CTDs were measured from the R/V *Knorr* platform between August 30 and September 6, and the SSPs from these are shown in Figure 4.4. Tropical Storm Ernesto passed through the experimental region on September 2, creating high sea states and strong wind conditions. The SSPs recorded after the storm exhibit a deeper mixing layer, which was forced by the increase in wave energy during the storm. The sound speed of the mixing layer is also lower due to the incorporation of the lower temperature waters from below the original mixing layer.

4.2 Analysis of experimental environment

Data from a mid frequency (1500–4500 Hz) LFM source were recorded on August 31. The data were recorded on MPL-VLA1, which was arranged as shown in Figure 4.5(a). The array was deployed in a water depth of 79 m. The first element (hydrophone 1) was 8.2 m above the seafloor, and inter-element spacing was 3.75 m. Using dynamic positioning, the source was held at a constant range 230 m from the array, and slowly lowered down the water column, being held at water depths of 15–65 m in 10 m increments for 5 min at each source depth. Clipping of the recorded signal was observed periodically in the upper 30 m of the water channel. All clipped data were discarded.

CTDs 36 and 37 were recorded at the beginning and end of the source lowering. The SSP from each of these CTDs is shown in Figure 4.5(b).

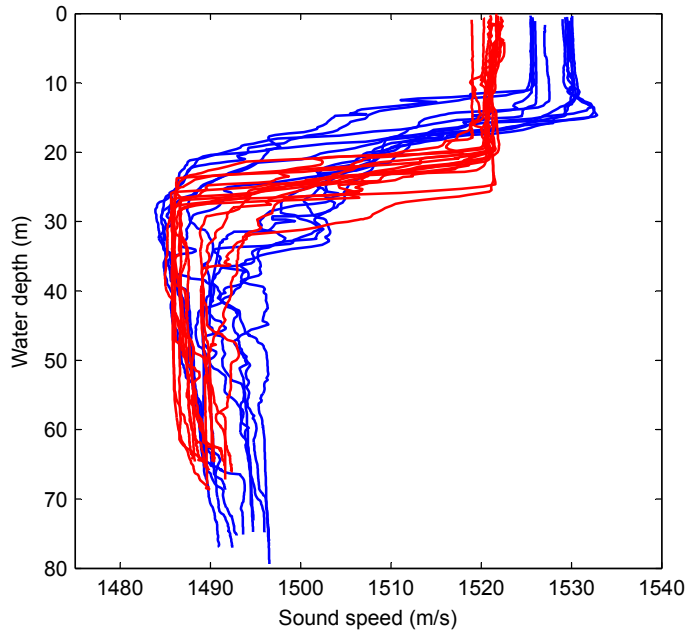


Figure 4.4: SSPs recorded from all CTDs measured from R/V *Knorr* between August 30 and September 6. Blue line profiles were recorded before Tropical Storm Ernesto and red line profiles were recorded after the storm.

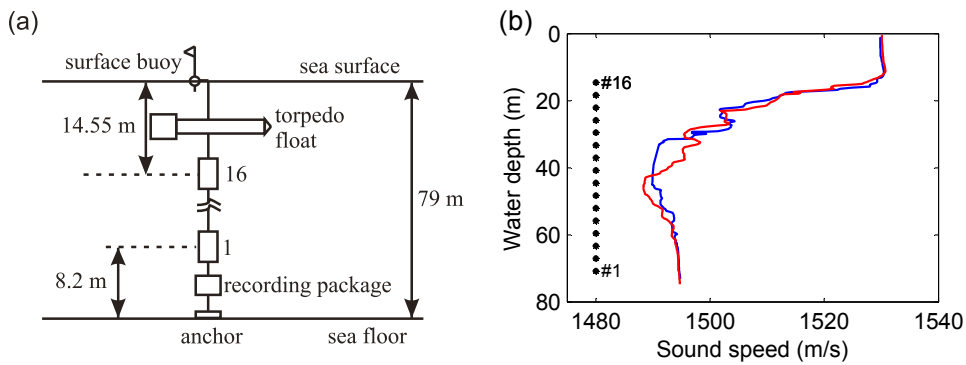


Figure 4.5: MPL-VLA1 array (a) geometry, and (b) SSPs from CTDs 36 (blue) and 37 (red). The 16 black markers in (b) represent the hydrophone depths.

4.2.1 Effects of ocean sound speed profile

The two SSPs of Figure 4.5(b) show similar characteristics: an almost isovelocity layer extending down to less than 20 m depth below the ocean surface, followed by a steep thermocline over which the sound speed drops about 40 m/s within 20 m, and then a more gentle sound speed increase towards the bottom. SSPs with similar characteristics have been recorded at nearby locations by Badiy *et al.* [77], who showed that small changes in sound speed within the thermocline have large effects upon acoustic transmission.

In an isovelocity waveguide the ocean-only paths are straight lines, and hence the amplitude of the received signal is virtually uniform over the waveguide depth. If a varying SSP exists, the sound may be refracted such that at some locations multiple ocean-only paths intersect, whilst at others there is no ocean-only path at all. The effect of sound speed variations on the ocean-only paths for the experimental environment was modelled using OASES (*Ocean Acoustics and Seismic Exploration Synthesis*) wavenumber integration based software [49], first using the SSP of CTD36 (SSP36), and then using the SSP of CTD37 (SSP37). Sources within or below the thermocline are refracted in such a way as to create interference patterns; however, these patterns are highly sensitive to the SSP. Consider, for example, the ocean-only path fields created by a source depth of 45 m shown in Figure 4.6(a)–(b). Interference patterns can clearly be seen for both SSPs, but their locations are distinct. For example, the results assuming SSP36, depicted in Figure 4.6(a), show a high amplitude around hydrophones 15 and 11–12, but if SSP37 is assumed, the amplitude is low, as shown in Figure 4.6(b). Similarly, the high amplitude seen between hydrophones 7 and 8 assuming SSP37, does not exist for SSP36.

The source at 15 m depth is around the top of the thermocline and this causes a large shadow zone at and below the thermocline, as shown in Figure 4.6(c). The signal, which is shown in Figure 4.6(d) for both sound speeds, is less sensitive to SSP changes although there are some regions where significant differences are observable, such as above 15 m and

from 35–55 m. For the other source depths large SSP dependent amplitude variations occur over short variations in depth, as is shown in Figure 4.6(e)–(g). These variations in the direct path amplitude mean that comparing the direct and bottom bounce path amplitudes for reflection coefficient inversion is difficult.

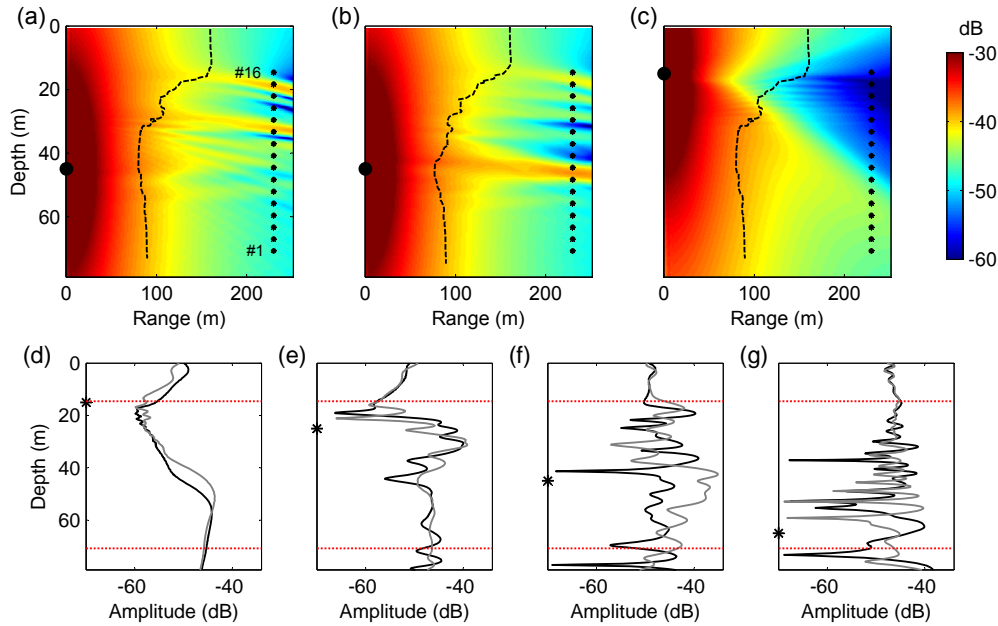


Figure 4.6: Modelled pressure amplitude (dB relative to source amplitude) of the 2200 Hz ocean-only field versus range and depth for source depths of (a) 45 m (SSP36), (b) 45 m (SSP37), and (c) 15 m (SSP36). The shape of the SSP as a function of depth is overlaid as a black dashed line (see Figure 4.5(b) for exact values). The large black circles mark the source location, and the 16 black markers at 230 m range represent the VLA locations. Plots (d)–(g) show the amplitude versus depth at 230 m range using SSP36 (black) and SSP37 (grey) for source depths of (d) 15, (e) 25, (f) 45, and (g) 65 m (black asterisks). The horizontal dotted lines represent the top and bottom of the VLA.

4.2.2 Reflection coefficient inversion

Reflection coefficient inversion has been successfully performed by others and the methodologies are well understood [78]. It is applied here to mid-

4. EXPERIMENTAL ENVIRONMENT

frequency data collected on August 31. Signals received for a source depth of 15 m were considered since they have the largest grazing angles, and will therefore have the most paths above the critical angle of reflection. The signals were matched filtered with a 1 second 1500–4500 Hz LFM pulse replica signal. The matched filter correlates the signal with the energy and amplitude normalised replica by multiplication in the frequency domain. A Hilbert transform is then applied; negative frequency components are set to zero and positive frequency components below the Nyquist frequency are doubled. The envelope of the inverse Fourier transform is then calculated. For each hydrophone depth, 300 chirps were measured. The envelope of the match filter outputs for each chirp are shown in Figure 4.7(a).

Results of Bellhop [48] finite-element ray tracing in the water column, using the measured SSPs, showed that the surface and bottom reflected paths are less sensitive to changes in SSP than direct paths. For bottom and surface bounce paths over a 230-m range, the ray paths are nearly straight lines. Thus the reflection coefficient can be extracted by comparing the amplitudes of these paths. The amplitude ratio of the bottom and surface reflected signals was compared to that of an OASES model assuming perfect reflections; however, sensible values for reflection coefficients could not be obtained. This is likely due to the inherent difficulty in generating an accurate model of the ocean surface for reflection problems [4]. The bottom reflected to direct path ratios of the experimental and simulated data were therefore compared instead.

The SSP was assumed to be that of CTD36 since the 15-m source depth signals were recorded at a time close to this measurement. The data from hydrophones in the central part of the array were discarded since signals in this region are most sensitive to SSP variations, as can be seen in Figure 4.6(d). Inclusion of these data would likely have yielded results that were highly erroneous if the actual and assumed SSPs differed. For the bottom four hydrophones (1–4), a reflection coefficient of unity was estimated, suggesting that the received signal is below the critical angle. For the top

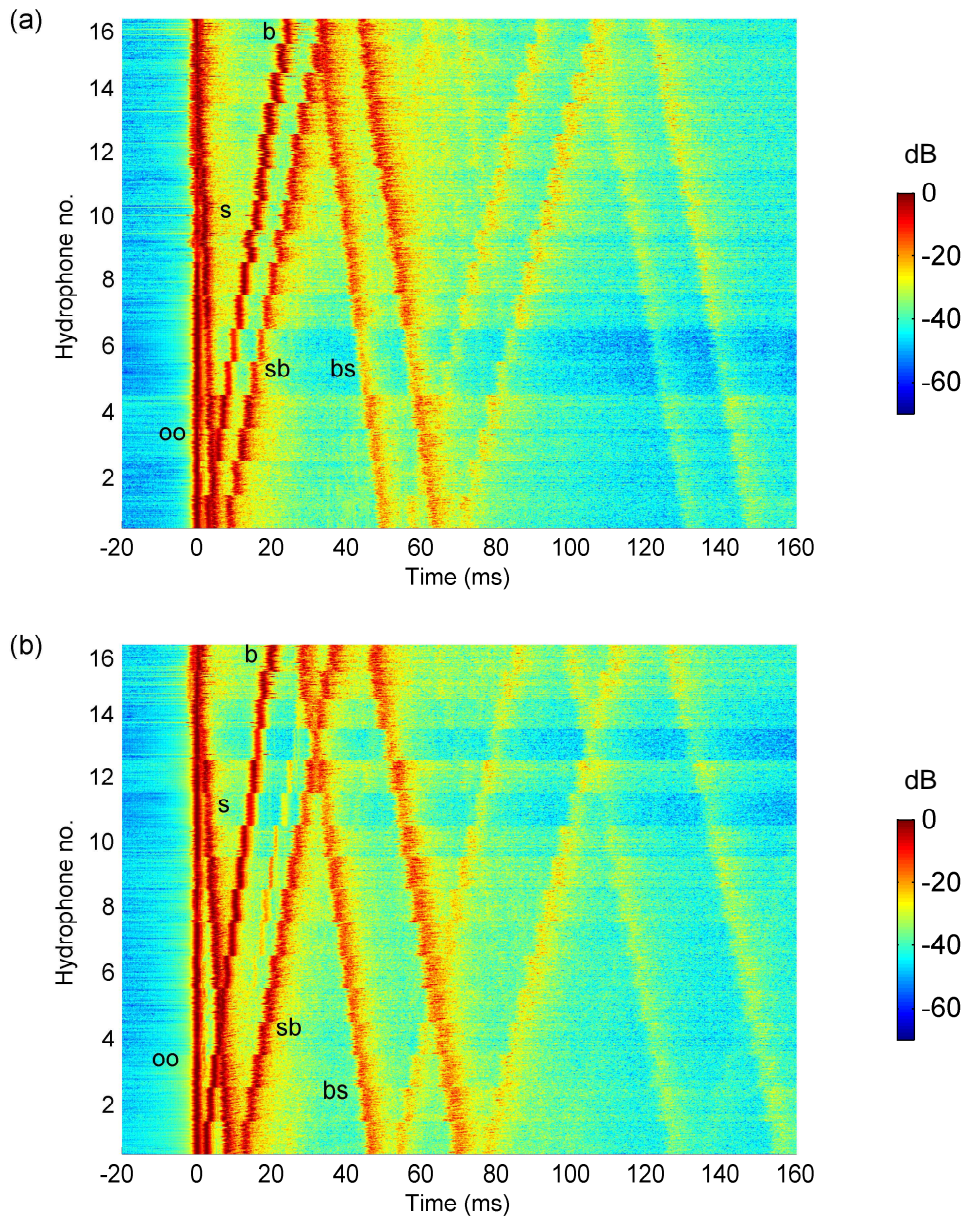


Figure 4.7: Match filter of 1500–4500 Hz chirp, recorded on all 16 hydrophones for a source depth of (a) 15m, and (b) 25m. For each hydrophone depth, 300 chirps were measured and the match filter from each of these is displayed here in a stacked arrangement at that depth. The amplitude (dB) is relative to the highest amplitude of the match filter for each chirp. The arrival paths are denoted oo (ocean-only), s (surface bounce), b (bottom bounce), sb (surface-bottom bounce) and bs (bottom-surface bounce), and time is relative to the ocean-only arrival.

4. EXPERIMENTAL ENVIRONMENT

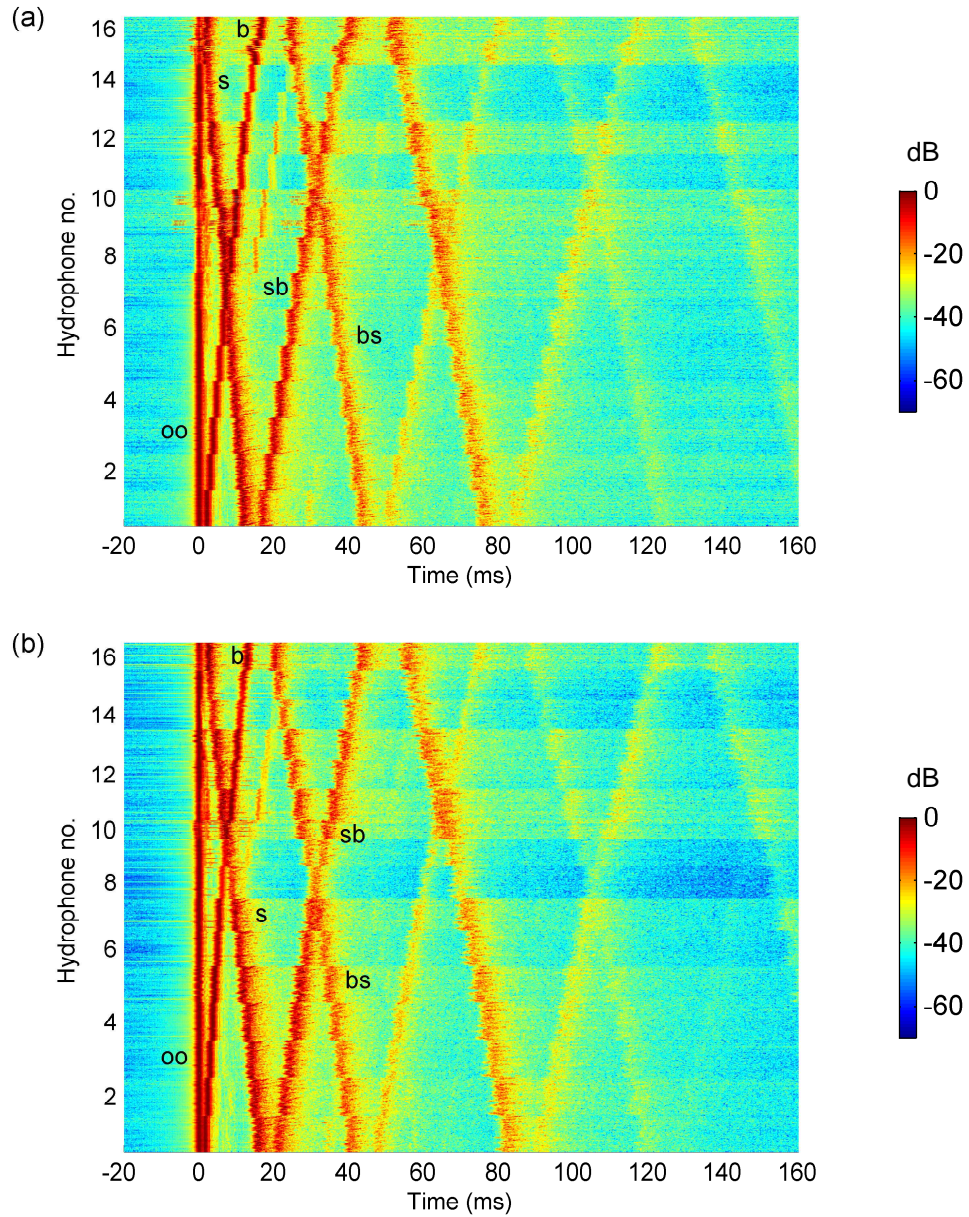


Figure 4.8: Match filter of 1500–4500 Hz chirp, recorded on all 16 hydrophones for a source depth of (a) 35m, and (b) 45m. For each hydrophone depth, 300 chirps were measured and the match filter from each of these is displayed here in a stacked arrangement at that depth. The amplitude (dB) is relative to the highest amplitude of the match filter for each chirp. The arrival paths are denoted oo (ocean-only), s (surface bounce), b (bottom bounce), sb (surface-bottom bounce) and bs (bottom-surface bounce), and time is relative to the ocean-only arrival.

four hydrophones (13–16) a reflection coefficient of 0.4 was estimated. This suggests a critical angle of 20–25°, corresponding to a sediment sound speed of 1590–1650 m/s, which is in agreement with Jiang and Chapman [71] and Huang *et al.* [72].

4.2.3 Sub-bottom arrival time inversion

The envelopes of the matched filtered signals for each chirp for source depths of 25, 35 and 45 m are plotted in Figure 4.7(b) and Figure 4.8. Definite sub-bottom arrivals can be seen as peaks in the amplitude between the third and fourth major arrivals (i.e., between the bottom and surface-bottom paths) for 15 source-hydrophone pairs: 25-m source depth, hydrophones 7–12; 35-m source depth, hydrophones 8–13; and 45-m source depth, hydrophones 11–13. Sub-bottom arrivals were expected for the 15-m source depth; however, these occurred around the time of the surface-bottom reflected paths, and hence cannot be individually discerned.

The arrival time difference between the bottom and sub-bottom paths was calculated for each of the 15 source-hydrophone pairs. Time differences ranged from 1.32 ms (35 m source depth, 45.15 m hydrophone depth) through 1.88 ms (35 m source depth, 25.4 m hydrophone depth). These arrival time differences relate to the sediment sound speed and thickness. The square of the observed difference and modelled difference assuming a specific sediment depth and sound speed was determined for each source-hydrophone geometry. The sum over all source-hydrophone pairs:

$$\sum ([t_{sb} - t_b]_{\text{obs}} - [t_{sb} - t_b]_{\text{mod}})^2, \quad (4.1)$$

is plotted versus sediment thickness and sound speed in Figure 4.9, and exhibits a line of minima (line of deepest blue extending from 0 m sediment thickness at 1500 m/s sediment sound speed, through 33 m sediment thickness at 1900 m/s sediment sound speed) showing the optimal combination of sediment sound speed and layer thickness. Ideally a minimum point corresponding to a single sound speed and sediment thickness would have been

4. EXPERIMENTAL ENVIRONMENT

obtained, but the parameters are coupled here because the time difference is related to the layer thickness divided by sound speed. A larger angular coverage of the different geometries would create a better determined minimum.

Although a definite minimum could not be obtained, bounds on the sediment thickness can still be obtained for the sound speeds estimated in Section 4.2.2. Based on Figure 4.9, if a sound speed of 1590–1650 m/s is assumed, a sediment thickness of 5–11 m is estimated, which is significantly lower than the thickness values of just over 20 m predicted by others [71, 72, 79]. However, Jiang and Chapman [71] suggest a negative gradient sound speed in the sediment, and this could give a slightly larger inverted sediment thickness. Ideally the sub-bottom arrival inversion would search over sediment thickness, sediment sound speed at the top, and sound speed slope within the sediment, but insufficient data are available to successfully search over multiple variables.

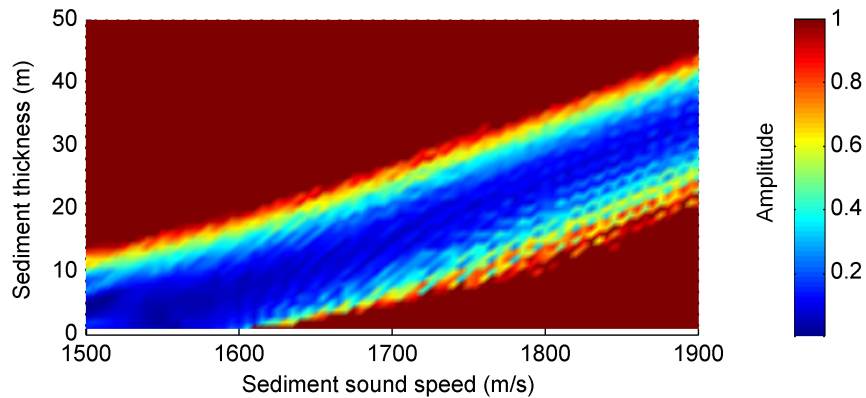


Figure 4.9: The square of the difference between the measured bottom and sub-bottom time differences, and the modelled values, is summed over all source-hydrophone geometries, and the result is threshold clipped to 3.2% of the maximum so that low amplitude structure can be better observed. The amplitude is normalised to the threshold value.

4.2.4 Conclusion

The ocean environment of the SW06 experiment was characterised by a strong thermocline and significant spatiotemporal variability. The resulting direct path acoustic field is shown to consist of multi-path interference, with high sensitivity to ocean variations. It is therefore difficult to extract accurate reflection coefficient information from the acoustic data. Attempts to do so provided, at best, approximate values.

An inversion based on time differences between bottom reflected and sub-bottom arrival times estimated the relationship between sediment sound speed and sediment thickness; however limited angular coverage of the ray paths prevented decoupling of these variables.

Simulated data will be used to compare with and support experimental results in Chapters 5 and 6. If the inversion results obtained here had been more conclusive, they could have been used to specify sediment properties for the simulation input environments, but given that they are not, it was decided that sediment properties would be better estimated from nearby sediment grab sample data [73]. All simulated data in the upcoming chapters will therefore use sediment property estimates based upon grab sample data.

Chapter 5

Ship Dominated Ambient Noise Cross-correlation

The high sea states and wind conditions created by Tropical Storm Ernesto on September 2 2006 created an opportunity to explore underwater noise fields with unusual characteristics. Within this chapter cross-correlations of ship dominated 20–100 Hz noise collected on three L-shaped arrays from August 31 to September 3 2006 are considered in detail. In particular, the applicability of common time and frequency domain preprocessing techniques to ship dominated ambient noise cross-correlation, the use of various receiver geometric configurations, and the effect of temporal variations on the cross-correlations, are all investigated. Knowledge of these is necessary in order not just to obtain good approximations to the Green's function from cross-correlation of ship dominated ambient noise, but also to understand the limitations of these approximations. The data were collected using the equipment at the locations described in Chapter 4.

A significant proportion of the work in this chapter has been submitted for publication in JASA [26].

5.1 Introduction

Although ocean acoustic interferometry (OAI) theory prescribes a uniform noise distribution, good approximations of the arrival structure of the actual Green's function can still be obtained from the cross-correlation time-derivative, termed the *empirical Green's function approximation* (EGFA), even when the distribution is not completely uniform, as demonstrated in the seismic literature [11, 12, 80]. At any time the cross-correlation of the data analysed from the experiments here tends to be dominated by one or two nearby ships, and therefore in order to obtain a cross-correlation that does not have directional bias, the time period over which the cross-correlation is performed must be sufficiently long such that several ship tracks that pass through the end-fire region are included [25]. When this is not the case spurious precursory arrivals corresponding to cross-correlations between paths from directions that are more densely sampled are apparent in the summed cross-correlation.

During Tropical Storm Ernesto most ships in the vicinity of the experimental area left the region. Thus, the shipping noise field was dominated by distant vessels. The reduced local shipping traffic, along with elevated wind and sea state conditions, meant that a greater amount of acoustic energy in the ocean at low frequencies was from both local and distant breaking waves, and distant shipping, than at other times. The overall acoustic energy levels were also higher. Because of the higher signal levels and the more uniform directivity of the shipping noise field, the arrival-time structure of EGFAs for low frequency cross-correlations of data recorded during the storm should more closely match that of the actual Green's functions between the hydrophones than during calmer periods.

The temporal characteristics of the ocean are non-stationary. This suggests that cross-correlations over short time periods, such as a few minutes, are optimal if instantaneous EGFAs are desired. However, the need to average over multiple ship tracks requires longer cross-correlation times, and hence cross-correlations that represent the 'average' EGFA over long time

periods of 24 hours are determined here. The theory assumes that sources all have the same amplitude and frequency content. Nearby ships tend to be louder, and larger ships have spectra that are dominated by lower frequencies. Time and frequency preprocessing are carried out to minimise these effects. The theory also assumes that ships move along a regular path at constant velocity. Ships that change velocity or have sharp changes in direction will degrade the EGFA. A ship that remains stationary in one location for a long time period is shown to result in a spurious peak at the corresponding time.

Cross-correlations between different sets of hydrophones within each array are compared, and it is shown that the cross-correlation yields direct and surface reflected paths between horizontal line array (HLA) hydrophones, and that bottom-surface reflected paths between HLA and vertical line array (VLA) hydrophones can be determined. Due to the long wavelengths considered, no attempt is made to determine sediment paths. Cross-correlations for equi-spaced hydrophones in an HLA are shown to have relatively little variation in amplitude and frequency, particularly at the cross-correlation peaks. Summing the cross-correlations between equally spaced pairs is shown to increase the signal-to-noise ratio (SNR). Temporal characteristics of the cross-correlations are also examined, and cross-correlations from calm periods are compared to those obtained from data collected during the tropical storm.

5.2 Theory

At frequencies above a few hundred Hertz the ocean sound field is dominated by surface noises from ocean waves [22–24]. At frequencies below about 100 Hz the noise field is dominated by shipping noise [22, 23]. Nearby shipping favours higher grazing angles between the acoustic paths and the horizontal, while distant shipping favours more horizontally travelling wavefronts. Noise in the frequency range 20–100 Hz is considered here. If it is

assumed that ship noise can be modelled as a set of sources that are uniformly and densely distributed within a horizontal plane near the surface of a waveguide, then the cross-correlation between two receivers can be derived following the stationary phase methodologies of Section 3.1 and Refs. [30] and [69]. The cross-correlation of the signals recorded at two receivers, A and B , is, from Eq. (3.4):

$$C_{AB}(\omega) = |\rho S(\omega)|^2 n \iint G(\mathbf{r}_A, \mathbf{r}_S) G^*(\mathbf{r}_B, \mathbf{r}_S) dx dy, \quad (5.1)$$

where $S(\omega)$ is the ship source spectrum, ρ is the density of the medium, n is the number of sources per unit area, $G(\mathbf{r}_\psi, \mathbf{r}_S)$ is the Green's function between the source, S , and receiver, ψ , $*$ denotes the complex conjugate, and x and y are the horizontal axes parallel and perpendicular to the vertical plane containing A and B respectively.

The full Green's function at each receiver can be written as the superposition of direct and reflected waves. For a uniform sound speed waveguide, bounded by a free surface and a bottom with reflection coefficient Γ , the Green's function between the source, S , and receiver, ψ , can be expressed as a sum of free-field Green's functions in the same manner as for Eq. (3.6) [1, 69]:

$$G(\mathbf{r}_\psi, \mathbf{r}_S) = \sum_{b_\psi=0}^{\infty} \Gamma^{b_\psi} G_f \left(\sqrt{(x - x_\psi)^2 + y^2 + (2b_\psi D + z \pm z_\psi)^2} \right) + \sum_{b_\psi=1}^{\infty} \Gamma^{b_\psi} G_f \left(\sqrt{(x - x_\psi)^2 + y^2 + (2b_\psi D - z \pm z_\psi)^2} \right), \quad (5.2)$$

where b_ψ is the number of bottom bounces for a given path, D is the depth of the waveguide, the $y = 0$ horizontal axis is defined as that which contains both A and B , and $G_f(R) = \frac{e^{ikR}}{4\pi R}$ is the 3D Green's function within a homogeneous medium, where k is the wave number and R is the total distance that a particular wave travels. The first term on the RHS of Eq. (5.2) includes all up-going waves, and the second term includes all down-going waves as measured from the source.

Inserting Eq. (5.2) into Eq. (5.1) yields a cross-correlation expression that consists of the sum of the integrals of all possible combinations of

the interaction between any path to the first receiver, and any path to the second. Consider any of these individual interactions. Substitution of Eq. (5.2) into Eq. (5.1), that is, cross-correlation between two arbitrary paths, yields [30, 69]

$$C_{AB}(\omega) = |\rho S(\omega)|^2 n \frac{\Gamma^{b_A+b_B}}{(4\pi)^2} \iint \frac{e^{ik(L_A-L_B)}}{L_A L_B} dx dy, \quad (5.3)$$

where b_ψ is the number of bottom bounces for the path to ψ , and

$$L_\psi = \sqrt{(x - x_\psi)^2 + y^2 + (2b_\psi D \pm z \pm z_\psi)^2}, \quad (5.4)$$

is the length of the given path between the source, S , and receiver, ψ .

Application of the method of stationary phase to Eq. (5.3) [15, 30, 68, 69], and summation over all stationary points, yields

$$C_{AB}(\omega) = in |S(\omega)|^2 \sum_{\chi_s} \left(\frac{\Gamma^{b_A+b_B} c \rho}{2\omega \cos \theta} G_f(R(\chi_s)) \right), \quad (5.5)$$

where c is the wave velocity, f is the acoustic frequency, $\omega = 2\pi f$ is the angular frequency, θ is the acute angle between the ray path and the vertical, and χ_s are the stationary points. Note that the stationary points satisfy the relationship $\theta_A = \pm\theta_B$. The positive relationship between θ_A and θ_B only occurs when the path to the furthest receiver passes through the closer receiver, hence the relationship between the summed cross-correlations and the Green's function between the receivers. The negative relationship corresponds to stationary-phase contributions from cross-correlations between a wave that initially undergoes a surface reflection, and one that does not [15, 69]. Since ship sources are near the ocean surface, these spurious arrivals will converge to almost the same time delay as the true Green's function paths, and due to the long wavelengths, will not be observed as separate peaks. The theory presented here has neglected curvature of ray paths due to refraction, but it has been shown by others [30] that the stationary phase argument generalises to a heterogenous medium with smooth velocity variations.

The cross-correlation in Eq. (5.5) can therefore be seen to produce an amplitude and phase shaded Green’s function. The amplitude shading is dependent on the travel path through the $\Gamma^{b_A+b_B}$ and $\cos\theta$ terms, and also contains both constant and frequency dependent components. The $1/\omega$ factor phase shading in Eq. (5.5) means that the time domain Green’s function is proportional to the derivative of the summed cross-correlations [11, 13, 15, 69]:

$$\frac{\partial C_{AB}(t)}{\partial t} \simeq - [G_{AB}(t) - G_{AB}(-t)]. \quad (5.6)$$

The raw cross-correlation, rather than its time derivative, is often used as an approximation to the Green’s function [25, 56, 65, 66], and for a mid-high frequency finite bandwidth signal this can be a good approximation since the cross-correlation peaks at roughly the same time as its derivative.

5.3 Experiment

Data considered in this chapter were collected from August 31 through September 3 on the three L-shaped arrays: SWAMI52, SWAMI32, and Shark. Array locations and orientations are shown in Figure 5.1(a), and configurations are detailed in Table 5.1. The HLAs were all located on the seafloor. All VLA hydrophones and the Shark HLA hydrophones are evenly spaced. SWAMI52 inter-hydrophone distances increase from the centre, and SWAMI32 HLA inter-hydrophone distances increase from the hydrophone 13 (H-13) end respectively. The exact HLA hydrophone spacing of each SWAMI array is detailed in Appendix B.1.2. A sketch of the SWAMI52 array geometry is shown in Figure 5.1(b). SSPs that were recorded near SWAMI52 on August 30 and September 6 are shown in Figure 5.1(c).

Tropical Storm Ernesto created large sea states and high winds. The wind direction and speed from August 31 through September 3 are shown in Figure 5.1(d)–(e). Predominantly easterly winds gradually built up over August 31 and September 1 to a 20 m/s peak early on September 2, and then remained high until late in the day, when they dropped rapidly once

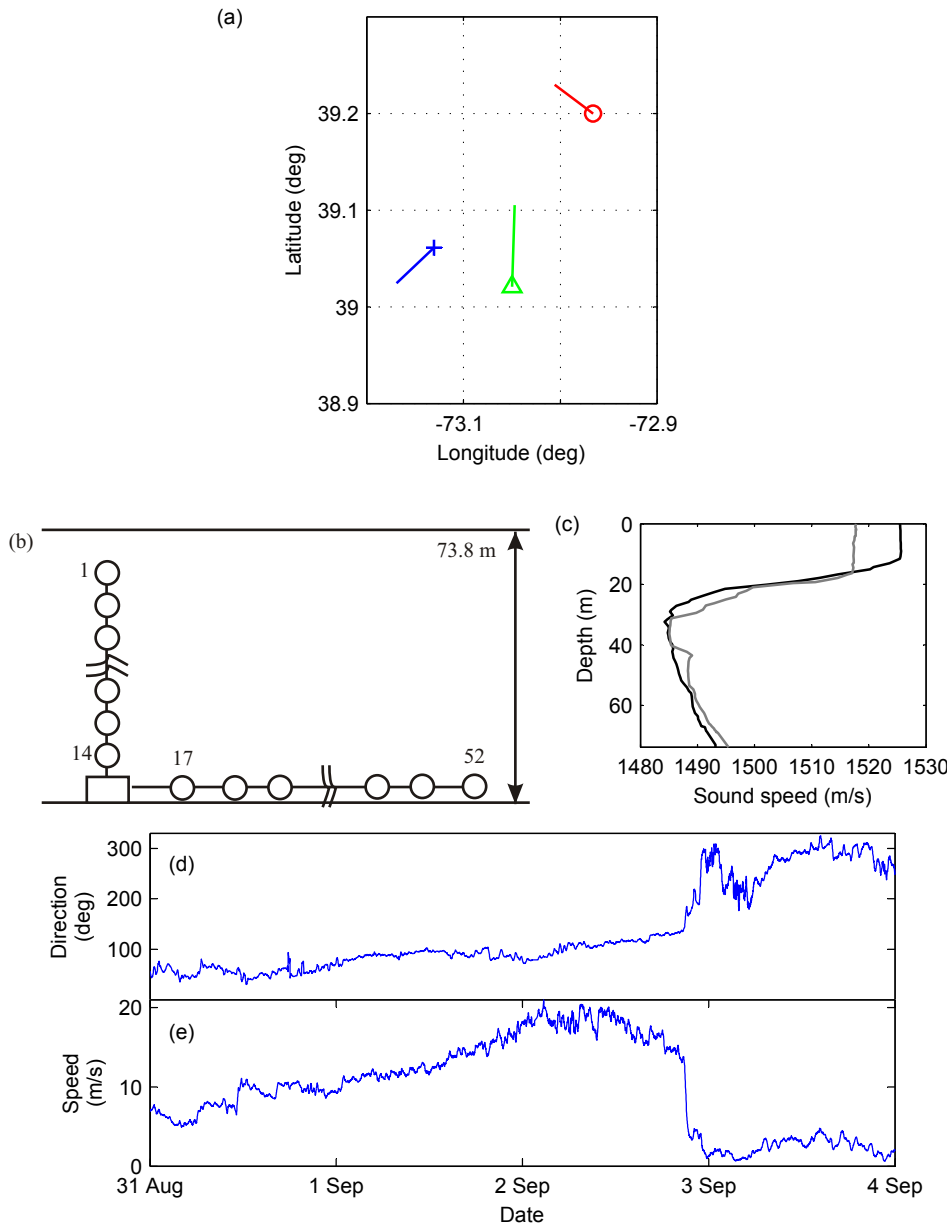


Figure 5.1: (a) The relative VLA locations of SWAMI52 (\circ), SWAMI32 ($+$), and Shark (\triangle). The lines departing each VLA show the HLA orientation. The array length is scaled by a factor of 20. (b) SWAMI52 array geometry and hydrophone numbering system. (c) SSPs near SWAMI52 for August 30 (black) and September 6 (grey). (d) Wind direction and (e) wind speed, from R/V *Knorr* ship records, from August 31 to end of September 3.

5. SHIP DOMINATED AMBIENT NOISE CROSS-CORRELATION

Table 5.1: Details of array configurations. ^aLowest numbered hydrophone is uppermost in the array. Extra hydrophones tied off just above frame (SWAMI52: H-15 and H-16, SWAMI32: H-11 and H-12, Shark: H-13–H-15). ^bLowest numbered hydrophone is closest to array except for Shark, which is opposite. ^cData from H-15 and H-46 were discarded due to inconsistencies with other data.

	Water depth (m)	Number of hydrophones	VLA		HLA	
			Length (m)	Hydrophones ^a	Length (m)	Hydrophones ^b
SWAMI52	73.8	52	56.81	1:14	230	17:52
SWAMI32	68.5	32	53.55	1:10	256	13:32
Shark	79	48	64.25	0:12	465	16:47 ^c

the storm had passed. The decrease in speed was accompanied by a change in wind direction to south and west.

On September 2 several of the SWAMI32 channels switched, as described in detail in Chapter 7. Corrections for this were applied to the relevant data presented here.

5.4 Analysis of data preprocessing methods

Time and frequency domain preprocessing methods were applied to the raw data to emphasise broadband ocean noise. The preprocessing techniques considered here were analysed using data collected on SWAMI52 throughout September 2 (Zulu time). No towed source experiments were undertaken on this day, because of Ernesto, and therefore ocean noise over a large frequency bandwidth could be considered. The data were stored and analysed in 140 portions, each 10 minutes and 14 seconds duration, or 10:14 min.

Short (10:14 min) cross-correlations were unstable at shallow depths above the thermocline, likely due to sound speed fluctuations resulting from elevated levels of swell and mixing due to Ernesto. If the noise field had been isotropic and sufficiently strong, cross-correlations could have been performed over periods that were sufficiently short for the environment to

be considered stationary. The temporal change in cross-correlation could then have been related to environmental changes, in particular changes in temperature in the upper waveguide, and tidal changes. However, the dominant noise here was from discrete ships, and therefore the cross-correlations had to be performed over a long time period so that specific sources did not dominate (see Section 5.6). Cross-correlations were therefore performed over the entire day. Direct path propagation between hydrophones lower in the water column would not have changed significantly over this time, but any propagation paths that passed through the thermocline region may have. The resulting EGFA is therefore an approximation of the ‘average’ Green’s function over the day.

5.4.1 Removal of main contamination

Depending upon the particular time interval, some of the September 2 data exhibited one or more of the following: high amplitude mid-frequency signal from fixed location sound sources, amplitude clipping, and low frequency energy bursts. Spectrograms and time series of data collected on September 2, showing examples of each of these aberrations, are shown in Figure 5.2.

Three fixed location sound source signals are observed in Figure 5.2(a). A 300 Hz 1.5-second duration LFM (linear frequency modulated) signal with a 60 Hz bandwidth is visible in the spectrogram as ramps that cut on and off at regular intervals. The LFM signal is bounded above and below by two continuous horizontal lines of high amplitude, created by phase encoded signals at 224 Hz and 400 Hz, both with 16 Hz bandwidth. The amplitude of the time-series is seen to spike when the LFM signal is active.

An example of amplitude clipping is shown in Figure 5.2(b). The frequency of the signal that exceeds the maximum allowable amplitude is low, and since the spectrogram is normalised to the maximum value at any given time, the apparent amplitude of all higher frequencies is reduced, yielding vertical green and yellow lines in the spectrogram. A low frequency energy burst is visible in Figure 5.2(c) at a time of 50 seconds as low frequency

energy smearing into the higher frequencies in the spectrogram, with a corresponding increase in amplitude in the time-domain.

Contaminations other than those shown in Figure 5.2 may also have been present. Electrical noise could manifest as high amplitude tonals at the hydrophone operation frequency and its harmonics, and/or as Gaussian noise across a wider frequency band. Impact noise from a fish colliding with a hydrophone or something else tapping the hydrophone array would likely be observed as sharp amplitude peaks in the time domain, and energy would be smeared across the frequency spectrum at this time. Signals from any ships in the vicinity of the array throughout the day would be recorded as discrete high amplitude tonals.

All discrete signals have a difference in direct path length to each hydrophone which is less than or equal to the direct path between the hydrophones, and may be visible in the cross-correlation as spurious precursory arrivals. Preprocessing, which includes choice of bandwidth as well as time and frequency domain normalisation, ameliorates this effect (see Sections 5.4.2–5.4.4).

5.4.2 Spectra and coherence

Only signals that are received by both hydrophones will sum coherently to give a peak in the cross-correlation function. Spectra give some information for selection of an appropriate bandwidth since signals of very low amplitude or low SNR will generally have poor coherence, which should be avoided; however, higher amplitude does not guarantee higher coherence.

Coherence, γ , which gives a measure of the degree of linear dependence between two random variables, X and Y , as a function of frequency, f , is defined by

$$\gamma^2(f) = \frac{|E(X^*(f)Y(f))|^2}{E(|X(f)|)E(|Y(f)|)}, \quad (5.7)$$

where $|X(f)|$ is the absolute magnitude of $X(f)$, $*$ denotes the complex conjugate, and $E(X)$ denotes the expected value of a random variable X .

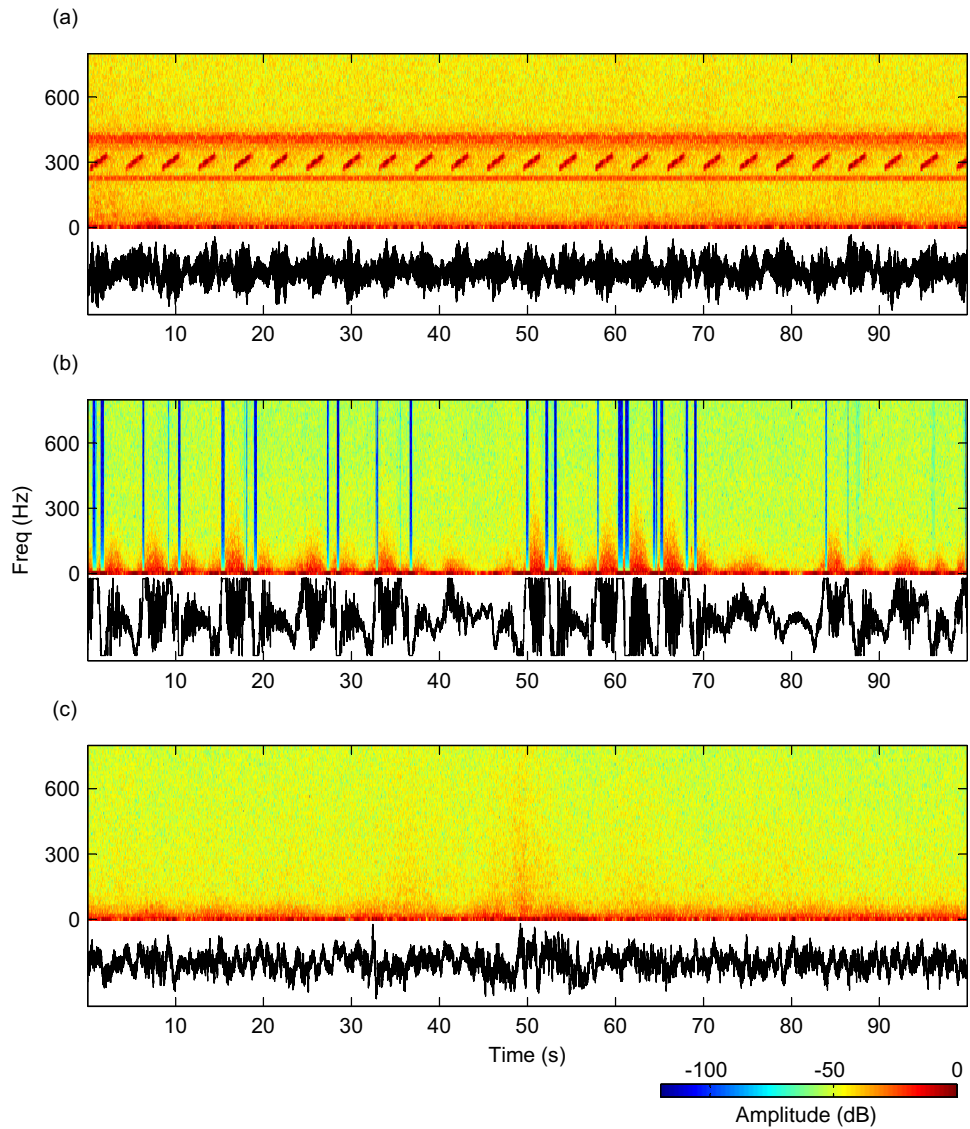


Figure 5.2: Spectrograms (upper) and time-series (lower) of September 2 data: (a) signal dominated by mid-frequency fixed sound sources (H-11, 0:29:25 Z), (b) clipped signal (H-1, 0:08:56 Z), and (c) energy dominated by low frequency sources (H-11, 12:46:39 Z). Low frequency energy bursts are observable in (b)–(c). Spectrograms (dB) are normalised to the maximum amplitude at each time.

Both the signal amplitude and coherence are considered here.

Since the underlying statistics of the data are non-stationary, spectra and coherence over short periods are examined. Spectrograms of the signals received by H-52, and coherograms (coherence plotted as a function of frequency and time) of the signals recorded on H-52 and H-40, which are separated by 97.74 m, are shown in Figure 5.3. The mean spectra and coherence for 1:33 min intervals were calculated using 2 second Hanning windowed data segments and 50% overlap. The mean of the individual spectra and coherences are shown on the far right.

High amplitude signals with a corresponding high coherence are apparent at regular time intervals in the 200–410 Hz frequency range, as shown in Figure 5.3(a)–(b). These signals are from the three fixed location sound sources described in detail in Section 5.4.1, which were only active for the first ten minutes of every half hour. Low signal amplitudes and coherence are observed at frequencies above 420 Hz, and also from 100–200 Hz. Below 100 Hz both the amplitude and coherence of the received signals are higher, as shown in Figure 5.3(c). This is expected since lower frequency ocean noise will propagate more coherently over long distances. A banded structure consisting of high amplitude tonals is observed in both the low frequency spectrogram and coherogram, Figure 5.3(c)–(d), at a range of frequencies at different times throughout the day (e.g., 1:30–3:30 Z and 13:30–15:30 Z). This banded structure is indicative of the sound field being dominated by ship noise at low frequencies. The exact frequency content of the signals emitted by each ship is dependent upon the propeller frequency as well as other characteristic properties of the ship, and therefore the frequency content of the banded structure changes throughout the day as different ships dominate the overall sound field.

Since the signals, apart from those from the fixed sources, exhibit negligible amplitude and coherence above 100 Hz, the data were bandpass filtered to 20–100 Hz. The lower limit of 20 Hz was selected as frequencies below this have insufficient resolution over the distances in question.

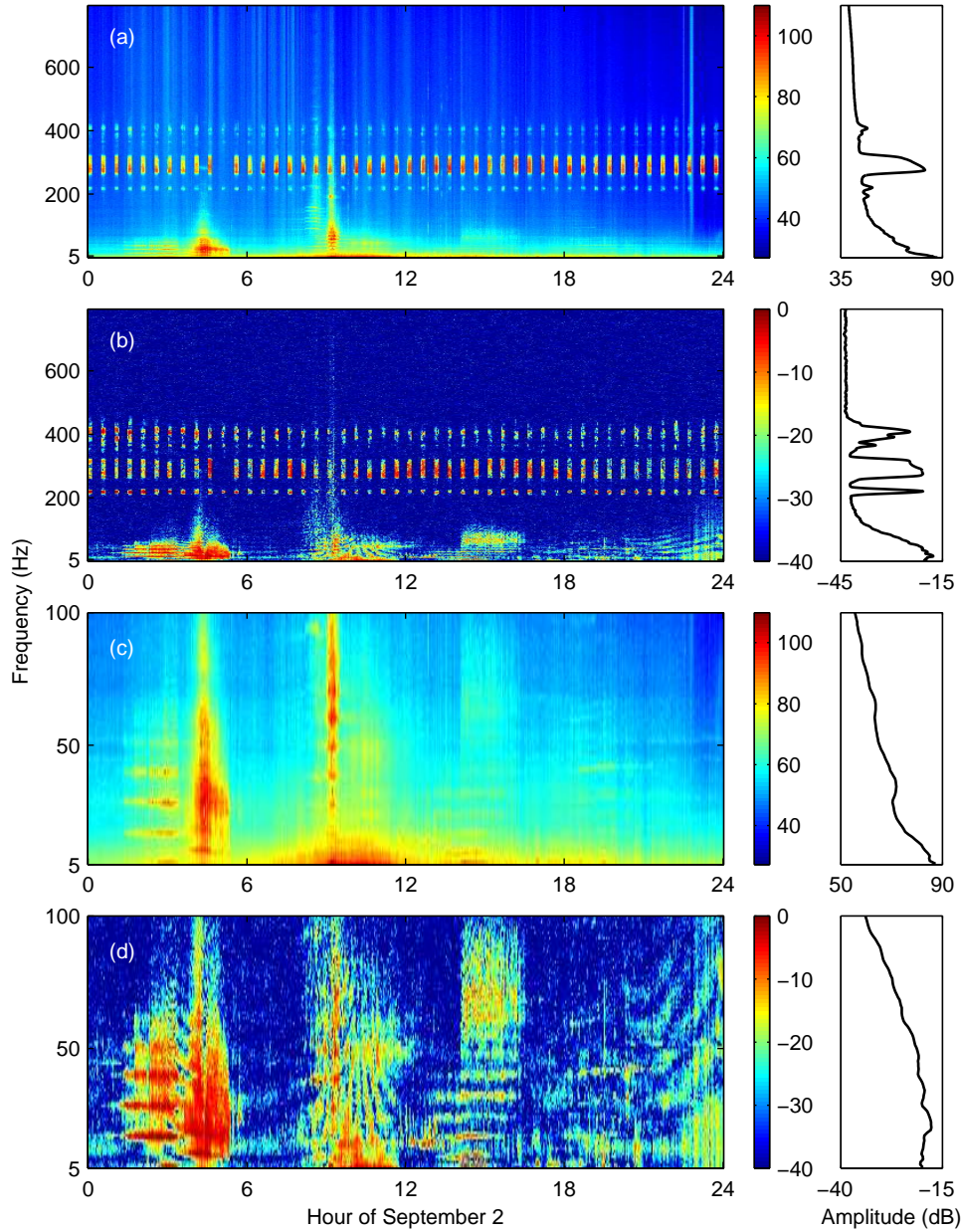


Figure 5.3: Spectrograms (dB) of signals recorded on H-52, using the entire September 2 data: (a) 5–800 Hz and (c) 5–100 Hz. Coherograms (dB relative to unity linear coherence) of the data recorded on H-52 and H-40: (b) 5–800 Hz and (d) 5–100 Hz. The average of the individual spectra or coherences is plotted to the right of each figure.

5.4.3 Frequency domain normalisation

Frequency domain normalisation has the dual purpose of broadening the signal bandwidth by placing higher emphasis on low amplitude signals, and of decreasing the negative impact of discrete sources. For the purpose of comparing frequency domain normalisation methods, the effects of erroneous temporal peaks were minimised by setting all values of amplitude greater than 50% of the signal standard deviation to this value [16, 81], a process described as ‘threshold clipping’, one of the time domain normalisation techniques that is discussed in detail in Section 5.4.4.

Normalisation methods

Cross-correlations were performed using five different frequency domain preprocessing methods:

- (a) no frequency domain preprocessing;
- (b) bandpass filter, no frequency domain amplitude normalisation;
- (c) bandpass filter and whiten by normalising over the entire frequency range (20–100 Hz), known as absolute whitening;
- (d) bandpass filter and normalise by a smoothed version of the amplitude spectrum, known as smoothed whitening; and
- (e) bandpass filter and partially normalise the data by the sum of the signal magnitude at that frequency and a mean amplitude dependent constant:

$$S(\omega) = \frac{S(\omega)}{|S(\omega)| + \beta \overline{|S|}}, \quad (5.8)$$

where $\overline{|S|}$ is the mean amplitude over the entire frequency range, and β determines the degree to which the data are whitened ($\beta = 0$ is equivalent to absolute whitening (c), and $\beta = \infty$ to no normalisation(b)).

The effect of applying each normalisation technique to H-40 data can be seen in Figure 5.4. Bandpass filtering without frequency normalisation, method (b), maintains the general characteristics of the amplitude peaks and decay with frequency seen in the raw data, method (a). Absolute and smoothed whitening, methods (c) and (d) respectively, give approximately equal energy across the frequency band. Partial whitening, method (e), reduces extraneous tonals, but also places emphasis on signals of higher coherence (lower frequency).

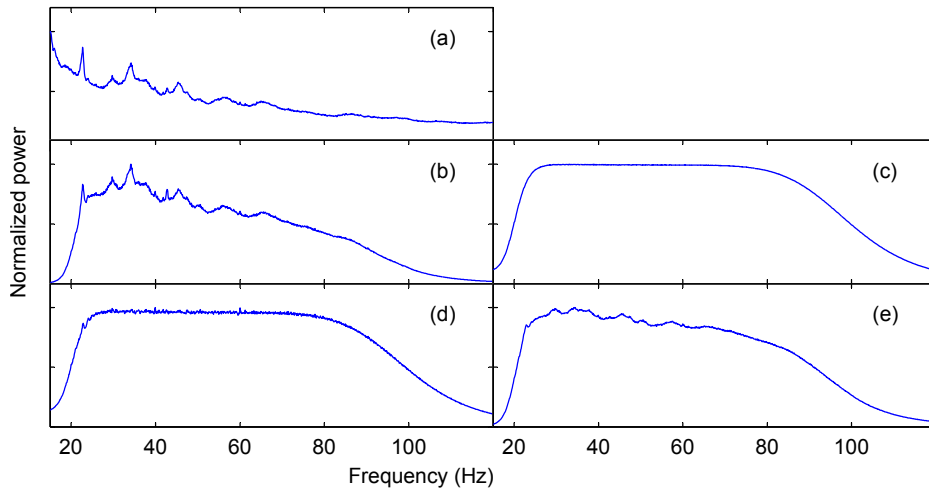


Figure 5.4: Normalised (linear) spectra of the September 2 signal recorded on H-40 (a) before pre-filtering, and (b)–(e) after pre-filtering. Pre-filtering methods are (b) bandpass and time domain filtering only, (c) absolute whitening, (d) smoothed whitening, and (e) partial whitening ($\beta = 1$).

Cross-correlations

Data were pre-processed using each of the methods outlined in the previous section. Individual cross-correlations were calculated and normalised by their peak value before summing so that the overall cross-correlation is not dominated by high amplitude cross-correlations from only part of the day. The cross-correlations between H-52 (tail-end HLA hydrophone) and all

other hydrophones, summed over September 2, using smoothed whitening filtering, method (d), are shown in Figure 5.5(a).

The HLA cross-correlations are plotted as a function of distance from H-52. The VLA cross-correlations, which are offset by the horizontal distance between H-52 and the VLA hydrophones, are plotted as a function of height from the seafloor (note that the two vertical axes have different scales). The direct and surface reflected travel times between each hydrophone, which are shown as dotted lines, were determined using OASES [49]. Peaks in the cross-correlation are evident at both the direct and surface reflected travel times. The EGFA envelope in Figure 5.5(b), on a logarithmic scale, reveals the surface-bottom reflected path to the lower VLA hydrophones.

The EGFA envelope for the case of bandpass filtering only, method (b), shown in Figure 5.5(c), shows only minor differences to that for smoothed whitening. Due to the higher proportion of low frequency energy, the arrivals are less sharp, and the background noise level is slightly higher. In addition, the surface reflected path is not as clear at the closer hydrophones (40–120 m). The raw signals have greater amplitude at lower frequency and this naturally assists the cross-correlation when no frequency domain normalisation is applied; the lower coherence signals are lower amplitude and will therefore have less overall influence upon the correlated signal. This explains why a reasonable cross-correlation can be determined when no spectral normalisation is performed. The EGFA envelope for no frequency domain filtering, method (a), shown in Figure 5.5(d), gives a poor representation of the Green's function. A low frequency signal below 20 Hz from the southeast dominates the cross-correlation to such an extent that only the direct acausal path is obtained.

The EGFA envelopes for absolute and partial whitening, methods (c) and (e), are not shown, but their characteristics lie between that of Figure 5.5(b) and (c). Smoothed whitening was selected as the optimal frequency domain filtering method for the data collected. Bensen *et al.* [62] compared no normalisation and smoothed whitening for cross-correlations

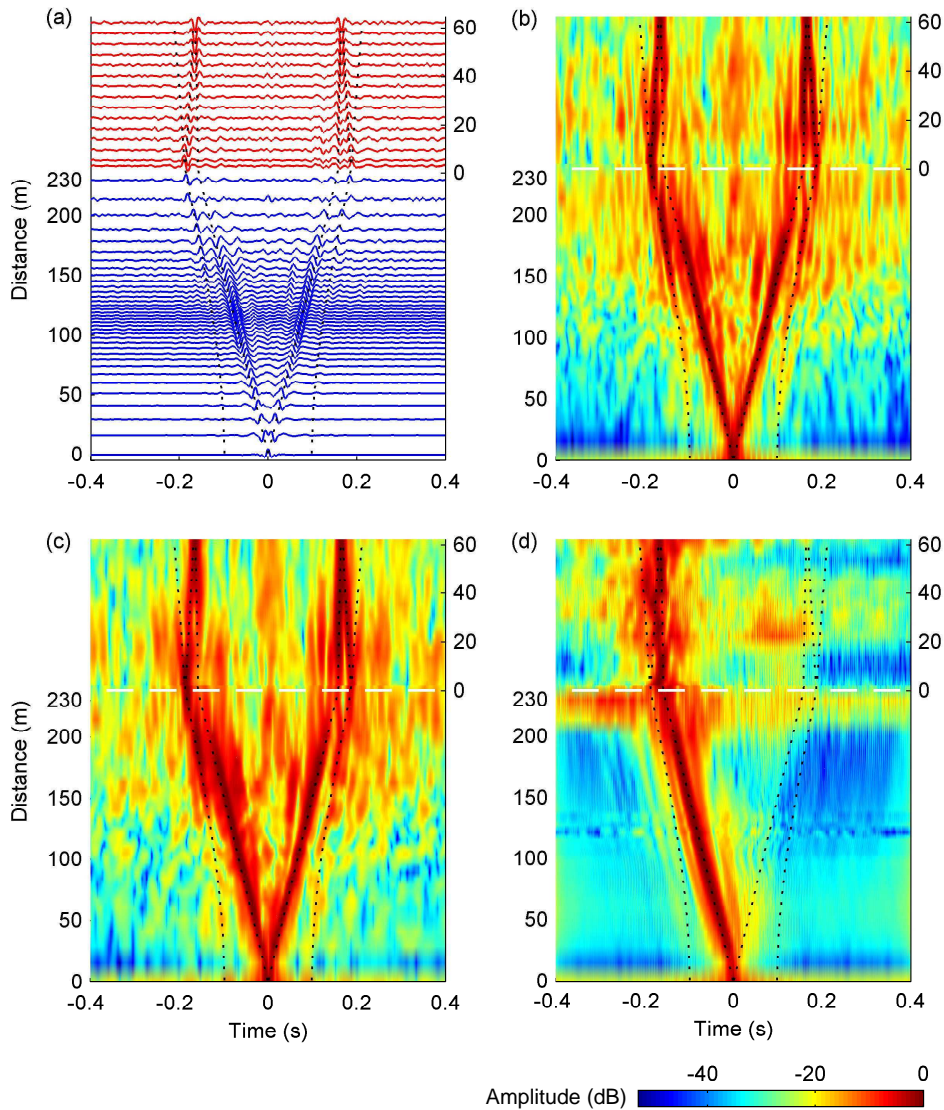


Figure 5.5: (a) Cross-correlations between H-52 and all other hydrophones for September 2 data using smoothed-whitening frequency filtering (20–100 Hz bandwidth). (b)–(d) EGFA envelopes (dB relative to maximum value): (b) with smoothed whitening (20–100 Hz bandwidth), (c) with no frequency normalisation (20–100 Hz bandwidth), and (d) with no frequency domain filtering or normalisation. The lower traces are cross-correlations with HLA hydrophones; their distances from the tail hydrophone (H-52) are shown on the left side axis. The upper traces are cross-correlations with VLA hydrophones; their vertical distances from the seafloor are shown on the right side axis, which is offset by the horizontal distance of the VLA from the HLA tail. The simulated travel times between the hydrophones were calculated using OASES and are overlaid as dotted lines.

of seismic data, which were created by different physical processes and have much lower frequencies. They found that the improvements gained by normalisation were substantially greater than for the data considered here.

The envelopes of the EGFAs generated using the various frequency domain normalisation techniques were compared here; however, it should be noted that because these normalisation methods are non-linear, not only the amplitude, but also the phase of the EGFAs are affected. The variations in phase due to the application of each technique were found to be small, and the only conclusive evidence that could be ascertained was that the greater the degree of non-linearity in the normalisation, the greater the effect on the phase of the obtained arrivals. The method of smoothed whitening used here has only a relatively small degree of non-linearity, and therefore should not significantly affect the arrival time.

Appropriate selection of the data bandwidth affected the result more than any frequency domain normalisation because above the 100 Hz low-pass frequency the cross-correlation has almost no coherence, and therefore inclusion of higher frequencies adds to the noise floor. If no frequency domain filtering or normalisation is applied this added noise is minimal, since the amplitude is negligible at higher frequencies. However, if the data are whitened but not bandpass filtered, signals of low-coherence will be emphasised, and the resulting cross-correlation sum will be dominated by noise that requires very long averaging times to remove.

5.4.4 Time domain normalisation

Theory

Various methods of time-domain normalisation have been used by others. Campillo and Paul [12] cross-correlated seismic coda. Since the coda decays over time, the overall cross-correlation would be naturally biased toward the earlier part of the coda. To compensate for this they used short segments of data, performed the cross-correlations, normalised these, and then summed

them. They reported results similar to those obtained by others [82] who had used one-bit normalisation, where only the sign (phase) of the waveform, not the amplitude, is retained. One-bit time reversal normalisation yields a higher SNR than classical time reversal in some multiple scattering or reverberating media [59, 82] since all scattering paths are equally weighted. Without one-bit normalisation longer scattering paths would have a reduced amplitude in the cross-correlation. A similar argument holds for cross-correlation analysis and therefore one-bit normalisation is often used [27, 59, 83]. Another method of time domain normalisation is to clip all signals above a certain threshold [81]. This minimises the effect of energy bursts, but also maintains more information than 1-bit normalisation. Gerstoft *et al.* [16] set their threshold as the minimum of the standard deviations measured over each day. For their data set this gave identical results to one-bit normalisation. Bensen *et al.* [62] and Yang *et al.* [18] used temporally variable weighting functions. They claimed that these retain more small amplitude information and also allow for flexibility in defining the amplitude normalisation in particular frequency bands.

Comparisons of time domain normalisation techniques by Bensen *et al.* [62] concerned seismic noise, which is often dominated by high amplitude earthquakes. Since ocean noise is dominated by other physical processes, which display different characteristics, the effect of these normalisation techniques upon the resulting cross-correlations will also differ. A comparative study of the applicability of several techniques to the current data set was therefore undertaken. The normalisation techniques that were compared are:

- no normalisation;
- correlate over short intervals with some degree of overlap, normalise the cross-correlations and then sum;
- clip the signal to a threshold;
- one-bit (two level) normalisation;

- use of a rectangular central temporally variable weighting (RCTVW) function; and
- use of an exponential central temporally variable weighting (ECTVW) function.

Performing no normalisation in the time domain sets a clear benchmark for the five other techniques. Cross-correlating over short intervals and then summing the normalised cross-correlations is more effective for shorter intervals. Since the greatest distance between any two hydrophones is 230 m, the direct path should be observable in under 0.2 s; hence, to ensure sufficient time for reverberant paths to be captured, 0.4 s data segments were used, with 33 % overlap.

A threshold of σ , one standard deviation, was chosen as the level to which the signal would be clipped for normalisation technique (c). It was noted that the results were not highly sensitive to the chosen threshold.

One-bit normalisation, which uses only the sign of the signal, increases the signal-to-noise ratio of the data:

$$s_n(t) = \begin{cases} -1 & \text{if } s(t) < 0 \\ 1 & \text{if } s(t) > 0, \end{cases} \quad (5.9)$$

where $s(t)$ is the raw signal at time t , and subscript n denotes the normalised signal.

RCTVW and ECTVW are the most computationally time intensive. RCTVW normalises each point by the sum of the unweighted mean of the absolute value of N preceding and succeeding values ($2N + 1$ points overall):

$$s_n(t) = \frac{s(t)}{w(t)}, \quad (5.10)$$

where

$$\begin{aligned} w(t) &= \sum_{\tau=t-N}^{t+N} |s(\tau)| \\ &= w(t-1) - |s(t-N-1)| + |s(t+N)|. \end{aligned} \quad (5.11)$$

A normalisation window of 0.05 s, which is the time interval of the maximum period, corresponding to the minimum frequency of 20 Hz, was found to be suitable. A normalisation vector length of $2N + 1 = 257$ was therefore used.

ECTVW places more emphasis on points closer to the point of interest. It normalises in the same manner as RCTVW, the only difference being that it applies a weighting filter with an amplitude that decreases exponentially in both directions from the data point of interest:

$$\begin{aligned}
 w(t) = & (1 - \alpha)^N |s(t - N)| + \dots \\
 & + (1 - \alpha) |s(t - 1)| + |s(t)| + (1 - \alpha) |s(t + 1)| + \dots \\
 & + (1 - \alpha)^N |s(t + N)|,
 \end{aligned} \tag{5.12}$$

where $\alpha = 2/(N + 1)$ is the exponential smoothing factor. In order to use previously calculated sums to determine subsequent weights, the exponential is split up into two parts, the increasing exponential prior to and including the point, and the decreasing exponential after the point. These are then summed to give the overall weighting.

Application to data

Example waveforms resulting from application of each time normalisation method to 2.5 s of H-40 data are shown in Figure 5.6. Higher energies are observed in the time period 1.4–2.1 s, as can be seen in Figure 5.6(a), and these amplitudes are all successfully reduced by the time-filtering methods, as shown in Figure 5.6(b)–(e). Normalisation technique (b) is not shown here as this normalisation is only applied after cross-correlating the data.

Cross-correlations and EGFA envelopes for September 2 for each time-normalisation method are shown in Figure 5.7(a)–(b). The same line style has been used in the figure for all results because they are too similar to be individually discerned. The horizontal distance between: (a) the HLA hydrophones H-52 and H-48, is 31.31 m; and (b) H-52 and H-8 (located in the VLA), is 230 m. Large cross-correlation peaks exist at the direct ray travel time, and smaller peaks at the surface reflected travel time. The

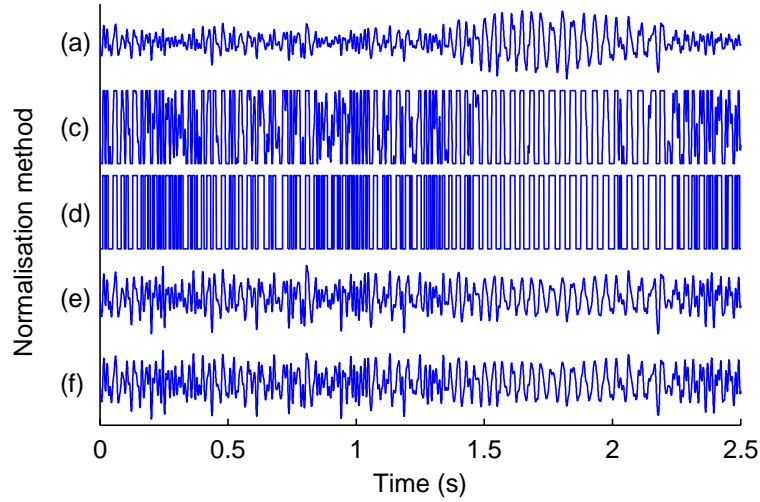


Figure 5.6: Preprocessed waveforms for 2.5 s of 20–100 Hz bandpass filtered data from H-40 (at 12:48:45 Z) with normalisation method: (a) none, (c) threshold clipping, (d) one-bit, (e) RCTVW, and (f) ECTVW.

background noise is consistently low, except for one high peak at a time just less than the positive direct arrival. This could be due to a non-uniform source distribution. For the two further spaced hydrophones shown in Figure 5.7(b), the EGFA envelope once again peaks at the direct and surface reflection travel times. A smaller peak can also be seen at the acausal surface-bottom travel time (i.e., the bottom-surface reflected path from H-8 to H-52). The signal-to-noise ratio is poorer than for the more closely spaced hydrophones, but this is to be expected since decay and spreading of signals increases with distance.

The results from Figure 5.7(a)–(b) suggest that time-normalisation has little influence on the cross-correlations for this data set. Time normalisation is important for seismic cross-correlations [61, 62] since otherwise the results can be dominated by earthquakes. Although the ocean noise field is not perfectly diffuse, there are no equivalently energetic events for the frequency band considered, and nearby shipping is minimal on September 2. This, combined with the intrinsic averaging introduced by summing over the entire day, are two reasons why time-domain normalisation shows

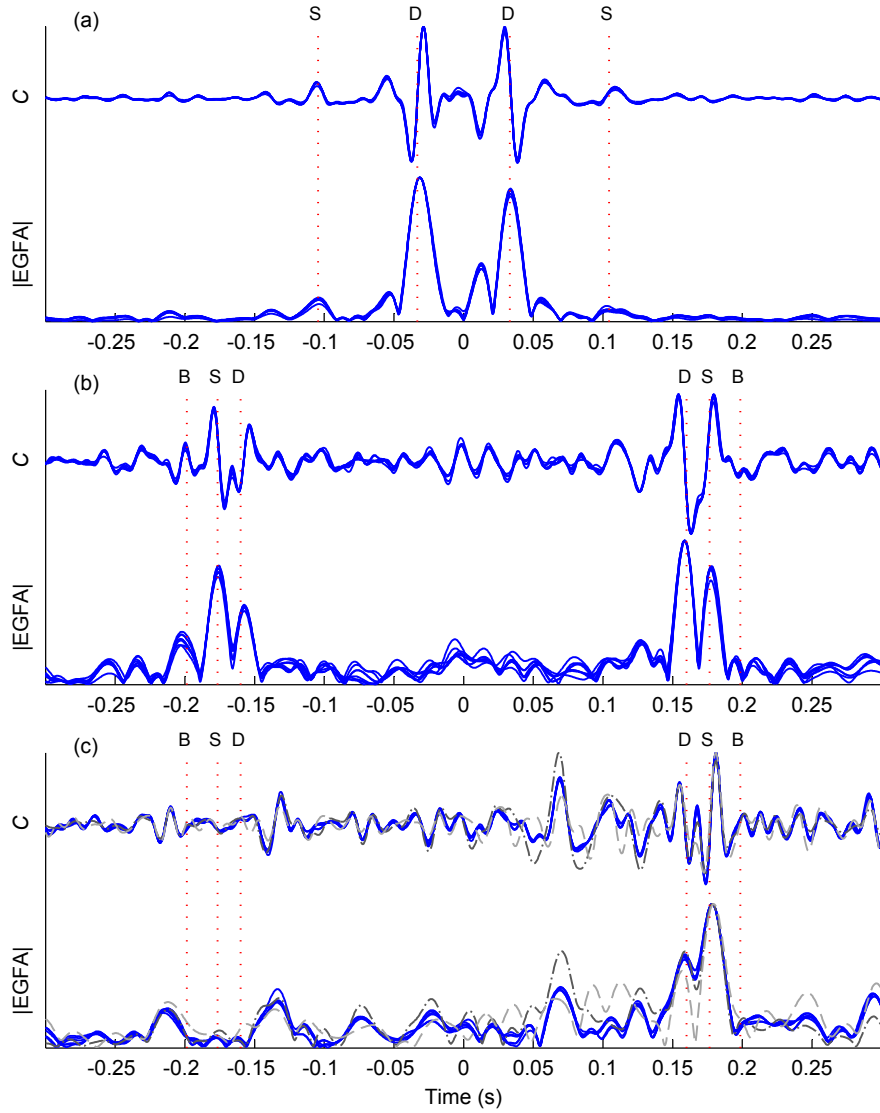


Figure 5.7: Summed cross-correlations, C , and EGFA envelopes, $|\text{EGFA}|$, for all time normalisation methods for H-52 and (a) H-48 (entire day with 51.32 m horizontal separation), (b) H-8 (entire day with 230 m horizontal separation), and (c) H-8 (10:24 min from 8:30 Z). Simulated travel times of direct (D), surface (S), and surface-bottom (B) paths are shown as vertical dotted lines. In (c) results for no normalisation and short interval cross-correlations are shown as dark grey dash-dotted and light grey dashed respectively.

negligible benefit here.

If the cross-correlations were carried out over a period that is insufficient to average-out energetic events, the benefits of normalisation would be greater. Consider the 10:14 min cross-correlation between H-52 and H-8 in Figure 5.7(c). The cross-correlations peak at the positive direct and surface reflected travel times only, indicating that the dominant sound field is from the tail-end of the array (the north-west direction). Distinct peaks seen at -0.22 , -0.14 , and 0.07 seconds are the result of discrete sources. Since high amplitude events, which are reduced in the normalisation process, are not averaged-out in the shorter cross-correlation time period, the cross-correlation and EGFA envelope without normalisation, method (a), and correlating over short periods and summing the normalised results, method (b), both have a higher noise level than the results for data that is normalised before cross-correlation.

Since time-domain normalisation techniques (c)–(f) all give similar results, and one-bit normalisation is the least computationally intensive, it was selected for further processing and analysis of the data.

The sum of the cross-correlations between H-52 and all other hydrophones for 20–100 Hz bandpassed, one-bit normalised, smoothed whitened September 2 data are shown in Figure 5.8(a). Since the Green’s function is related to the time-derivative of this (the EGFA), the flipped in time acausal EGFA, which is clearer than the causal signal, is plotted in Figure 5.8(b). The Green’s function, which was simulated using OASES and then convolved with a 20–100 Hz box car pulse, is shown in Figure 5.8(c) for comparison purposes. The assumed model sediment properties, $c = 1761$ m/s and $\rho = 1.69$ gm/cm³, were approximated from grab samples in the array vicinity [73]. In both cases the direct arrival peaks are positive and the reflected arrival peaks are negative, which is due to the phase change at the surface. The amplitudes are not exact, though this is expected since the acoustic energy is not equi-partitioned amongst all modes [84].

The EGFA envelope shown in Figure 5.8(d) shows the arrivals more

clearly. The surface-reflected arrivals are apparent for distances greater than about 50 m, as indicated by the peak in EGFA amplitude that occurs above 50 m in the figure at times corresponding to the second set of dotted arrivals on either side of zero time. They are not observable at closer ranges, where they would be more steep, because at these ranges the noise field is dominated by far-field horizontally travelling wavefronts.

If a cross-correlation is started or finished part way through a ship's track, the cross-correlation may be biased. Tapering of the cross-correlation amplitudes towards the start and end of the cross-correlation was therefore considered; however, for the given data set and long cross-correlation times, tapering was seen to have little effect.

5.5 Geometric comparisons

Examples of EGFA envelopes with respect to hydrophones other than the outer-most HLA hydrophone, H-52, are shown in Figure 5.9. Due to the steeper grazing angle (of the acoustic paths relative to the horizontal) to the furthest hydrophone, cross-correlations with H-34, a central HLA hydrophone, shown in Figure 5.9(a), do not yield as much information about the surface reflected path as do cross-correlations with H-52, shown in Figure 5.8(d). Figure 5.9(b) reveals that cross-correlations with VLA H-10 show the surface reflected path, at slightly larger times than the dominant direct path, for distances of 0–150 m from the tail end of the HLA; however, the surface path is not as clear as that obtained when correlating with H-52, which is likely due to either the decreased stability in the environment at the shallower depth of H-10, or the increased motion of the VLA hydrophones relative to the HLA hydrophones. The bottom-surface reflected arrival from H-10 to the HLA hydrophones is also observable at a time just after the surface reflected path, but the acausal path from the HLA to H-10 is not observable.

The September 2 EGFA envelopes for SWAMI32 and Shark are shown

5. SHIP DOMINATED AMBIENT NOISE CROSS-CORRELATION

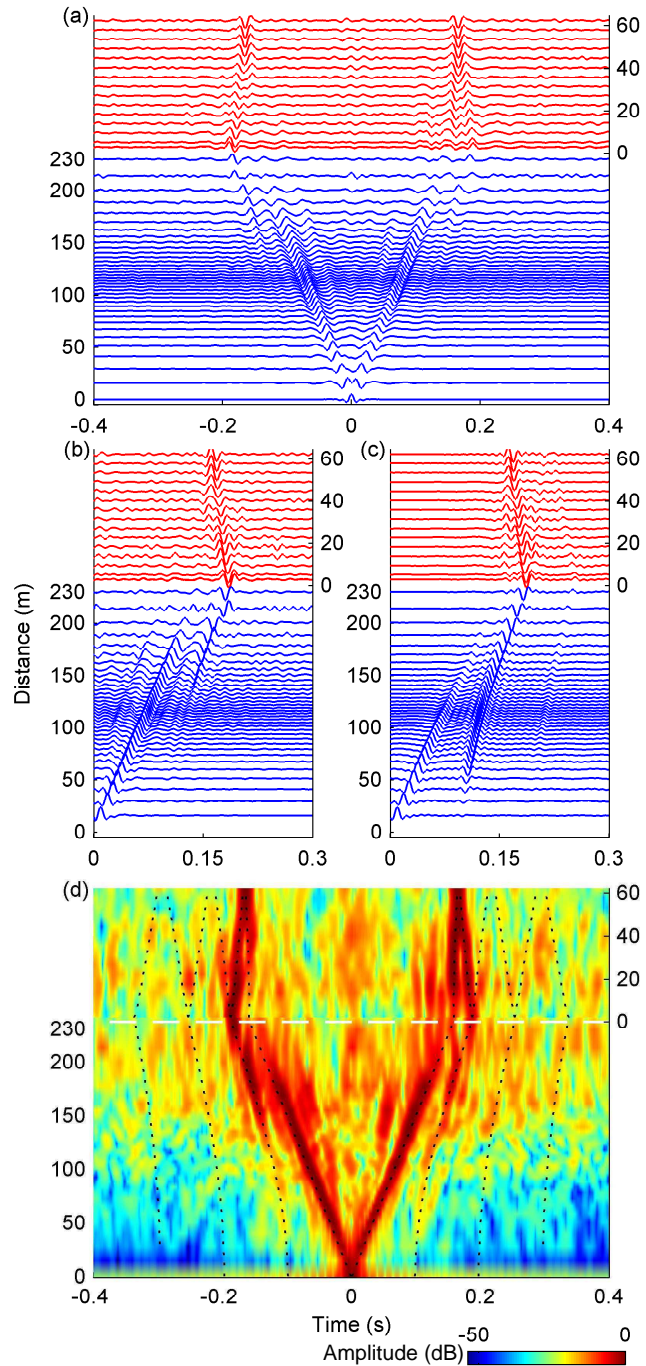


Figure 5.8: September 2 (a) summed cross-correlations and (b) EGFA between H-52 and all other hydrophones. (c) Simulated Green's functions convolved with a 20–100 Hz bandwidth linear source. (d) EGFA envelopes (relative to maximum value) with simulated inter-hydrophone travel times overlaid as dashed lines. Vertical axes format is the same as in Figure 5.5.

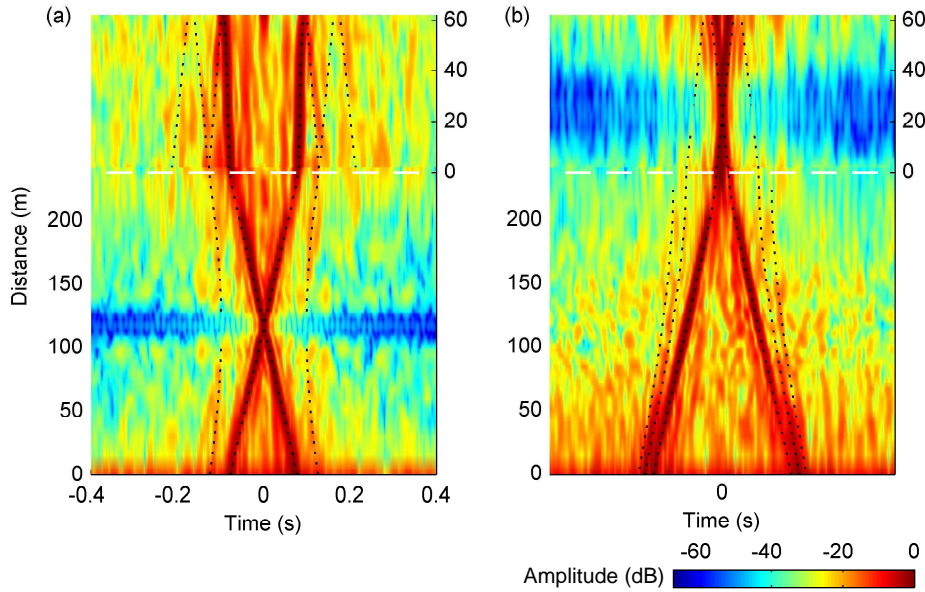


Figure 5.9: September 2 EGFA envelope (dB relative to maximum value) with respect to: (a) H-34, and (a) H-10. Vertical axes are the same as in Figure 5.5.

in Figure 5.10. The SWAMI32 cross-correlations are with respect to H-30 rather than the tail hydrophone due to high noise on the outer two hydrophones. The high noise levels are attributed to channel switching, which is discussed extensively in Chapter 7. Like the SWAMI52 results shown in Figure 5.8(d), the SWAMI32 and Shark array cross-correlations show both the direct and surface reflected paths. All the SWAMI and Shark results in Figures 5.8–5.10 show that although the direct path dominates for more closely spaced hydrophones, the relative amplitude of the surface reflected path increases at greater distances. These relative amplitudes depend upon array geometry, modal distribution of acoustic energy, roughness at the surface and, importantly, the impedance at the seafloor. As such, a relationship between the relative amplitudes of the paths and the critical angle could potentially be determined.

Unlike the tapered spacing of the SWAMI array HLA hydrophones, the Shark HLA hydrophones are evenly spaced at 15 m intervals. Cross-

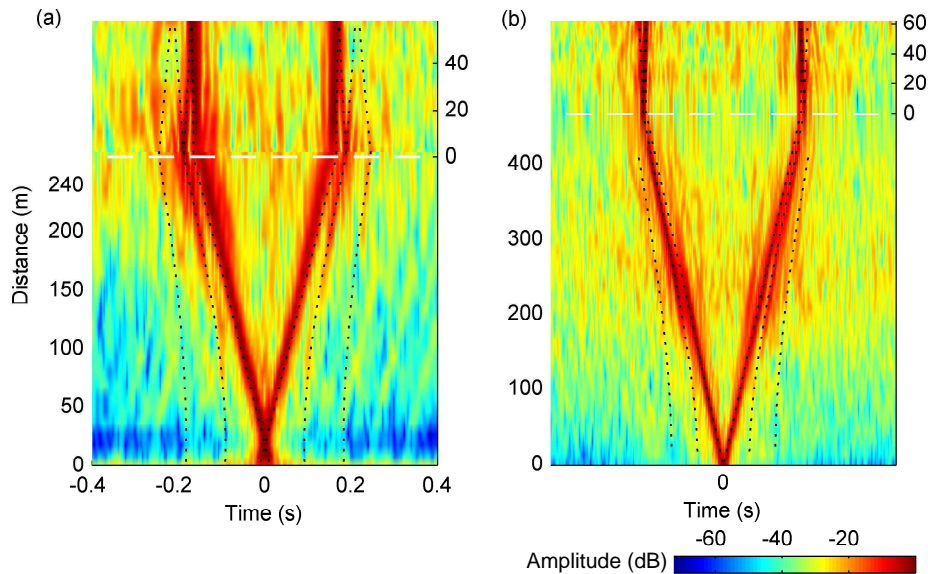


Figure 5.10: September 2 EGFA envelopes (dB relative to maximum amplitude) for (a) SWAMI32, with respect to H-30, and (b) Shark, with respect to H-16. Vertical axes format is the same as in Figure 5.5.

correlations between hydrophone pairs with the same separation distance and direction were compared. The September 2 cross-correlation sums between all HLA pairs separated by 345 m are plotted in Figure 5.11(a). The traces are similar, and all display cross-correlation peaks at approximately ± 0.24 s. The median value of the signals is plotted against a shaded area encompassing the range of all signal values in Figure 5.11(b). A magnified view of part of the signal is provided in Figure 5.11(c) and shows that the signal variation is minimum near the direct path travel time. Summing the cross-correlations of all equally spaced hydrophone pairs should therefore increase the signal-to-noise ratio of the data. The EGFA envelopes between H-52 and all other HLA hydrophones are compared to EGFA envelopes calculated from the sum of the cross-correlations for all pairs at each spacing in Figure 5.11(c)–(d). The overall signal-to-noise ratio is seen to increase when the median cross-correlation is used. Note that the relative amplitudes at some path times not corresponding to inter-hydrophone travel times of the ocean waveguide paths (e.g., $t=0.08$ s, $D=200$ m) do not decrease. These

signals could be from sediment paths or reflections from deeper layers, or they could be non-Green's function arrivals that are due to the noise being azimuthally inhomogeneous.

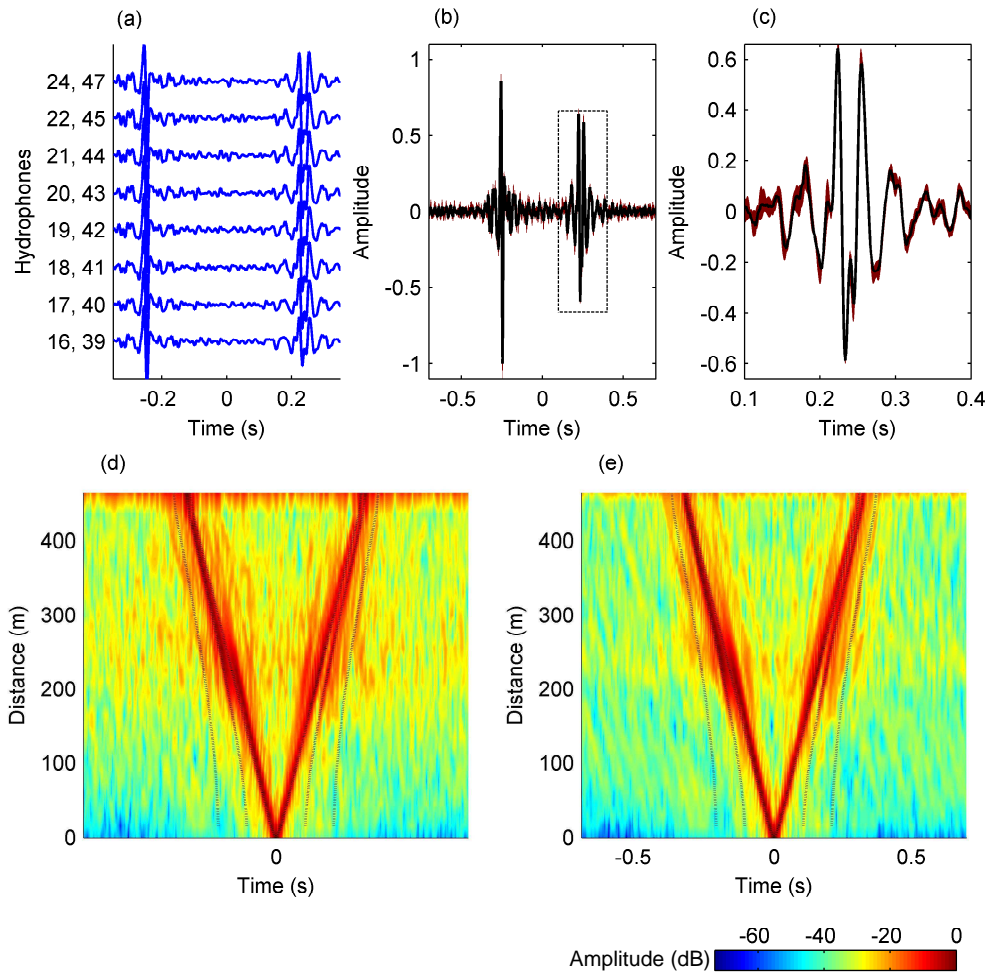


Figure 5.11: (a) Summed cross-correlations over September 2 for Shark hydrophone pairs separated by 345 m. (b) The median cross-correlation from (a) overlies a shaded region between which all values lie. (c) Data from the dashed box in (b) are magnified. EGFA envelopes (dB relative to maximum amplitude) are shown in (d) using cross-correlations between H-52 and all other HLA hydrophones only, and in (e) using the median cross-correlations for all HLA hydrophone pairs.

5.6 Temporal variations

The September 2 data cross-correlations with H-52 were compared with those from adjacent days, and are shown in Figure 5.12. The September 2 data, shown in Figure 5.12(c), peak at the expected direct and surface reflected paths, and exhibit the least background noise. Results from September 1, shown in Figure 5.12(b), are not as clear but are still better than from September 3, shown in Figure 5.12(d), and August 31, shown in Figure 5.12(a), suggesting that the sound field is more diffuse during the storm. Noise from nearby shipping is reduced since most ships retreated from the area for the storm duration, but the overall signal amplitudes are actually higher due to the increase in sea states.

Short time cross-correlations were calculated for data for all three arrays from 0 Z August 31 through 12 Z September 3. SWAMI52 hydrophones H-52 and H-17, SWAMI32 hydrophones H-30 and H-15, and Shark hydrophones H-16 and H-35 were chosen as their separation distances are all similar (between 200 and 285 m). Time segments corresponding to one data file were used for SWAMI52 and SWAMI32 (10:14 and 6:24 min respectively), and quarter file (8:34 min) data segments were used for Shark. These time segments differ as it is easier to use only one rather than parts of two files for a single calculation. The times are all sufficiently short for the study of temporal characteristics. The corresponding EGFA envelopes are plotted as a function of time in Figure 5.13(a)–(c), along with the EGFA envelope of the summed normalised cross-correlations over the 84 hour period.

The EGFA envelope is dominated by discrete sources, as indicated in Figure 5.13(a)–(c) by the presence of the high amplitude peaks that occur throughout the day at times less than the direct inter-hydrophone acoustic travel times. Hydrophone spectrograms from times corresponding to the largest peaks are dominated by a banded structure indicative of ship noise. As an example, spectrograms of 60 seconds duration from 3:36:40 Z August 31 for SWAMI52 H-52 and SWAMI32 H-30 are shown in Figure 5.13(d)–(e). Noise from a large ship, with a primary tonal at just

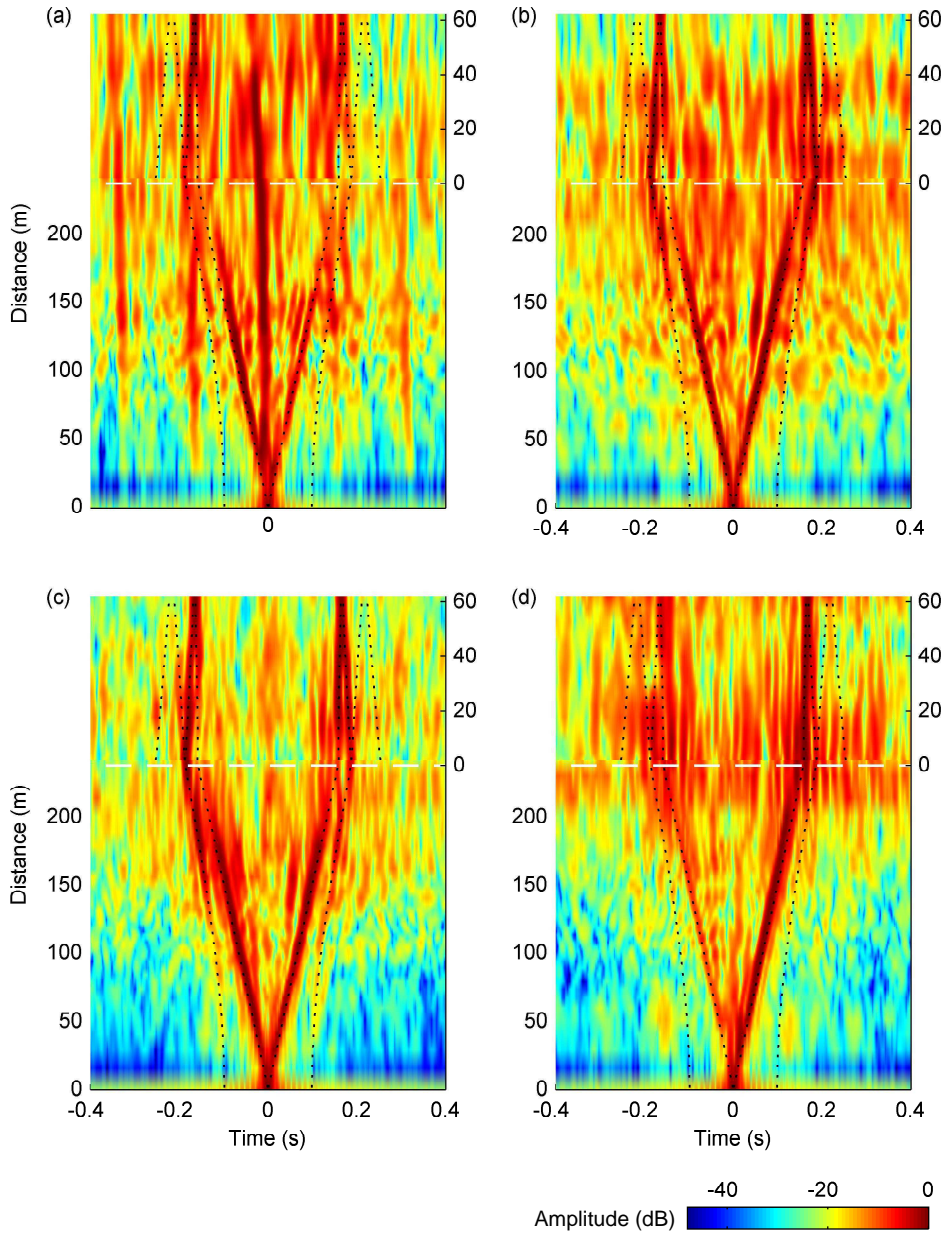


Figure 5.12: EGFA envelope (dB relative to maximum value) with respect to: H-52 for (a) August 31, (b) September 1, (c) September 2, and (d) the first 12 hours of September 3. Vertical axes are the same as in Figure 5.5.

5. SHIP DOMINATED AMBIENT NOISE CROSS-CORRELATION

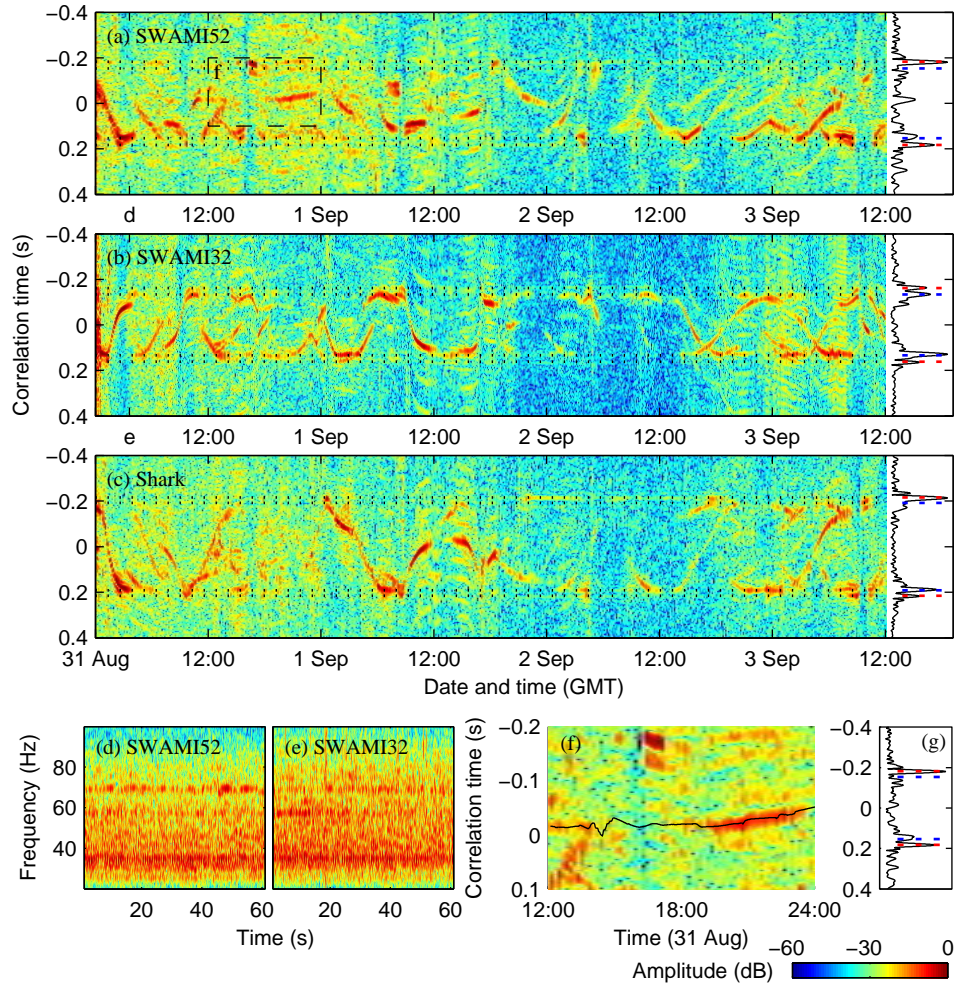


Figure 5.13: EGFA envelope (dB relative to maximum value) for: (a) SWAMI52 H-52 and H-17 (230 m separation), (b) SWAMI32 H-30 and H-15 (200 m separation), and (c) Shark H-16 and H-35 (285 m separation). Simulated direct and surface reflected travel times are faintly overlaid as dashed lines. The envelope of the time gradient of the sum of all cross-correlations, normalised by their peak amplitudes to minimise bias from dominant signals, is shown at the right of each plot. (d)–(e) 20–100 Hz spectrograms (dB relative to maximum value) from 3:36:40 Z August 31 for SWAMI52 H-52 and SWAMI32 H-30 respectively (times denoted on (a) and (b) time axes as ‘d’ and ‘e’). (f) Enlarged view of SWAMI52 EGFA envelope, the boxed area from (a), showing a dominant near-side signal, with calculated travel time difference (black line) from R/V *Oceanus* to the hydrophone pair. (g) The envelope of the time gradient of the sum of all cross-correlations, excluding the period 12–24 Z August 31, for SWAMI52 data. A lower threshold of -60 dB has been applied to all logarithmic scales.

under 40 Hz, dominates both spectrograms. The ship is visible as a peak in the EGFA envelope for all three arrays from 0–4 Z August 31. It was ascertained from the time of the EGFA envelope peak that during this period the ship moved from south-west of the arrays, to north of the arrays. The peak in cross-correlation time due to an individual ship changes as a function of the ship's position and hence the signals from a single ship are apparent as curves of high amplitude when plotted as a function of experimental and cross-correlation times. The 'pattern' of curves that is visible in Figure 5.13(a)–(c) is therefore due to a multitude of ship tracks and is entirely dependent on the types and locations of ships passing through the experimental region. Aliasing of the high amplitude ship signals is apparent (e.g., around 12 Z September 1) in Figure 5.13(a)–(c) as lower amplitude replicas of the main EGFA peak at regularly spaced time intervals surrounding the main EGFA peak.

Towards the end of September 1 and on September 2 the EGFA envelope is more stable, as observed by the main peaks in the EGFA being more consistently closer to the dashed inter-hydrophone travel times, and also by the amplitude and number of smaller peaks in the EGFA being reduced. Fewer shipping tracks are seen, and faint arrivals are observable at the inter-hydrophone travel times. This is during the period of high wind, as shown in Figure 5.1(d), and elevated sea conditions from Tropical Storm Ernesto. The reduction in nearby ships and the increase in wave energy results in a greater proportion of acoustic energy in the ocean at these lower frequencies being from breaking waves and cumulative noise from distant shipping, and therefore the noise field is more diffuse. During this period faint peaks are frequently observed at times corresponding to the simulated surface reflection travel times, such as between 22 Z September 1 and 3 Z September 2 in the acausal signal of Figure 5.13(c).

Although the short term EGFA envelope rarely yields the modelled inter-hydrophone travel time based on the measured sound speed profile throughout the 84 hour period, the EGFA envelopes of the summed cross-

correlations for this period do peak at times near the simulated travel times, as shown at the far right of Figure 5.13(a)–(c). The surface reflected path is particularly strong. This is because the cross-correlation is dominated by nearby ships, and these shorter ranges favour higher grazing angles of the acoustic signals relative to the horizontal.

A strong signal is observed at a cross-correlation time of slightly less than zero for all cross-correlations for August 31 in Figure 5.12(a), suggesting that there is a high amplitude signal from near-broadside (either SW or NE) of the array during that day. A corresponding peak in the summed SWAMI52 EGFA envelope is seen at -0.0175 s at the far right of Figure 5.13(a). The cross-correlations reveal that this peak is a result of signals from 12–14 Z and 18–24 Z on August 31 (see box ‘f’ and Figure 5.13(f)). The Shark and SWAMI32 EGFA envelopes do not show a strong signal at these times. Hence the dominant signal seen in the SWAMI52 data is likely from a source significantly closer to that array than the others. R/V *Oceanus* was located NE of SWAMI52 (in the region 39.25 – 39.28° N, 72.8 – 72.9° W) from 12–24 Z August 31, about 10 km away. This is the closest that R/V *Oceanus* came to any of the arrays during the experiment. R/V *Oceanus* moved slowly in the experimental area and as such is an unusual ship noise source. The expected difference in travel time from this near-broadside location to SWAMI52 matches the short time EGFA envelope peaks, as can be seen in Figure 5.13(f). Thus, the high amplitude spurious signals in Figure 5.12(a) are attributed to R/V *Oceanus*. The amplitude of the anomalous -0.0175 s peak in the EGFA envelope of the summed normalised cross-correlations, shown in the far right of Figure 5.12(a), decreases to the background noise level when the period 12–24 Z August 31 is excluded, as can be seen in Figure 5.12(g).

Figures 5.12 and 5.13 suggest that the observation time period to obtain a stable EGFA envelope depends on the distribution of the noise. Summing over September 2 yields a good approximation, as shown in Figure 5.13(c), but summing over any of the other days, or even summing over the entire

84 hour period gives poorer results due to the increased proportion of directional bias of dominant events in the total received signal. Hence, when specific events dominate the cross-correlations, either data from the times during which they occur should be discarded, or the cross-correlations need to be summed over an even longer period so that the effects of individual events are negligible. At any one time, except during the storm, the cross-correlation is generally dominated by one or two high amplitude events, and eliminating these from the data is difficult. For the case considered here of shipping noise near the coast, the cross-correlations summed over many days or longer could show some directionality, corresponding to preferred shipping routes.

5.7 Conclusion

Cross-correlation of ocean noise in the ship dominated 20–100 Hz frequency band was considered in this chapter. A theoretical stationary-phase based relationship between summed cross-correlations of ship noise using simplifying assumptions was described. The theory showed that the time-derivative of the cross-correlation yields an empirical Green’s function approximation (EGFA), an approximation of an amplitude shaded Green’s function.

EGFAs were determined from data collected during the Shallow Water 2006 (SW06) experiment. Since ship noise is discrete, long cross-correlation periods were required to give sufficient averaging for the emergence of the Green’s function. In this chapter EGFAs were computed over one day, but shorter observation times could potentially be used. The ocean environment is temporally non-stationary. The EGFAs are therefore approximations of ‘average’, rather than instantaneous, Green’s functions. For an appropriate bandwidth, different time and frequency domain normalisation methods yielded similar cross-correlation results. A major reason for this is the spatial averaging of the noise field which occurs when noise from many ship tracks are recorded.

Direct and surface reflected paths between HLA hydrophones, as well as bottom-surface reflected paths between HLA and VLA hydrophones were determined from the EGFA envelopes for three L-shaped arrays, and agreed well with simulated D, S, and B travel times. Averaging the cross-correlations between equi-spaced HLA hydrophone pairs increases the signal-to-noise ratio.

Analysis of temporal variations in the cross-correlations confirmed that the signal is, at any one time, generally dominated by only one or two sources. Cross-correlations obtained from data recorded during Tropical Storm Ernesto were shown to be clearer than those obtained before and after the storm. This is due to a combination of a reduction in high energy discrete sources (most ships left the area during the storm), and an increase in overall sound levels and hence an increase in signal-to-noise ratio. The source of a dominant spurious signal that is observed in the data on two separate non-consecutive days was identified, and its removal was shown to improve the EGFA.

The results obtained here for ambient noise cross-correlation will be compared with those from active source cross-correlation in Chapter 6. The arrival times, but not the amplitudes, of the direct and many of the surface-reflected paths were, overall, well estimated using ambient noise cross-correlation of data recorded during Tropical Storm Ernesto. Two practical applications for the direct path arrival time estimates from the SWAMI32 EGFA data will be detailed in Chapter 7, that is, monitoring and localisation of array elements.

If sub-bottom arrival times could also be estimated then ambient noise cross-correlation could potentially be used to estimate sediment properties such as layer depth and sound speed. One aspect of the future work outlined in Section 8.2.5 discusses how low frequency ambient noise data that will be collected on a recently deployed gas hydrate sea-floor observatory will be cross-correlated in an attempt to extract sub-bottom paths and subsequently monitor a gas hydrate mound.

Chapter 6

Experimental Active Ocean Acoustic Interferometry

Active source ocean acoustic interferometry (OAI) presents a number of advantages over the passive noise OAI technique described in Chapter 5, including the use of higher frequencies, which give sharper arrival peaks, as well as controllability and continuous monitoring. Greater knowledge of the contributing sources also means that more realistic simulated data can be produced. An active set of sources that surrounds the two points of interest could potentially achieve an isotropic source field. Due to the technical complexity of creating such a situation, the characteristics of, and results from, simpler active source configurations are investigated here: a source that is lowered vertically over the depth of the ocean water column, and a source that is towed horizontally along a straight line towards the array at a constant depth. Both of these source tracks are contained within the end-fire plane, which is defined as the plane containing the hydrophone array (i.e., the plane of the page in Figures 6.1 and 6.2(a)). These configurations have been examined theoretically and through simulation in Chapter 3.

Within this chapter cross-correlations between data recorded on hydrophones in an L-shaped array, and obtained using the two active source configurations, source lowering and towed source, are compared and contrasted

with cross-correlations of noise generated during the source lowering event by the ship from which the source was being controlled, and also with cross-correlations from a noise field dominated by shipping. Although recorded simultaneously, data from the active source being lowered, and from the ship during the lowering, can be analysed separately since the active source frequency range was 1200–2900 Hz, which is well above the 20–100 Hz frequency range in which noise generated by the ship dominated.

The active source experiments were performed in seas with a 2–2.5 m swell, residual effects from the passing of Tropical Storm Ernesto the day before. These conditions hindered controllability of the experiments, and therefore the movement of the source was not completely uniform. In addition, the swell would have caused the Green’s function between two points to fluctuate more than usual, which would likely have had detrimental effects on the results obtained. Although the conditions were less than ideal, it was the only opportunity for the experimental work to be completed, since the extensive organisation and high costs associated with at-sea experiments ensures tight schedules, and an entire day of experimental time had already been lost during the storm. The various source configurations that were used are discussed theoretically in Section 6.1, and experimental results for each source type, from cross-correlation of data collected during the SW06 (Shallow Water 2006) sea trials, are compared and explained in Section 6.2.

A significant proportion of the work in this chapter has been submitted for publication in JASA [85].

6.1 Background

Consider the isovelocity waveguide depicted in Figure 6.1. The x , y and z directions are defined as the horizontal axis, the axis in-and-out of the page, and the vertical axis, respectively. Cross-correlation of the signals received

at A and B from a source at S yields

$$C_{AB}(\omega) = \rho_s^2 |S(\omega)|^2 G(\mathbf{r}_A, \mathbf{r}_S) G^*(\mathbf{r}_B, \mathbf{r}_S), \quad (6.1)$$

where ω is frequency, $S(\omega)$ is the source spectrum, ρ_s is the density of the medium, $G(\mathbf{r}_\psi, \mathbf{r}_S)$ is the Green's function between the source S , and receiver ψ , and * denotes the complex conjugate.

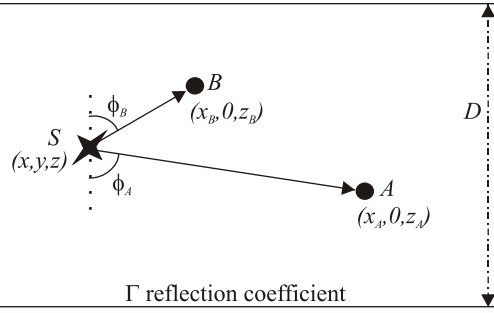


Figure 6.1: Source-receiver geometry and notation. Receivers A and B define the $y = 0$ plane, and source S is located within the waveguide of depth D , but is otherwise unrestricted.

The sum of the cross-correlations over a set of sources is, from Eq. (3.4):

$$C_{AB}(\omega) = |\rho_s S(\omega)|^2 n \int G(\mathbf{r}_A, \mathbf{r}_S) G^*(\mathbf{r}_B, \mathbf{r}_S) dA, \quad (6.2)$$

where n is the number of sources per unit length (line source), area (planar source), or volume (volume source), and the integral is over the source line, plane or volume.

The cross-correlation of data from four source types are considered here:

1. active source lowered vertically in the end-fire plane over the depth of the waveguide, modelled as a vertical line of sources, $\int dA \sim \int dz$;
2. active source towed in the end-fire plane towards the array at a constant depth z , modelled as a horizontal line of sources, $\int dA \sim \int dx$;
3. stationary ship source, modelled as an “extended” point source, $\int dA \sim \int \delta(x, y) dA$; and

4. ship dominated ambient noise field, modelled as a horizontal plane of sources at a shallow depth z , $\int dA \sim \iint dx dy$.

The oscillatory characteristics of the integral in Eq. (6.2) allow it to be solved via the method of stationary phase [68]. The integral is estimated in the neighbourhood of the stationary points, which are the points where the partial derivative of the difference in path lengths to each receiver in the direction of the line integral is equal to zero (i.e., the extrema of the cross-correlation function exponential), and the contributions are then summed over all stationary points. The stationary phase solution to Eq. (6.2), can be derived from Eq. (3.16) for a vertical line of sources in the end-fire plane, source type 1, assuming 3D-wave propagation, as

$$C_{AB}(\omega) = in|S(\omega)|^2 \times \sum_{z_s} \left(\frac{\Gamma^{b_A+b_B} \rho_s^2 G_f(R(z_s))}{\sin \phi_s} \sqrt{\frac{\xi(z_s)c}{-8\pi i \omega}} \right); \quad (6.3)$$

and from Eq. (3.29) for a horizontal line of sources in the end-fire plane, source type 2, as [13, 30]

$$C_{AB}(\omega) = in|S(\omega)|^2 \times \sum_{x_s} \left(\frac{\Gamma^{b_A+b_B} \rho_s^2 G_f(R(x_s))}{\cos \phi_s} \sqrt{\frac{\xi(x_s)c}{-8\pi i \omega}} \right); \quad (6.4)$$

where Γ is the bottom reflection coefficient, b_ψ is the number of bottom reflections for the path to ψ , where $\psi = A$ or B , R is the total distance that a particular wave travels, $G_f(R) = \frac{e^{ikR}}{4\pi R}$ is the 3D Green's function within a homogeneous medium, ϕ_s is the acute angle between the ray path and the vertical (see Figure 6.1), $\xi = \frac{1}{L_B} - \frac{1}{L_A}$, L_ψ is the length of the given path between the source, S , and receiver, ψ , c is the speed of sound in the medium, and z_s and x_s are the stationary points for the vertical and horizontal configurations respectively. The term on the RHS of Eq. (6.4) is termed the phase and amplitude shaded Green's function, because it is the Green's function convolved with phase and amplitude terms. The 3D

Green's function within a homogeneous medium, $G_f(R)$, differs from the true Green's function between A and B , $G(R)$, in that it does not incorporate the path dependent amplitude reduction due to bottom interactions, as explained in Section 3.1. The relationship between them is, from Eq. (3.6),

$$G(R(x_s)) = \Gamma^{b_s} G_f(R(x_s)), \quad (6.5)$$

where b_s is the number of bottom reflections for the arrival between A and B , corresponding to the stationary point x_s .

For a point source, source type 3, Eq. (6.2) simplifies to

$$C_{AB}(\omega) = \frac{|\rho S(\omega)|^2 \Gamma^{b_A+b_B} e^{ik(L_A-L_B)}}{16\pi^2 L_A L_B}. \quad (6.6)$$

In general $L_A - L_B$ is less than the inter-receiver path length (triangle inequality theorem) and therefore arrival times are underestimated. Although the stationary ship source is larger than a point source, the area of integration in Eq. (6.2) is small, and therefore it is not a Green's function estimate. However, if the ship is close to the stationary path it may provide a good approximation.

The structure of the ship noise cross-correlations will only converge to the arrival structure of the Green's function when the cross-correlation time is averaged over several ship tracks, hence the consideration of ship dominated ambient noise, source type 4. For a horizontal plane of sources the stationary phase solution to Eq. (6.2) is, from Eq. (5.5):

$$C_{AB}(\omega) = in|S(\omega)|^2 \sum_{\chi_s} \left(\frac{\Gamma^{b_A+b_B} c \rho_s}{2\omega \cos \phi_s} G_f(R(\chi_s)) \right), \quad (6.7)$$

where χ_s are the horizontal planar stationary points.

The solutions for the line sources, Eq. (6.3) and Eq. (6.4), are of the same form, differing only in the trigonometric function of the acute ray angle ($\frac{1}{\sin \phi_s}$ term for a vertical line source, and $\frac{1}{\cos \phi_s}$ for a horizontal line source), and the locations at which stationarity occurs. The difference in source dimensionality (1D line source distribution versus 2D planar source

distribution) is responsible for the increased complexity of the line source solutions when compared to a 3D Green's function.

For each source configuration the summed cross-correlation produces an amplitude and phase shaded Green's function (i.e., a standard Green's function that is multiplied by amplitude and phase dependent weighting coefficients). The amplitude shading consists of constant (n , ρ_s , c , π , and numeric factors), path dependent ($\Gamma^{b_A+b_B}$, ϕ_s , L_A , and L_B), and frequency dependent (ω and $S(\omega)$) terms.

As explained in Section 3.1.1, the i/ω factor in Eq. (6.7) can be corrected for by using the time-derivative of the cross-correlations [11, 13, 15], and the $i/\sqrt{-i\omega}$ factor in Eq. (6.4) and Eq. (6.3) can be corrected for with a $\pi/2$ phase shift, and a fractional time derivative of 0.5 order [13]. This should yield a result with correct arrival times.

Deconvolution of the source term, $S(\omega)$, from the cross-correlations can present difficulties and hence the Green's functions are instead convolved with the source term, yielding a source shaded Green's function, before comparisons with the phase corrected empirical cross-correlations are made. The constant amplitude shading factors need not be considered since all data are normalised before comparing. Due to their variability, the path dependent amplitude factors are difficult to correct for, and hence correct arrival times but incorrect amplitudes are expected when comparing the phase corrected cross-correlations and the source shaded Green's function.

As discussed in Section 3.1.3, spurious arrivals, defined as peaks in the cross-correlation function at times not corresponding to Green's function path travel times, can occur for each source geometry. For the horizontal planar and line configurations, spurious arrivals will result due to stationary-phase contributions from cross-correlations between waves that initially undergo a surface reflection and ones that do not. For an isovelocity water column, one wave departs at an angle of ϕ from the horizontal, and the other departs at an angle of $-\phi$ [15]. If the depth of the plane of sources is reduced, the spurious peaks converge to the same time delay as

the true Green's function paths; however, they are π out of phase and will therefore result in shading of the Green's function [15]. For the vertical line configuration, spurious arrivals will result when the line integral does not extend to infinity.

6.2 Experiment

6.2.1 Data collection

Acoustic data for OAI were collected on the L-shaped SWAMI32 array, with the geometry shown in Figure 6.2(a). Hydrophones 1–12 (H-1–H-12) constitute the vertical line array (VLA), with H-11 and H-12 co-located, and H-13–H-32 constitute the horizontal line array (HLA).

Data from four source types were recorded:

1. 1200–2900 Hz linear frequency modulated (LFM) source lowered from 9.8–60 m at a constant rate of 1 m/min, at a location 466 m from the VLA, in the end-fire plane (vertical line source: see source lowering geometry and location in Figure 6.2(a)–(b));
2. 1200–2900 Hz LFM source held at 10 m depth towed at 1 knot toward the array in the end-fire plane, from a distance of 1.5 km from the VLA, to a location mid-way between H-16 and H-30 (horizontal line source: see towed source geometry and location in Figure 6.2(a)–(b));
3. 20–100 Hz noise generated by the deployment vessel R/V *Knorr* (location shown in Figure 6.2(a)) during the source lowering experiment; and
4. 20–100 Hz ship dominated ambient noise (horizontal planar source).

A horizontal hyperbolic towed source was theoretically described in Section 3.3. Data from two hyperbolic towed sources were collected during the experiments, but are not analysed in detail here because they showed less

6. EXPERIMENTAL ACTIVE OCEAN ACOUSTIC INTERFEROMETRY

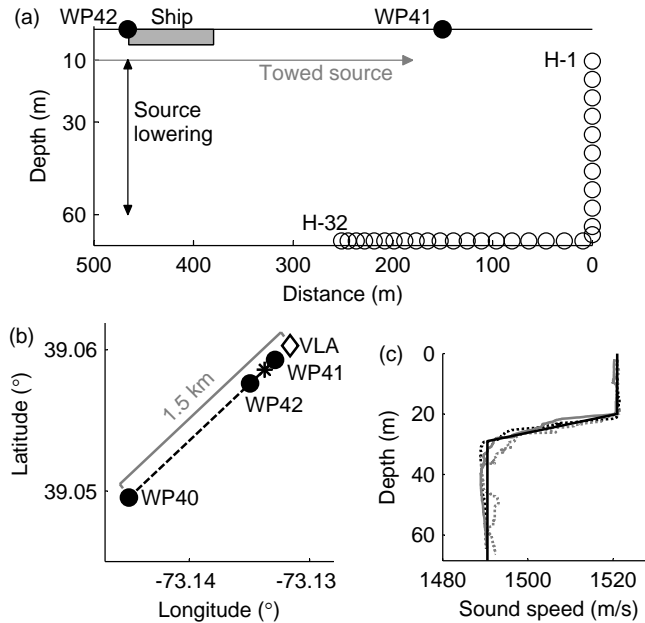


Figure 6.2: (a) Source and receiver geometries: SWAMI32 hydrophones shown as circles, where H-11 and H-12 are collocated at the VLA bottom, and ship location is during source lowering. (b) Plan view of array with VLA labelled, asterisk marking far end of HLA, and source geometries showing where the source is towed from WP40 to WP41, and lowered at WP42. (c) SSPs from CTDs 42–44, shown as black dotted, grey solid and grey dotted lines respectively. Assumed SSP for modelling is overlaid in a black solid line.

resemblance to the acoustic Green’s function than the other two source configurations. Plans for future work involving the hyperbolic source data are described in Section 8.2.3.

The ship dominated noise data, source type 4, were collected during Tropical Storm Ernesto over the entire day of September 2, and data from source types 1–3 were collected on the afternoon of September 3 2006. There was little wind, but there was a residual swell of 2–2.5 m, as well as strong inhomogeneity in the ocean due to the previous day’s storm. These made it difficult to move the active source along the desired tracks. Sound speed profiles (SSPs) were recorded from CTD42 (conductivity, temperature, depth measurement 42) at waypoint 40 (WP40), CTD43 at WP42,

and CTD44 near WP41, before, during, and after the September 3 experiments respectively. These three SSPs are shown in Figure 6.2(c), along with a simpler SSP that is assumed for simulations.

On September 2 several of the SWAMI32 channels switched, as described in detail in Chapter 7. Corrections for this were applied to the relevant data presented here.

6.2.2 Data analysis

Active source data from all hydrophone pairs were bandpass filtered to 1200–2900 Hz, and ship noise data were bandpass filtered to 20–100 Hz. The ship dominated ambient noise data were then one-bit normalised in the time domain (i.e., amplitude was discarded but sign, or phase, of the waveform was retained), and normalised by a smooth version of their amplitude spectra in the frequency domain, as discussed in detail in Section 5.4. The active source and stationary ship data did not require normalisation since variations in the source amplitude and phase characteristics were negligible throughout each experiment.

The preprocessed data were cross-correlated over short time intervals, and then summed over the period of collection for each source type. As specified in Section 6.1, a raw summed cross-correlation (see Eqs. (6.3), (6.4) and 6.7) yields a phase and amplitude shaded Green’s function approximation. The phase shading and frequency dependent components, as explained in Section 6.1, were corrected for by evaluation of the time derivative for source type 4, and by using a $\pi/2$ phase shift and a fractional time derivative for source types 1 and 2. Although source type 3 also has a phase shift, it is geometry dependent, due to the length discrepancy in the exponential of Eq. (6.6), and therefore no correction factors are applied to the stationary ship noise data. Inclusion of the appropriate phase correction is, henceforth, implicit in the term ‘cross-correlation’.

The cross-correlation sum is termed the *empirical Green’s function approximation* (EGFA). The EGFA envelopes of the cross-correlations be-

tween H-30 and all other hydrophones are shown in Figure 6.3 for the four source types in Section 6.2.1. Simulated direct, surface reflected, surface-bottom reflected (VLA only), and surface-bottom-surface reflected path travel times, which were determined using OASES [49], are overlaid as dotted lines for comparison. The simulations use the assumed SSP of Figure 6.2(c) and sediment properties estimated from nearby sediment grab sample data [73]. The ship dominated ambient noise results, shown in Figure 6.3(d), have both causal and acausal components, that is, peaks at positive cross-correlation time corresponding to signals travelling from left to right from the perspective of Figure 6.2(a), as well as peaks at negative time corresponding to signals travelling from right to left. This is because the sound comes from all directions, though only the first 0.05 s of the acausal signal is shown here. The other three configurations, shown in Figure 6.3(a)–(c), have sources travelling in one direction only, from left to right from the perspective of Figure 6.2(a), and therefore produce a one-sided EGFA. The stationary ship EGFA (c) and ship dominated ambient noise EGFA (d) show broader peaks than the active source results, (a) and (b), due to the lower frequencies, 20–100 Hz, of the ship noise compared to the 1200–2900 Hz active source frequencies.

The EGFA envelopes for all source types, as shown in Figure 6.3, exhibit distinct peaks at times agreeing with the simulated direct inter-hydrophone travel times. The times corresponding to these peaks are compared in Figure 6.4. Minimal variations are seen for all HLA hydrophone combinations, though the stationary ship peak times (c) are generally slightly less than the others, which is due to the discrete nature of the source location. No signals from the source pass through the location of the first hydrophone, on their way to the second hydrophone, with a direct path in between.

The variation in the EGFA peak times corresponding to the direct arrivals between the hydrophones are notably larger for the VLA hydrophones. Due to their location, the VLA hydrophones are more sensitive to environmental variations and more susceptible to movement than their HLA

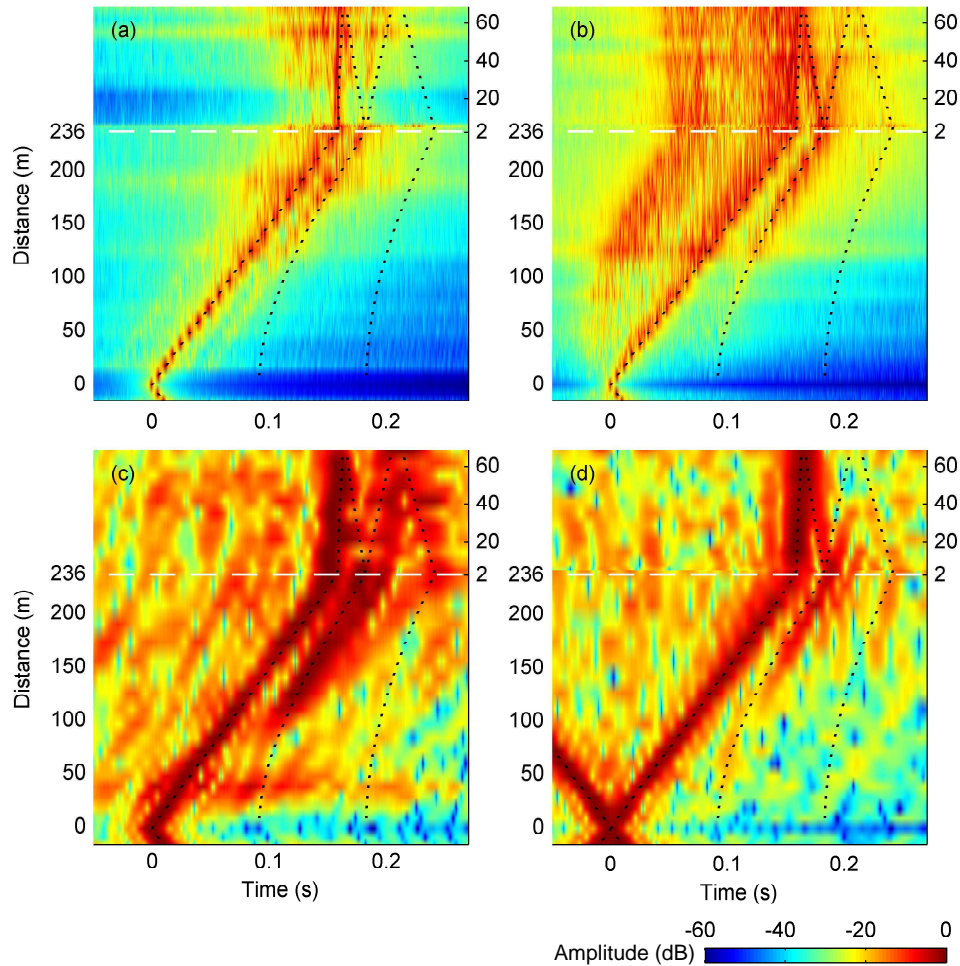


Figure 6.3: EGFA envelopes (dB relative to maximum value) between H-30 and all other hydrophones, overlaid with simulated travel times shown as black dotted lines, for: (a) source lowered vertically from 9.8–60 m, (b) source towed horizontally towards the array, (c) noise generated by R/V *Knorr* during the source lowering, and (d) ship dominated ambient noise. The traces below the dashed white line are from cross-correlations with HLA hydrophones; their distance from H-30 is on the left axis. The upper traces are from cross-correlations with VLA hydrophones; their vertical distance from the seafloor is on the right axis. A lower threshold of -60 dB has been applied to the amplitude.

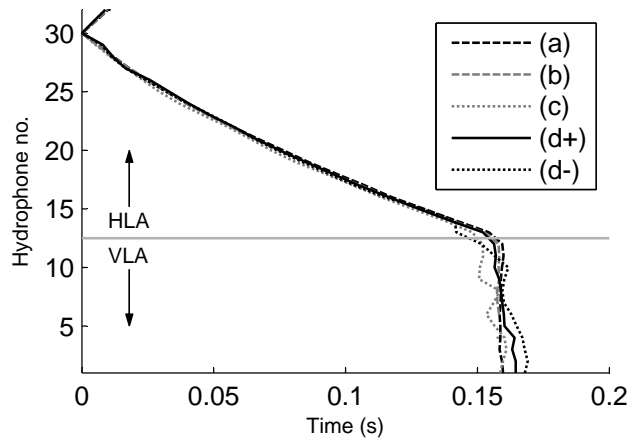


Figure 6.4: Times corresponding to the direct path arrival EGFA envelope peaks of Figure 6.3 as a function of hydrophone number: (a) source lowering, (b) towed source, (c) stationary ship, (d+) causal ship dominated ambient noise, and (d-) acausal ship dominated ambient noise.

counterparts.

The EGFA peaks in Figure 6.3 that correspond to the surface reflected arrivals show more variation than the direct path peaks. The towed source and ship dominated ambient noise results, shown in Figure 6.3(b) and (d) respectively, show a surface reflection peak for all hydrophones more than 40 m from H-30. The source lowering results, shown in Figure 6.3(a), exhibit peaks at slightly early times for hydrophones more than 150 m from H-30. For hydrophones less than 150 m away, peak times diverge from the simulated values. The stationary ship results, shown in Figure 6.3(c), show an arrival peak for HLA hydrophones at ranges greater than 100 m, but the VLA results are not so clear.

The greater the complexity of the acoustic travel paths, the more detrimental any inaccuracies in the simulated environment would have been. For this reason, the EGFA peaks in Figure 6.3 that correspond to the surface-bottom reflected arrivals between H-30 and the VLA hydrophones, show greater variation from the simulated travel times than the EGFA peaks that correspond to the lower order paths.

The amplitudes of the EGFA peaks are greatest, relative to the background noise, for the active source cross-correlations. This is due to high levels of coherently propagating noise which result from the close proximity of the source and the even distribution of the source over the active source line integrals.

In order to more fully explain the EGFA envelopes of Figure 6.3, OAI data for one hydrophone pair, H-30 and H-5, will be examined in detail for each of the four sound sources in the coming sections.

Vertical source lowering

The theoretical vertical line source description in Section 6.1 assumes a set of sources that is uniformly distributed along the line, as explained in Section 3.1. The source was slowly lowered vertically, but was only at one location at any given time. The line source configuration was therefore obtained by cross-correlating data over short time intervals, and summing these cross-correlations. Thus, while the cross-correlations as a function of depth are initially described here, it is the sum of the cross-correlations over all source depths that were used to approximate the EGFA in Figure 6.3(a). The EGFA approximation could instead have been obtained by one single cross-correlation of the data collected from the entire source lowering, but this would have been computationally less efficient, and would not have allowed for analysis of the cross-correlation as a function of source depth.

The geometric set-up of the source lowering, as well as the stationary point travel paths and surface and bottom sources that converge to the stationary points for H-5 and H-30, are shown in Figure 6.5. As explained in Section 3.1.2, a source should ideally be lowered through the water column and sediment, but due to experimental restrictions the source could only be lowered from 9.8–60 m, the deeper limit being approximately 8.5 m above the seafloor.

Cross-correlations of 100 s duration between H-5 and H-30 are shown as a function of source depth for experimental data and data simulated

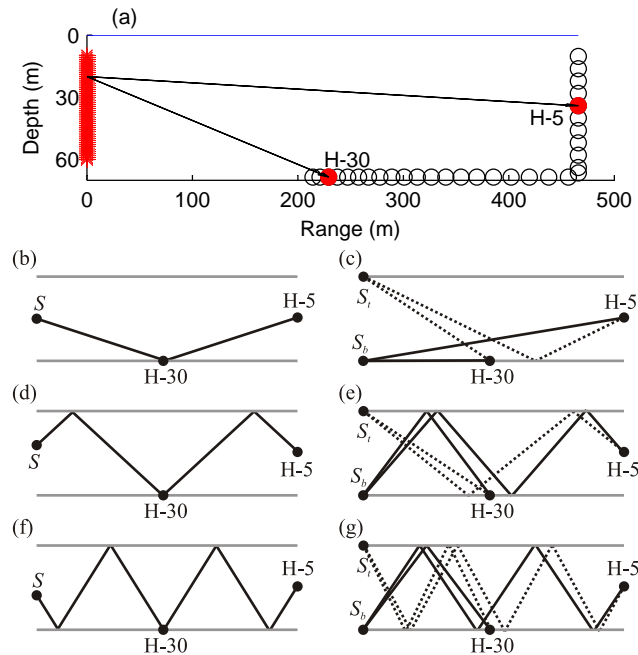


Figure 6.5: Source lowering. (a) Source (far left) is lowered from 9.8–60 m, and signals are recorded on H-5 and H-30, which are shown as solid red circles. (b)–(g) Source-receiver geometry and stationary point paths for (b) direct, (d) surface, and (f) surface-bottom paths between the two hydrophones. (c), (e), and (g) are the surface (S_t) and bottom (S_b) source to receiver paths that converge to the stationary point paths in (b), (d), and (f) respectively.

using OASES in Figure 6.6(a) and Figure 6.6(b)–(c) respectively. Cross-correlation peaks occur at the time differences between paths from the source to each hydrophone. For example, consider the direct path from the source to H-30 and the bottom reflected path to H-5 shown in Figure 6.5(b)–(c). The simulated time differences between these paths for sources at the top or bottom of the waveguide, as shown in Figure 6.5(c), are depicted in Figure 6.6 as the first set of solid red circles at 0.16 s. The curve of cross-correlation peaks connecting these circles, and best seen in Figure 6.6(c), corresponds to the time difference between these paths for each source depth. The time difference increases to a maximum, also called the stationary point, which is depicted as a solid green circle in Figure 6.6(c),

at 40 m depth. This stationary point occurs when the path to the second hydrophone, H-5, passes through the first hydrophone, H-30, as shown in Figure 6.5(b). The two paths have a travel time difference equivalent to the time taken to travel the distance between H-30 and H-5, and therefore correspond to the direct arrival, where arrival refers here, and henceforth, to the travel path between the two hydrophones, not the travel path from the source to one of the hydrophones.

The surface and surface-bottom reflected arrivals between two hydrophones can be analysed in a similar way to the direct arrival just discussed, as shown in Figure 6.5 and marked with solid circles in Figure 6.6.

Consider the four paths that converge as the source location moves towards the surface of the waveguide, to the direct path from the source to H-30, and bottom reflected path from the source to H-5. The convergence point is shown as the first circle, (c) S_t , in Figure 6.6(c). The cross-correlations near this point are reproduced in Figure 6.7, along with schematics of the four paths that converge at this point. The cross-correlations of paths (b) and (e) are in phase with one surface reflection each, and their amplitudes are equal in amplitude at the convergence point. Since the path length difference of (b) increases as the source location moves towards the surface, the path length difference of (e) decreases as the source location moves towards the surface, and their rates of change with source depth are also the same, the cross-correlation peaks due to these combinations transfer smoothly from one path combination to the other at the convergence point, and therefore there is no spurious arrival. A similar argument holds for paths (c) and (d) and all other sets of paths at the waveguide surface and bottom, and therefore no peak should occur at any of these convergence points when the cross-correlations are summed. However, if the amplitude of the surface or bottom reflection coefficient is not unity, there will be discontinuities in the correlation when the total number of surface and bottom reflections of the two converging paths is not identical. Truncation errors due to the non unity reflection coefficients at the

6. EXPERIMENTAL ACTIVE OCEAN ACOUSTIC INTERFEROMETRY

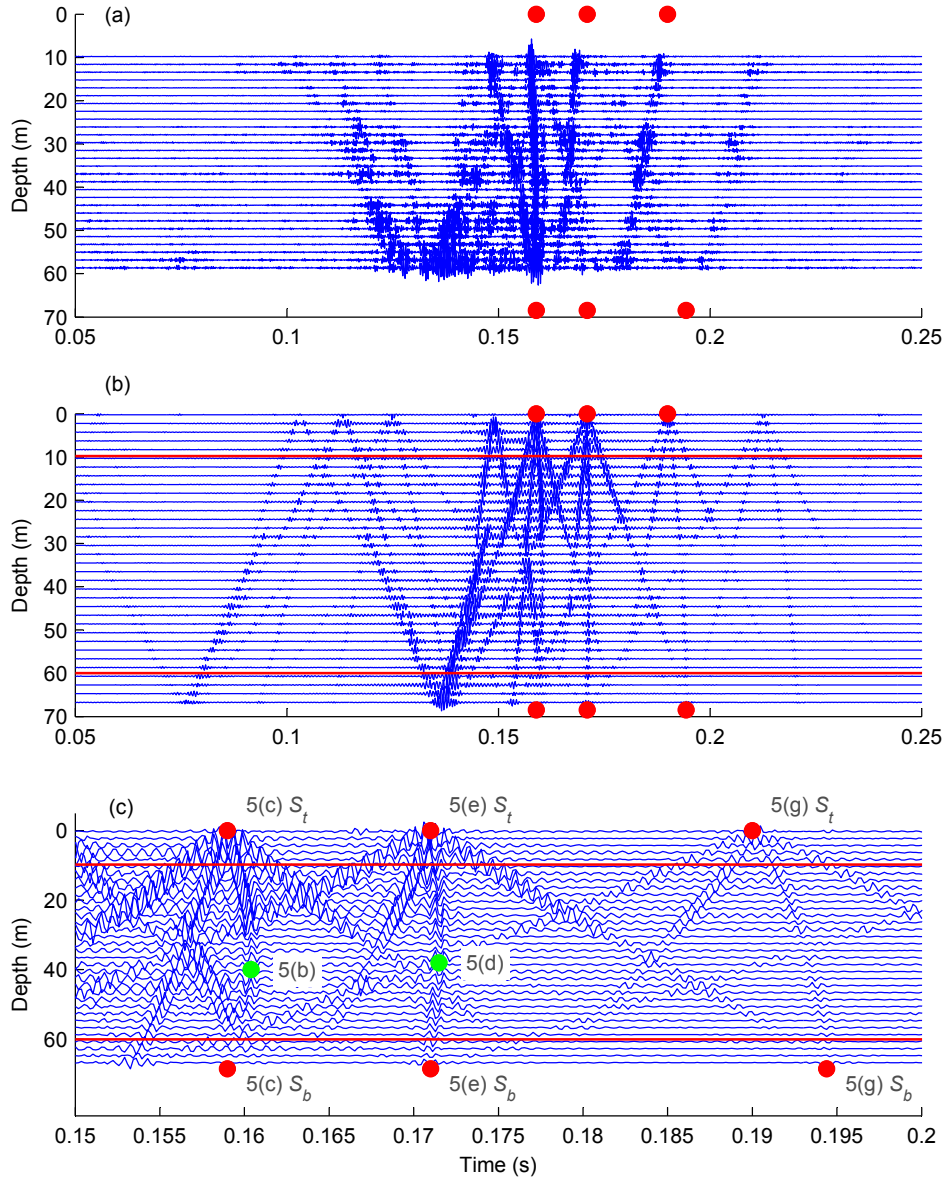


Figure 6.6: Cross-correlated data versus source depth: (a) experimental, (b) simulated, and (c) extract of simulated data. The solid red circles correspond to time differences between the surface and bottom source paths to H-5 and H-30. These paths are shown in Figure 6.5(c), (e) and (g). The solid green circles in (c) correspond to the direct and surface reflection stationary points in Figure 6.5(b) and (d).

bottom of the waveguide are discussed in Section 3.1.2.

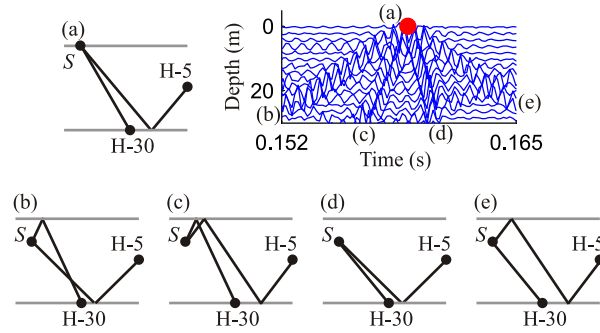


Figure 6.7: View of part of the simulated cross-correlations from Figure 6.6(c), showing the direct path to H-30 and bottom reflected path to H-5 surface convergence point (a), and the four sets of paths that converge to this point as the source moves towards the surface (b)–(e).

The simulated and experimental data of Figure 6.6 differ in three main ways.

1. The experimental data are not as sharp, likely due to 2–2.5 m swell, which caused both the source and waveguide depth to oscillate throughout the lowering event.
2. There are variations in amplitudes for different path combinations, with some path combinations more affected than others. Likely reasons are that the bottom reflection coefficient, or sediment properties, of the simulation are only an estimation, and that due to waves, the surface reflection was not specular. Most paths depend on some power of surface and bottom reflection, as can be seen from Eqs. (6.3–6.7), and higher order paths are more sensitive to these reflection coefficients.
3. Peak times differ slightly, likely due to slight mismatch in sound speed profile and water column depth between the experimental and simulated environments.

The unity surface reflection and the sediment properties that were assumed for the simulations are only approximations. Since the differences between the cross-correlation amplitudes of the simulated and experimental data, item 2, are due mainly to variations in the environment from that assumed, these differences could potentially be used to invert for the actual surface and bottom reflection coefficients.

The cross-correlations were summed over depth. The experimental summed data, ΣC , are compared with both simulated summed data and the source shaded Green's function in Figure 6.8.

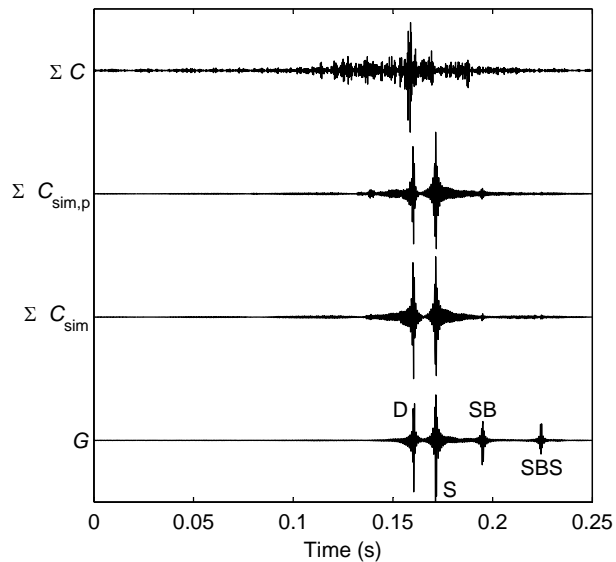


Figure 6.8: The sum of the H-5 and H-30 cross-correlations from the source lowering experiment, ΣC , is compared to the simulated cross-correlations summed from 9.8–60 m, $\Sigma C_{\text{sim,p}}$, the simulated cross-correlations summed over the entire waveguide, ΣC_{sim} , and the simulated source shaded Green's function, G . The Green's function shows direct, D, surface, S, surface-bottom, SB, and surface-bottom-surface, SBS, paths.

The sum of the simulated data over the waveguide, ΣC_{sim} , shows direct, surface reflected, and surface-bottom reflected peaks at correct Green's function, G , time lags in Figure 6.8. The amplitudes are different, as explained in Section 6.1. The significantly smaller amplitude of the surface-

bottom reflected path in $\sum C_{\text{sim}}$ when compared to the Green's function is due to losses from the large number of boundary interactions. The Green's function for this path has only one surface and one bottom reflection, but the two paths that are cross-correlated have 3 surface and 4 bottom reflections between them. This difference in amplitude due to bottom interactions can be seen by comparing Eq. (6.3) and Eq. (6.5). The sum of the simulated data from 9.8–60 m only, $\sum C_{\text{sim,p}}$, has small spurious peaks around 0.14 s, which is earlier than the direct arrival. These are mainly because the cross-correlation arrivals that should converge and cancel with other paths at the seafloor do not converge due to the 8.5 m gap in cross-correlations at the waveguide bottom.

The experimental summed cross-correlation shows peaks at the direct arrival time as well as times slightly less than the surface reflected and surface-bottom reflected arrivals. The main cause of discrepancies in the secondary path peaks can be explained by considering Figure 6.6. The cross-correlations from the travel paths containing the surface and surface-bottom stationary points, the second and third set of solid red circles respectively, are faint in the simulated data, but are not visible in the experimental data, likely due to the source distribution not being completely even, and the environment, in particular the water depth and sound speed profile, constantly changing throughout the source lowering. The summed data are therefore dominated by the stronger peaks from the surface source convergence points that are slightly earlier, that is, the second and third solid red circles at the surface. The amplitude of the surface reflection coefficient is likely less than unity and this causes contributions near the surface convergence points, shown as solid red circles in Figure 6.6.

Horizontal towed source

Following the same reasoning as for the vertical source lowering in Section 6.2.2, to obtain a line source, short time cross-correlations were summed over the time during which the source was towed from WP40 to WP41. The

theory assumes a source that extends out to infinity. Stopping the source suddenly at a finite location can therefore result in spurious arrivals due to the presence of end-effects from cross-correlations at the end point that would cancel with cross-correlations from sources at slightly greater distances if the tow extended further. In order to minimise these end-effects, a tapered cosine window, with length 5% of the total length over which the source was towed, was therefore applied to the amplitude of the cross-correlations from the furthest sources. The H-5 and H-30 100 second long cross-correlations are shown in Figure 6.9 as a function of range for experimental data as well as data simulated using OASES. The direct, surface reflection, and surface-bottom reflection stationary points, which are the points at which the time of arrival of the cross-correlation peaks are local maxima, are difficult to see at this scale, and are therefore circled for clarity. The corresponding stationary point paths are shown in Figure 6.10(a)–(c). The stationary points occur within the first few hundred metres; the cross-correlation peak times increase rapidly to these points, as can be seen in Figure 6.9, and then asymptote towards a far-field fixed value. The towed source configuration has more than one source satisfying each stationary phase condition (i.e., more than one stationary point). The grey circles in Figure 6.10(a)–(c) are higher order source locations that emit signals that pass through the first hydrophone, H-30, and are then received on the second hydrophone, H-5. Since these signals experience more boundary interactions before being received at each hydrophone, their amplitudes are much smaller, and they are therefore not visible in Figure 6.9.

Figure 6.10(d)–(f) are stationary phase geometries where one wave departs at an angle of ϕ from the horizontal, and the other departs at an angle of $-\phi$. These source paths yield spurious arrivals, as explained in Section 6.1, and will be examined in more detail shortly.

The experimental summed cross-correlations over range, $\sum C$, are compared with the simulated summed cross-correlations, $\sum C_{\text{sim}}$, and the simulated source shaded Green's function, G , between H-30 and H-5 in Fig-

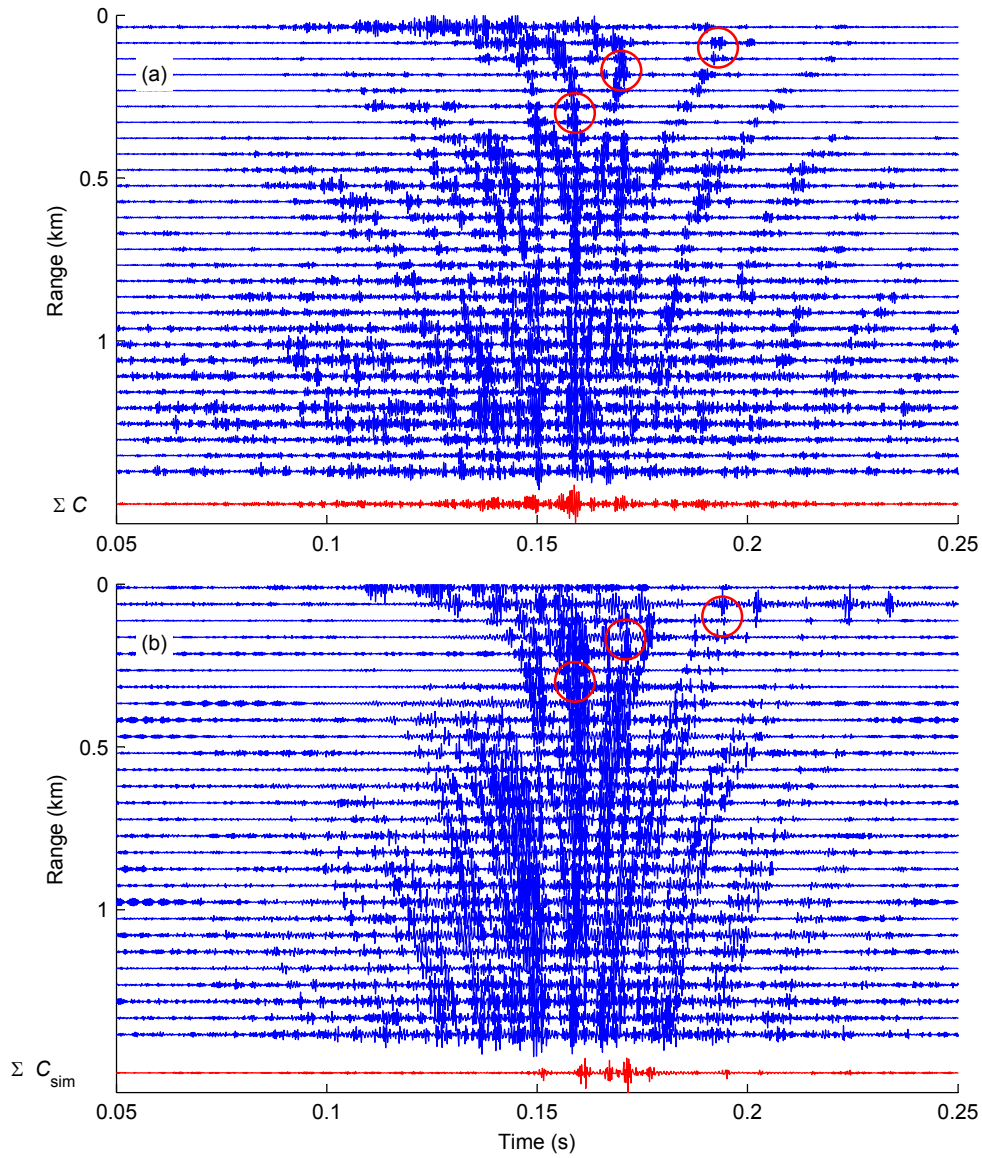


Figure 6.9: Cross-correlated towed source data, (a) experimental and (b) simulated, as a function of range (0–1.4 km) from H-30. The summed cross-correlations, ΣC and ΣC_{sim} respectively, are at the bottom of each plot.

6. EXPERIMENTAL ACTIVE OCEAN ACOUSTIC INTERFEROMETRY

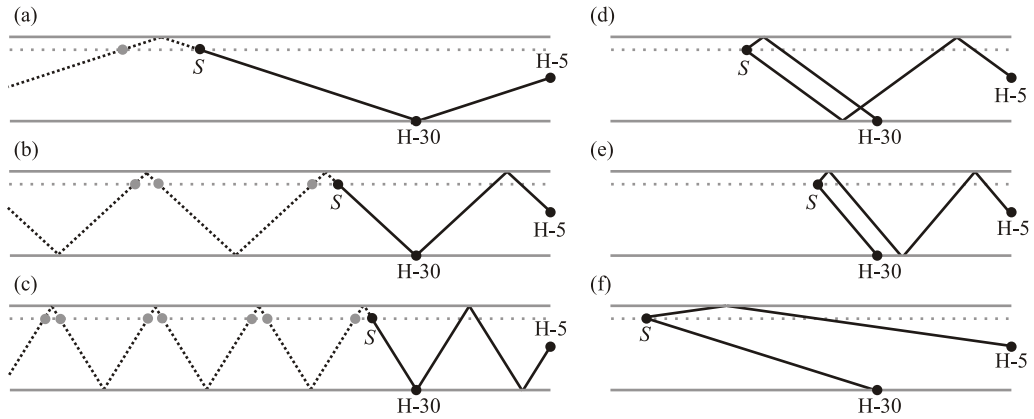


Figure 6.10: Source-receiver geometry and stationary point paths for (a) direct path, (b) surface reflection path, and (c) surface-bottom reflection path. The grey circles represent weaker stationary points. (d)–(f) Stationary phase geometries that yield spurious arrivals.

Figure 6.11. The simulated cross-correlation sum shows direct, D, surface reflected, S, and surface-bottom, SB, arrival peaks at correct lag times. The experimental data have stationary points, circled in Figure 6.9(a), that yield arrival peaks at times slightly less than the simulated direct and surface reflected arrivals, as shown in Figure 6.11. This is likely due to mismatch between the experimental and simulated water depths and sound speed profiles. The experimental summed cross-correlation also has a higher noise background, which is likely due to convergence difficulties near zero range, where the data are very sensitive to the tapering method and the chosen physical end point.

Both the experimental and simulated cross-correlation sums exhibit numerous high amplitude spurious arrivals. For example, consider the two spurious arrivals, X2 and X3, that are visible in the summed simulated cross-correlations shown in Figure 6.11, before and after the surface reflected arrival, S. These spurious arrivals are due to the stationary phase paths shown in Figure 6.10(d)–(e).

The arrivals and stationary points that create these peaks are visible in Figure 6.9(b). Peaks corresponding to the time difference in the direct

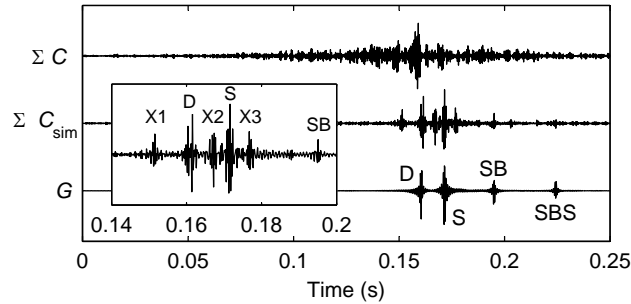


Figure 6.11: Sum of the H-5 and H-30 cross-correlations from the towed source experiment, ΣC , is compared to the simulated summed cross-correlations, ΣC_{sim} , and the simulated source shaded H-5–H-30 Green’s function, G . The Green’s function shows direct, D, surface, S, surface-bottom, SB, and surface-bottom-surface, SBS, paths. An enlarged view of ΣC_{sim} from 0.14–0.2s, showing inter-hydrophone arrivals D, S, and SB, and spurious arrivals X1–X3, is inset.

path to H-30 and the bottom-surface reflected path to H-5, with the surface reflection stationary point at 0.17s circled, are flanked by a set of arrivals at slightly earlier and later times. These spurious arrivals, which are due to the cross-correlation of a wave that initially undergoes a surface reflection with one that does not, have stationary points corresponding to the geometry of Figure 6.10(d) and (e), and are labelled X2 and X3 respectively in the summed cross-correlations of Figure 6.11.

A significant peak, X1, is apparent in both the experimental and simulated cross-correlations at 0.15s, which is prior to the direct path, D, arrival. This spurious arrival is due to a stationary phase contribution from the cross-correlation of the direct path to H-30 and surface reflection to H-5, as shown in Figure 6.10(f). The peak in the simulated and experimental data exist only in this varying SSP environment. Simulated cross-correlations for a 1500 m/s isovelocity waveguide with the same geometry do not show this peak, because such a stationary phase geometry does not exist when considering straight line paths only. The schematic of straight line paths in Figure 6.10(f) comes close to, but does not satisfy, the equal departure angle requirement; the path to H-5 always departs the source at an angle

closer to the horizontal than the path to H-30.

Stationary ship noise

The cross-correlated data from the stationary ship varied little with time, as can be seen in Figure 6.12. Since the source volume is small, the signals received by the hydrophones will be directionally biased, and hence a good estimate of the Green's function is not expected. However, cross-correlation of the ship data during this time does give a multi-path result that looks similar to the Green's function, except that the arrival *structure* does have path dependent inaccuracies. The times tend to be a little early due to the stationary phase path geometries not existing for any of the source locations within the small ship source volume.

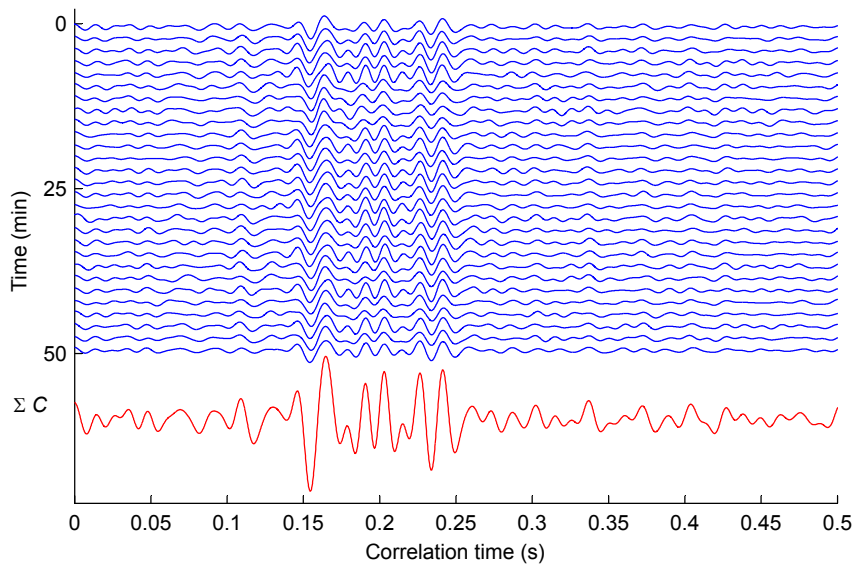


Figure 6.12: Cross-correlations of H-30 and H-5 data from the stationary ship as a function of time during the source lowering event. The sum of the cross-correlations, $\sum C$, is shown underneath.

Ship dominated ambient noise

The structure of ship noise cross-correlations will only converge to that of the true Green's function if either the ship moves along the end-fire direction, or the cross-correlations are averaged over many ship tracks that pass through the end-fire plane. Ship dominated ambient noise, which was investigated in greater depth in Chapter 5, meets the second of these criteria. It was modelled in Section 6.1 as a horizontal planar near-surface source. However, at any one time the signals tend to be dominated by one or two nearby ships, and hence cross-correlation must be performed over a sufficiently long period, here the entire day of September 2, such that several ship tracks that pass through the end-fire plane are included. The cross-correlation function, consisting of many cross-correlations that are each 100 s long, changes continuously throughout the day of September 2, as shown in Figure 6.13. High amplitudes at the direct travel time of ± 0.16 s indicate the presence of a ship near the end-fire plane, whilst high amplitudes at lesser times are contributions from ships closer to broadside (the direction horizontally perpendicular to the array). As an example, from 16–20 Z the acausal cross-correlation has negligible amplitude, suggesting a left-side dominant noise field from the perspective of Figure 6.2(a). From 20–24 Z a high amplitude peak is seen to move from -0.08 to -0.14 s, suggesting the presence of a ship that is moving towards the end-fire plane to the right of the array, again from the perspective of Figure 6.2(a). The causal and acausal direct path signal between H-5 and H-30 only emerges clearly after summation of the noise field over the whole day, $\sum C$, as can be seen in Figure 6.13.

6.3 Conclusion

Empirical Green's function approximations determined from two active source configurations, a vertically lowered source and a horizontally towed source, were compared with EGFAs from a stationary ship at a single end-

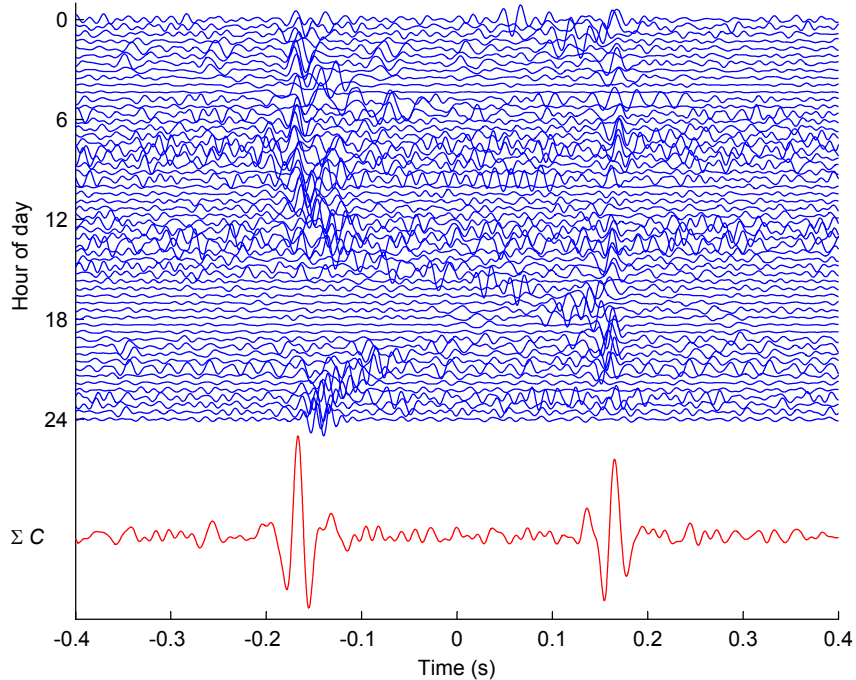


Figure 6.13: Short time cross-correlations of 6 minutes and 24 seconds for H-30 and H-5 ship dominated ambient noise data as a function of time of September 2. The sum of the entire day's cross-correlations, $\sum C$, is shown underneath.

fire location, and EGFAs from a ship dominated ambient noise field. It was shown that the EGFAs from all source configurations yield direct arrival time estimates that match well with the simulated direct arrivals, though the stationary ship arrival times were slightly early. The ability to determine surface reflected arrivals was more variable between techniques, with the towed source and ship dominated ambient noise giving the best results. Due to their greater complexity, the surface-bottom reflected arrivals between H-32 and the VLA hydrophones were not as well determined.

In order to more fully understand how the EGFA evolves for each source configuration, the cross-correlations for one source pair, H-30 and H-5, were analysed as a function of time, and the experimental active source cross-

correlations were compared to those obtained from simulations. The empirical and simulated summed cross-correlations were then compared to the simulated source shaded Green's function, and differences between these were explained with reference to the theory in Chapter 3. The experimental and simulated cross-correlations showed many of the same characteristics.

Although it is the direct path arrivals estimated from the ship dominated ambient noise that will be applied to problems of array monitoring and localisation in Chapter 7, direct arrival times estimated from the EGFAs of active source configurations could also potentially be used for similar purposes.

Chapter 7

Practical Applications of Travel Time Estimates

The experimental results presented in Chapter 5 show that although correct amplitudes are difficult to obtain, the arrival structure of the Green's function between two hydrophones can be accurately approximated from the summed cross-correlation of ship dominated ambient noise. This chapter describes how the inter-hydrophone travel time estimates extracted from this ambient noise ocean acoustic interferometry data can be used for two practical applications:

1. diagnosis of a problem of channel switching on an ocean hydrophone array, and
2. array shape determination.

A significant proportion of the work in this chapter has been accepted for publication in JASA-EL [86].

7.1 Introduction

As a result of Tropical Storm Ernesto, large sea state and wind conditions started to develop during the evening of September 1. All experimental

activities then ceased until September 3. The acoustic arrays remained operative throughout this period. Analysis of experimental data recorded on the 20 hydrophone horizontal portion of SWAMI32 after the storm revealed that several channels in the array had switched.

The term *channel switching* refers to the event where signals from a given hydrophone that were previously recorded on a certain channel, are subsequently recorded on a different channel; *hydrophone* refers to the physical transducer in the array; and *channel* refers to the recording medium where the data from a hydrophone were stored. Hydrophone and channel numbers matched upon deployment of the array, as shown in Figure 7.1(b), but not after the channel switching occurred, as shown in Figure 7.1(c)–(d).

This chapter describes how ambient noise cross-correlation of array data from during the storm are used to diagnose a problem of channel switching that occurred between hydrophone pairs. When channel switching occurs, a set of two given channels begin to record data from a different pair of hydrophones, and hence the inter-hydrophone travel time, determined from cross-correlation of the signals, will change. The estimated travel times, and specifically changes therein, are used to determine on which channel the data from each hydrophone are being recorded at any given time during the day. Consequently, the time and manner in which the channel switching occurs is ascertained.

In addition to the channel switching, it was noticed that travel times of acoustic data recorded on the SWAMI32 array showed inconsistencies with the given array geometry; difference in travel times from any given source to horizontal line array (HLA) hydrophone pairs were consistently less than expected. Cross-correlations of data recorded on SWAMI52 and Shark during this time period yielded travel time estimates that did not vary significantly from that expected for the given geometry. It was therefore hypothesised that the HLA hydrophones were spaced more closely than the *a priori* specifications, most likely due to the HLA not lying in a straight line on the seafloor. Travel times extracted from day long September 2 ambient

noise cross-correlations of SWAMI32 data, with the channel switching taken in to account, are in agreement with this hypothesis.

Direct path travel times are estimated for all hydrophone pairs 12–32 (12 is in the vertical line array (VLA) approximately 2 m above the bottom, and 13–32 form the bottom-mounted HLA). Inter-hydrophone distances are then estimated assuming constant sound speed, which is a valid assumption since hydrophones 12–32 are all at or near the ocean bottom where the SSP does not change significantly. Using the travel times, an inversion for array geometry is performed using the MATLAB® nonlinear least squares algorithm, which uses a subspace trust region method for nonlinear minimisation [87, 88].

7.2 Diagnosis of channel switching

7.2.1 Analysis of recorded data

The SWAMI32 array, the geometry of which is shown in Figure 7.1(a), has a 256-m long horizontal portion consisting of 20 hydrophones with tapered spacing.

Preliminary analysis of acoustic data (see Section 7.2.2) from active sources collected throughout the experiment shows that switching of channels occurred. Since no active source experiments were undertaken during the storm, further details of the switching could not be determined using traditional techniques; however, ambient noise cross-correlations (see Section 7.2.3) show when, and in what manner, the switching occurred.

7.2.2 Active sources

Data from both broadband pulses and combusive [89] sound sources show that before the storm the signals recorded on each channel correspond to the correct hydrophones shown in the *before switching* configuration of Figure 7.1(b). The signal from a broadband 1100–2950 Hz energy pulse,

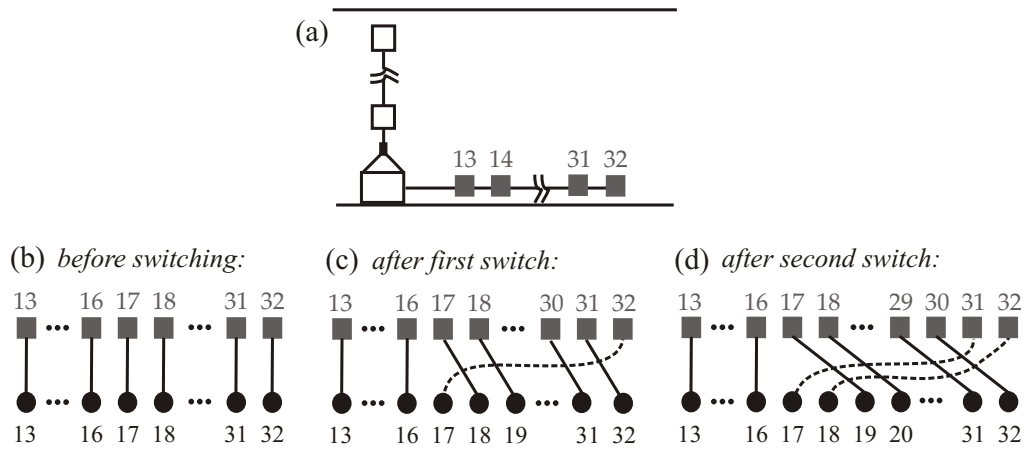


Figure 7.1: (a) Array geometry. (b)–(d) Schematics showing the hydrophone-channel connections: (b) at deployment, (c) after the first switch, and (d) after the second switch.

recorded at 6:04Z on August 31, 21° from the HLA axis, and 1385 m from the closest hydrophone (hydrophone 32), was projected to the on-axis direction. The envelope of the projected signal received by each HLA channel, where channels are directly interchangeable with hydrophone numbers for this case, is shown in Figure 7.2(a). The time of arrival is plotted relative to the first direct arrival. Several reflected arrivals are observable on each channel at times later than the direct. As expected, each arrival is received first by the channel corresponding to the closest hydrophone, channel 32, and the arrival times increase as the channel number decreases. The time interval between arrivals on each channel increases due to tapering of the array spacing.

After the storm, data from both linear frequency modulated (LFM) sweep sources and combustive sound sources indicated that some switching of channels had occurred. The match filtered signal from a 1100–2900 Hz 1-s duration LFM source, held 10 m below the water surface, recorded at 14:40Z on September 3, on-axis with the HLA, and 150 m from the closest hydrophone, is shown in Figure 7.2(b). The signals recorded on each channel no longer correspond to the correct hydrophones. The data from

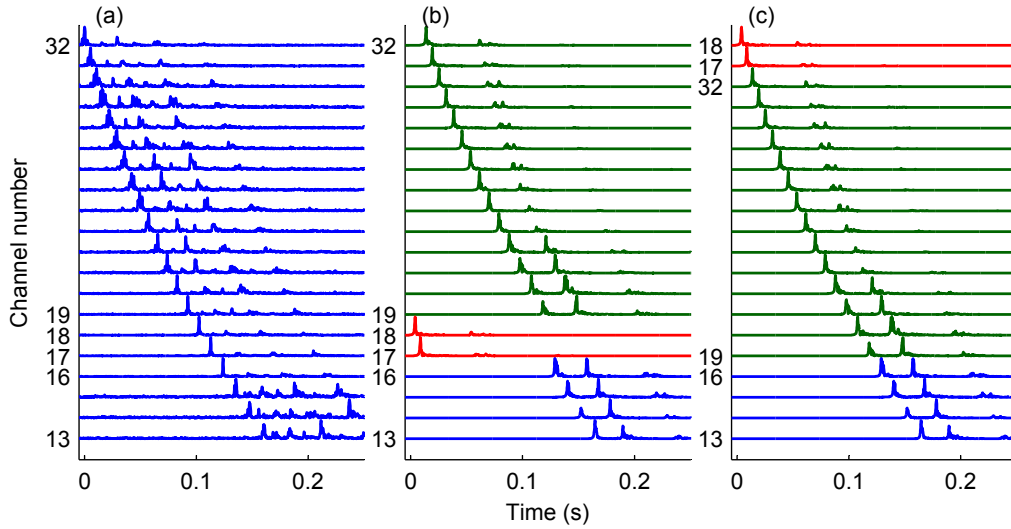


Figure 7.2: Envelope of the signal recorded on each channel from active source testing (a) before the storm at 6:04 Z on August 31, and (b) after the storm at 14:40 Z on September 3. (c) Signal envelope from after the storm with channels re-sorted. Channels 14–15 and 20–31 are unnumbered, but are in order between 13 and 16, and between 19 and 32, respectively.

hydrophones 31 and 32 are recorded on channels 17 and 18 respectively, and the data from hydrophones 17–30 are all recorded 2 channels higher than expected, as shown in Figure 7.1(d). Figure 7.2(c) shows the data after re-sorting the channels so that the data from hydrophones 13 through 32 are in order. The arrival times and the manner in which the shape of the envelope evolves are consistent, which shows that data recorded after switching of the channels occurred are reliable (i.e., acoustic data from each hydrophone are still being recorded).

The channels did not revert to their original configuration, but retained the configuration of Figure 7.1(d) for the remainder of the experiments. It is not known what caused the switches to occur, though possible reasons have been hypothesised. The HLA was connected, through a junction box, to a VLA with a large float at the top (5 m below the sea surface). It is possible that large waves which broke over the VLA float during the storm could have tugged on connector cables, resulting in the propagation

of an impulsive source down the cable and subsequent damage to the cable connections. It is also possible that the problem was not mechanical, but occurred in the electrical systems of the junction box in which the data were stored. Unfortunately these and other hypotheses could not be tested as the array is owned by a non-local organisation and therefore physical access could not be gained.

7.2.3 Ambient noise cross-correlations

As described in Section 2.2.2, the cross-correlation between two hydrophones, denoted A and B , as a function of time delay, τ , is defined as

$$C_{AB}(\tau) = \int_{-\infty}^{\infty} p_A(t)p_B(t + \tau)dt, \quad (7.1)$$

where p is the pressure recorded at each hydrophone, and t is time. It has been shown [8, 15] that the arrival-time structure of the Green's function, G , between hydrophones A and B , defined as the signal which would be received at A given a unit impulsive source at B , can be extracted from the time-derivative of the ocean noise cross-correlation function:

$$\frac{\partial C_{AB}(\tau)}{\partial t} \simeq -[G_{AB}(t) - G_{AB}(-t)]. \quad (7.2)$$

The raw cross-correlation, rather than its time derivative, is often used as an approximation to the Green's function [25, 56], and for a finite bandwidth signal this can be a good approximation, since the cross-correlation and its derivative closely resemble one another. However, if exact arrival times are desired, the cross-correlation time derivative should be employed, as this corrects for the $\pi/2$ phase difference between the raw cross-correlation arrival peak, and that of the Green's function [15].

Ship dominated 20–100 Hz noise was recorded throughout the day that Tropical Storm Ernesto passed through (see Chapter 5). After preprocessing the data, cross-correlation periods of 6:24 min (6 minutes and 24 seconds), which corresponds to the length of a single data file, were used. Since the width of the cross-correlation waveforms are narrow relative to travel times

between receivers, it is sufficient to consider the raw cross-correlations for the purpose of determining which channels are recording data from which hydrophones. Due to the short cross-correlation times, peak amplitudes of the post-processed data were prone to temporal bias from high amplitude directional sources (see Section 5.6). However, even if the source field is not evenly distributed, the time of the cross-correlation peak between the hydrophones increases with distance. Examination of the raw cross-correlations over the entire day revealed three main findings: (a) the channel switching occurred in two steps; (b) a short time period during which each switch occurred can be estimated; and (c) the raw signals, and hence the signal cross-correlations, recorded for a significant time period before and after each switch, exhibit high levels of noise on the higher channels.

Cross-correlations from times prior to and after each switch occurred are shown in Figure 7.3(a)–(d). Figure 7.3(a), which depicts the cross-correlations starting at 7:07:37 Z, shows that the channels are in order, and the cross-correlation peaks correspond to a move-out velocity of approximately 1500 m/s, as expected. The cross-correlations of data starting at 7:14:01 Z are shown in Figure 7.3(b). These show an anomaly in the signal recorded by channel 17. The signal does show a small peak at the expected move-out velocity; however, the major peak occurs at a time of just under 0.2 s, which is the expected cross-correlation time for channel 32. The signals recorded on channels 18 through 32 exhibit major peaks corresponding to those expected for one channel lower than their assigned values. These results suggest that channel 17 switched within the period 7:17 Z \pm 3 min, the relative peak amplitudes indicating that the switch was closer to the start of this time period. Note that the cross-correlations for channels above 17 exhibit high levels of noise. High noise levels were, in fact, observed on channels 18–32 for a two hour period surrounding this time (5:40–7:40 Z), suggesting that the channel switching and the increase in noise are linked. The hydrophone-channel connections after this first switch are shown in Figure 7.1(c).

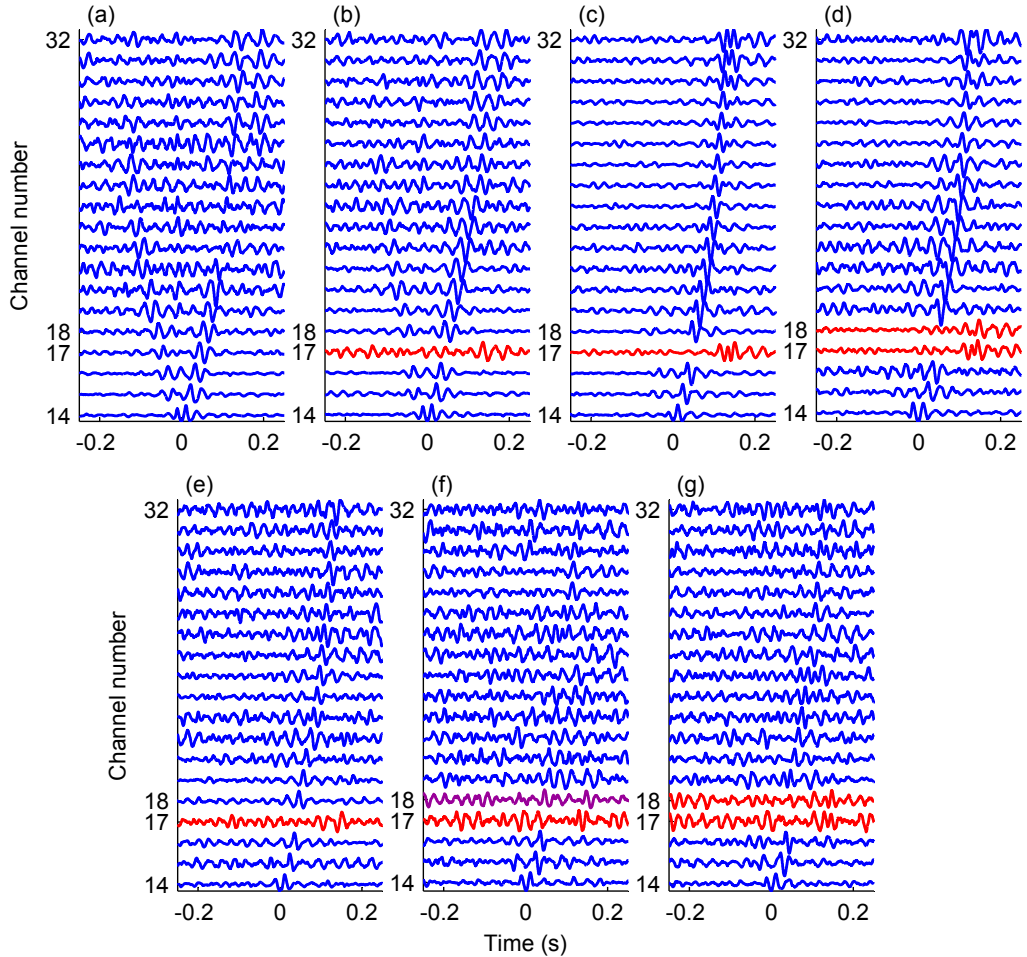


Figure 7.3: Short time cross-correlations (6:24 min) between channel 13 (first HLA hydrophone) and all other channels from the time period surrounding the first switch (a) 7:07:37 Z and (b) 7:14:01 Z, and from the time period surrounding the second switch (c) 12:08:40 Z and (d) 12:15:05 Z. (e)–(g) 20 s long cross-correlations at 12:14 Z for times (e) 20–40 s, (f) 30–50 s, and (g) 40–60 s.

Results of cross-correlation of data starting at 12:08:40 Z are shown in Figure 7.3(c). Channel 17 is still the only channel to have switched. Cross-correlations of data immediately following this, starting at 12:15:05 Z are shown in Figure 7.3(d). These cross-correlations suggest that channel 18 has also switched. Now channels 17 and 18 are recording data from hydrophones 31 and 32, and channels 19–32 are recording data from two hydrophones less than their number. This configuration matches the ‘after switching’ description of Section 7.2.2 that is depicted graphically in Figure 7.1(d) and Figure 7.2(b). Cross-correlations with higher numbered channels exhibit less noise than during the first switch, and high noise levels were only observed for a few minutes around the time of the second switch.

Cross-correlations over shorter time periods were employed to narrow down the time window during which the second switch occurred. Cross-correlations of 20-s duration were calculated from 12:08:40–12:21:29 Z. Three results from the minute of 12:14 Z are shown in Figure 7.3(e)–(g): (e) 20–40 s, (f) 30–50 s, and (g) 40–60 s. Due to the shorter duration of the cross-correlation time, the cross-correlations exhibit high noise levels; however the peak arrivals can still be observed. The first cross-correlation, Figure 7.3(e), suggests that channel 17 has switched but 18 has not. The second cross-correlation, Figure 7.3(f), is the least clear, but suggests that the switch occurs during this time period, since both the true and delayed arrival are seen. The third cross-correlation, Figure 7.3(g), also exhibits the true and delayed arrival; however, the delayed peak dominates, suggesting that the switch occurred closer to the start of the cross-correlation period. The likely time interval during which the second channel switching occurred is thus 12:14:45 Z \pm 5 s.

Once the switch times had been determined, data from the entire day of September 2 were correlated in three time segments: (a) immediately before either switch, (b) after the first switch but before the second switch, and (c) immediately after the second switch. The channels were re-sorted so that the data from hydrophones 13 through 32 were in order, and then

plotted as a function of distance from hydrophone 13 in Figure 7.4(a)–(c). The cross-correlation peaks are seen to increase linearly in time with distance along the array, which is in agreement with the results previously described. The noise levels are lower than those in Figure 7.3 due to the longer cross-correlation periods. The envelopes of the time-derivatives of the cross-correlation functions, which, as previously mentioned, relate to the arrival times between hydrophones, are shown in Figure 7.4(d)–(f), corresponding to data in Figure 7.4(a)–(c) respectively. The simulated travel times between hydrophones, which were determined using OASES [49], are also shown. The envelope peaks are in agreement with the direct arrival, and also with the surface reflected arrival at greater distances. The surface reflected arrival is not seen at closer distances due to the steeper grazing angles, which are accompanied by greater bottom loss.

Figures 7.3 and 7.4 show only the cross-correlations between channel 13 and other channels. Comparisons between all channels can be made by considering the peak of the envelope of the time-derivative of the cross-correlation function, which, as previously mentioned, corresponds to the arrival times between hydrophones when the noise sound field is isotropic.

The arrival time corresponding to the envelope peak of the noise cross-correlation time-derivative is plotted for all channel pairs in Figure 7.5 for three 6:24 min periods at (a) 2:20 Z, (b) 10:55 Z, and (c) 23:15 Z. These correspond to time periods well before the first switch occurred, in between when the two switches occurred, and after the second switch occurred. During the high noise level time periods surrounding the switch times, a clear peak in the gradient envelope was difficult to obtain, and therefore the time periods used here are well away from the switch times. The correlation times of Figure 7.5 give additional support to the findings that the channel switching occurred in two steps. Figure 7.5(c) shows peak times that are less than those shown for (a) and (b). This suggests that the noise field at 23:15 Z is dominated by off-axis directional energy in the data (see Section 5.6). However, as mentioned in Section 7.2.3, even if the source field

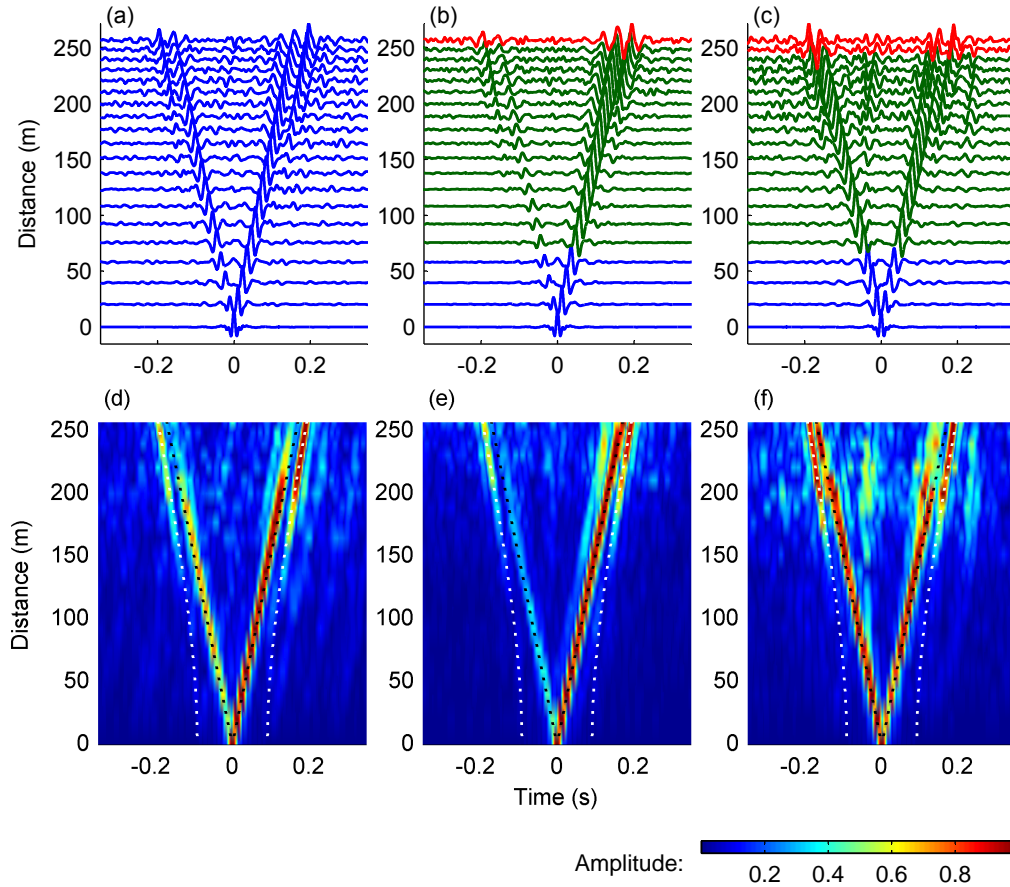


Figure 7.4: (a)–(c) Cross-correlations between channel 13, the first HLA hydrophone, and all other channels after re-sorting the channels, plotted as a function of distance from hydrophone 13: (a) before, (b) between, and (c) after the switches. (d)–(f) Normalised envelopes of the cross-correlation function time-derivatives, with simulated direct (black dotted lines) and surface reflected path travel times (white dotted lines): (d) before, (e) between, and (f) after the switches.

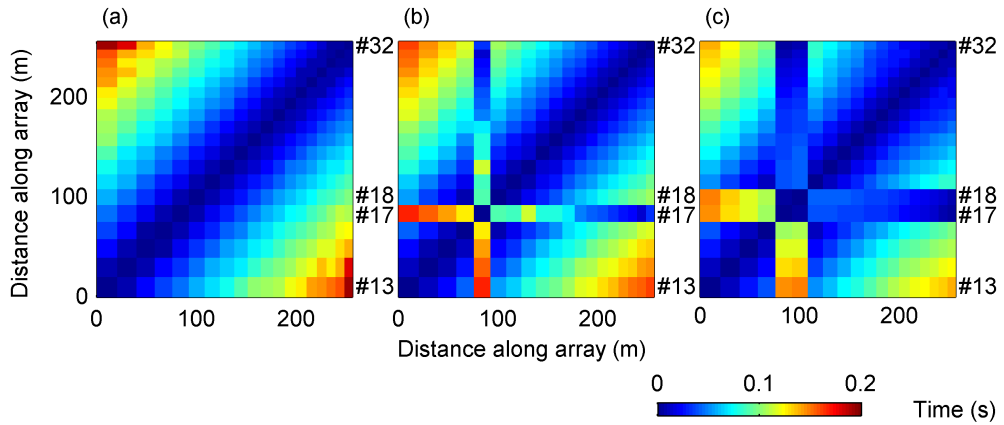


Figure 7.5: Arrival time as a function of distance from the first HLA element (hydrophone 13), from (a) before the first switch at 2:20 Z, (b) after one channel has switched at 10:55 Z, and (c) after both channels have switched at 23:15 Z.

is not evenly distributed, the time of the cross-correlation peak between the hydrophones increases with distance, and therefore only the relative times are important.

7.2.4 Conclusion

Results from active source experiments near the SWAMI32 array prior to and after the day Tropical Storm Ernesto passed through the region showed that some channels had switched during the storm.

Ambient noise cross-correlation of data from September 2 was successfully employed to determine more information about the nature of the channel switching. The cross-correlation analysis suggested that the switching occurred in two distinct stages. The change that occurred at each stage was identical; the channel that was recording the data of hydrophone 17 started recording data from hydrophone 32, and the channels recording data from hydrophones 18 through 32 all moved down one hydrophone. The inferred time intervals during which each switch happened were narrowed down to the periods $7:17\text{ Z} \pm 3\text{ min}$ and $12:14:45\text{ Z} \pm 5\text{ s}$. Elevated noise levels were ob-

served on each channel for a significant time period surrounding each switch. The noise levels were especially high during the first switch, making it difficult to narrow down the time of the switch to as small a time window as was obtained for the second switch. Longer time period cross-correlations from before, between, and after the switches occurred, supported the findings. With the channels re-sorted to the correct hydrophones, the cross-correlation function time-derivative envelopes showed accurate arrival time structure.

7.3 Array shape estimation

Estimation of array shape from travel times and other acoustic data has previously been performed using discrete sources [90–92]. Either an active source or ship noise at approximately known locations is used. If exact source locations are not known, the inversion algorithm can invert for both source and receiver positions. Inputs for the inversions generally consist of source-receiver travel times, *a priori* estimates of the source and receiver geometry, and estimated errors in travel times and geometry, as well as other assumptions such as the array elements being able to be approximated by a smooth function.

Sabra *et al.* [27] developed a 2 dimensional algorithm (all receivers must be located on the same horizontal plane, allowing for an isovelocity assumption) for array element self-localisation from ambient noise cross-correlations. Their methods were experimentally shown to be effective for HLA hydrophone localisation, and as such, form a basis for the methodology presented here.

All the HLA elements as well as the lowest VLA element are considered here. The VLA element is included so that the location of the HLA relative to the VLA can be estimated also. Velocity changes near the bottom of the water column are negligible and therefore the isovelocity assumption remains valid.

7.3.1 Inter-hydrophone travel times

Correlations of SWAMI32 20–100 Hz September 2 data were performed following the methodology of Chapter 5. Travel times, $T_{i,j}$, between hydrophones i and j were then estimated as the peak of the empirical Green’s function approximation envelope.

7.3.2 Inversion algorithm for array element localisation

The fundamentals of a generic inversion process are included in Appendix C. The array element inversion process presented here attempts to determine an array geometry with inter-hydrophone travel times that best match the measured travel time estimates.

The bottom of the VLA is chosen as the origin, and the 20 HLA elements, which are all assumed to be at a constant depth, are parameterised in 2D by their distance and azimuth from the first element. The VLA element is parameterised by its height from the seafloor.

The model vector of unknown parameters is

$$\mathbf{m} = [h_1, d_2, \dots, d_M, \theta_2, \theta_3, \dots, \theta_{M-1}]^T, \quad (7.3)$$

where $M = 21$ is the number of elements in the array, h_1 is the height of the VLA hydrophone above the seafloor, d_j is the distance from the origin to element j , and θ_j is the azimuth relative to the two ends of the array (i.e., $\theta_M = 0$). The inversion therefore seeks to estimate $2M - 2$ unknowns.

The observed data vector:

$$\mathbf{T} = [T_{1,2}, T_{1,3}, \dots, T_{1,M}, T_{2,3}, \dots, T_{M-1,M}]^T, \quad (7.4)$$

consists of $M(M - 1)/2$ terms.

The array is *a priori* assumed to be straight. The *a priori* estimate of the unknown parameters is therefore $\mathbf{m}_{\text{ap}} = [l_2, \dots, l_M, 0, \dots, 0, c_0]^T$, where l_j is the pre-experiment measured hydrophone separation.

The inversion seeks to minimise the difference between the measured travel times and those computed from the model vector, whilst simulta-

neously ensuring that the resulting hydrophone locations lie on a smooth spline.

The computed travel times are

$$\mathbf{T}_{\text{cal}} = \left[\frac{\sqrt{|d_2 e^{i\theta_2}| + h_1^2}}{c_0}, \dots, \frac{\sqrt{|d_k e^{i\theta_2}| + h_1^2}}{c_0}, \dots, \frac{\sqrt{|d_M e^{i\theta_2}| + h_1^2}}{c_0}, \right. \quad (7.5)$$

$$\left. \frac{|d_3 e^{i\theta_k} - d_2 e^{i\theta_j}|}{c_0}, \dots, \frac{|d_k e^{i\theta_k} - d_j e^{i\theta_j}|}{c_0}, \dots, \frac{|d_M e^{i\theta_M} - d_{M-1} e^{i\theta_{M-1}}|}{c_0} \right]^T. \quad (7.6)$$

The travel time differences should be weighted by the inverse of the uncertainties of the measured times. This is done by pre-multiplication with the diagonal regularisation matrix:

$$\mathbf{W}_1 = \text{diag}[w_{1,2}, w_{1,3}, \dots, w_{1,M}, w_{2,3}, \dots, w_{M-1,M}], \quad (7.7)$$

where $w_{j,k}$ are uncertainty weightings for each observation data. If the uncertainty is assumed to be a constant number of samples independent of the hydrophone pair, then the difference between the observed travel times, \mathbf{T} , and the computed travel times, \mathbf{T}_{cal} , should be equally uncertain regardless of hydrophone pair. Unity regularisation weighting was therefore used.

The first objective function to be minimised is

$$\Phi_1 = [\mathbf{W}_1(\mathbf{T} - \mathbf{T}_{\text{cal}})]^T [\mathbf{W}_1(\mathbf{T} - \mathbf{T}_{\text{cal}})] \quad (7.8)$$

$$= [(\mathbf{T} - \mathbf{T}_{\text{cal}})]^T [(\mathbf{T} - \mathbf{T}_{\text{cal}})]. \quad (7.9)$$

The second consideration of the inversion is the shape of the array. The *a priori* assumption is that the array is straight. The inversion therefore seeks to minimise the difference in azimuth between straight lines connecting successive elements.

The change in azimuth vector between the lines connecting two successive elements is

$$\Delta\Theta = [\Delta\theta_2, \dots, \Delta\theta_j, \dots, \Delta\theta_{M-1}]^T, \quad (7.10)$$

where

$$\Delta\theta_j = \text{phase}(d_{j+1}e^{i\theta_{j+1}} - d_j e^{i\theta_j}) - \text{phase}(d_j e^{i\theta_j} - d_{j-1}e^{i\theta_{j-1}}). \quad (7.11)$$

Unity regularisation weighting is applied. The smoothness objective function is therefore

$$\Phi_2 = [\Delta\Theta]^T[\Delta\Theta]. \quad (7.12)$$

The objective function to be minimised is the weighted sum of Φ_1 and Φ_2 :

$$\Phi = \Phi_1 + \alpha\Phi_2 = [(\mathbf{T} - \mathbf{T}_{\text{cal}})]^T[(\mathbf{T} - \mathbf{T}_{\text{cal}})] + \alpha[\Delta\Theta]^T[\Delta\Theta], \quad (7.13)$$

where α is the Lagrange multiplier that governs the relative importance of the observed travel times and the array smoothing.

The array geometry is estimated as that which minimises the objective function, Φ .

7.3.3 Application to data

The array element localisation algorithm was applied to the travel times obtained from the JD245 ambient noise cross-correlations. Minimisation of the objective function was achieved using the MATLAB® nonlinear least squares algorithm, which uses a subspace trust region method for nonlinear minimisation [87, 88].

Since the least-squares algorithm attempts to minimise all travel time differences, it can be susceptible to bias from outliers. The six largest values were therefore rejected for each calculation of the objective function (stability was checked and results using rejection of 5–20 largest values showed negligible variation).

Lower and upper limits on inter-element spacing were set to half and twice the *a priori* values. The large upper bound was used because inversion results yielding distances greater than the *a priori* data would have suggested a problem with either the data or the algorithm. The distances calculated from the inversion were; however, consistently about 5% less than the *a priori* values, which is consistent with the expectation that the hydrophones were spaced more closely.

The inverted element location results are show in Figure 7.6, along with the *a priori* locations. The *a posteriori* geometry supports the original

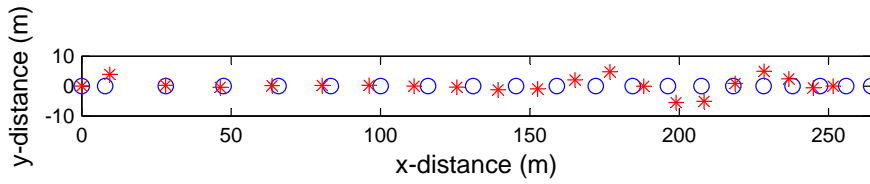


Figure 7.6: Array element locations: *a priori* (circles) and *a posteriori* results from non-linear least squares travel-time inversion (asterisks).

hypothesis that the HLA was not lying in a straight line. Results using estimates of the unknown parameters \mathbf{m}_{ap} that are different to the *a priori* geometry converge to the same *a posteriori* geometry. The *a posteriori* geometry results were observed to match travel times from all active sources at known locations near the array better than the *a priori* straight line geometry.

7.3.4 Conclusion

An inversion algorithm for array element localisation, that used inter-hydrophone travel times estimated from ship dominated ambient noise cross-correlation, was successfully applied to SWAMI32 hydrophone data. The curved *a posteriori* array shape matched travel times from active sources at known locations better than the *a priori* shape, supporting the original hypothesis that the array was not lying in a straight line

Chapter 8

Conclusion

Knowledge of the ocean acoustic Green's function can be used to determine information about the ocean environment through which acoustic transmission between two points takes place. There exists limited prior literature that addresses ocean acoustic interferometry, that is, Green's function approximation from cross-correlation of sound in the ocean. The work in this thesis aimed to further the understanding of ocean acoustic interferometry in a shallow water oceanic waveguide.

8.1 Summary of thesis findings

This thesis focussed upon ocean acoustic interferometry using two source types: active sources, and ship dominated ambient noise. Theoretical descriptions, simulated and experimental results (using data collected on the outer New Jersey Shelf during the Shallow Water 2006 sea trials), as well as two practical applications of ocean acoustic interferometry, were presented.

A stationary phase argument was used to theoretically describe the relationship between the summed cross-correlations from a line of active sources, and the Green's function between two hydrophones. Three active source configurations were considered: vertical and horizontal line sources, located in the same vertical plane as two hydrophones; and a horizontal

8. CONCLUSION

hyperbolic source with its asymptote at a location horizontally midway between two hydrophones. The theory and simulations for the vertical line source presented here were shown to be in agreement with a modal approach presented by others, and results for cross-correlations of towed horizontal line and hyperbolic sources were shown to be in agreement with theoretical work on cross-correlations of wave generated ocean noise, modelled as a horizontal plane of sources, as well as horizontal lines of seismic surface sources. The three source configurations were compared and their advantages and disadvantages highlighted. Due to its close proximity, signals from the source column were shown to have minimal attenuation, but the source column geometry did not account for the modal continuum of the ocean sediment. The towed source scenarios were shown to suffer from intrinsic stationary-phase contributions from cross-correlations between a wave that initially undergoes a surface reflection and one that does not. The hyperbolic source was shown to have the advantage of being able to approximate the Green's function between a physical receiver and a virtual receiver; however, unlike the other two configurations, the theory assumed range independence and therefore is not applicable in some environments.

Experimental data were collected during the Shallow Water 2006 experiments. It was shown that the ocean environment was characterised by a strong thermocline and significant spatiotemporal variability. The resulting direct path acoustic field was shown to include multi-path interference, with high sensitivity to ocean variations. It was therefore difficult to extract accurate reflection coefficient information from the acoustic data. It was decided that sediment properties needed as input data for cross-correlation simulations would therefore be better estimated from available nearby sediment grab sample data.

Cross-correlations of ocean noise in the ship dominated 20–100 Hz frequency range were used to determine empirical Green's function approximations (EGFAs). Since ship noise is generated at discrete locations, long cross-correlation periods were required to give sufficient averaging for the

emergence of the Green's function. For a frequency band with sufficient levels of coherent noise, different time and frequency domain normalisation methods yielded similar cross-correlation results. A major reason for this is the spatial averaging of the noise field that occurred when noise from many ship tracks were recorded. Direct, surface reflected, and bottom-surface reflected travel times between hydrophones were determined from the EGFA envelopes for three L-shaped arrays, and agreed well with simulated data. Summing the cross-correlations between equi-spaced horizontal line array (HLA) hydrophone pairs was shown to increase the signal-to-noise ratio. Analysis of temporal variations in the cross-correlations confirmed that the signal was generally dominated by only one or two sources at any one time. Cross-correlations obtained from data recorded during Tropical Storm Ernesto were shown to be clearer than those obtained before and after the storm. This was due to a combination of a reduction in high energy discrete sources (most ships left the area during the storm), and an increase in overall sound levels. High amplitude discrete sources were not averaged out during cross-correlation, and could therefore result in EGFA peaks at times earlier than the inter-hydrophone travel times. Removal of a dominant discrete source was shown to improve the EGFA by removing a corresponding high amplitude peak at a time less than the inter-hydrophone travel time.

Cross-correlations were examined for experimental data obtained from two of the three active source configurations discussed in the theory: a source lowered vertically, and a source towed horizontally. Hyperbolic source data were collected but not analysed in detail because they showed less resemblance to the acoustic Green's function than the other two source configurations. The results were compared with cross-correlations from the ship dominated noise field, and also with cross-correlations of noise generated during a source lowering event by the ship from which the source was being controlled. The active source data EGFAs were shown to have higher signal-to-noise ratios than the EGFAs from ship noise. This was due to the

8. CONCLUSION

higher levels of coherently propagating noise that resulted from the close proximity of the source, and the even source distribution over the active source line integrals. The differences between the EGFAs and simulated Green's functions were explained with reference to theory and simulations by considering the results for a single hydrophone pair. Approximation of direct paths were shown to be consistently good for each source configuration. Surface reflection paths were shown to be more accurate for hydrophones with a greater horizontal separation, and the towed source and ship dominated ambient noise were shown to be best for determining surface reflected arrivals overall.

Two practical applications of ocean noise cross-correlation were detailed: the diagnosis of a problem with a multichannel hydrophone array, and array element self-localisation. Results obtained from active source measurements revealed that signals from several hydrophones, which were recorded on certain channels before the storm, were subsequently recorded on different channels after the storm. Noise cross-correlation of data recorded during the storm showed when, and in what manner, this channel switching took place. The inferred intervals during which each switch occurred were narrowed down to two time periods, 6 minutes and 10 seconds long respectively. With the channels re-sorted to match the correct hydrophones, the cross-correlation function time-derivative envelopes were shown to give accurate arrival time structure at all times before, during, and after the storm. In addition to the channel switching, it was noticed that differences in travel times from any given source to HLA hydrophone pairs were consistently less than expected for the assumed geometry. It was therefore hypothesised that the HLA was not lying in a straight line on the seafloor. Travel times extracted from day long ambient noise cross-correlations of data, with the channel switching taken into account, were used in a non-linear least squares inversion to estimate array geometry. The resulting curved array geometry provided more consistent acoustic travel times from active noise sources than the assumed straight line array geometry.

In conclusion, the findings discussed in this thesis increase the understanding of Green's function approximation from cross-correlation of sound in the ocean. This thesis provided a theoretical and practical understanding of Green's function estimations for two noise types: active sources and passive ship-dominated ambient noise. Cross-correlations of the ship noise, which has the advantage of no additional source instrumentation being required, were shown to be of good quality when the source distribution was fairly evenly distributed, but degenerated when the incoming source field was directionally biased. Cross-correlations of the active source signals, which have the advantages of higher frequencies, giving sharper arrival peaks, as well as controllability and continuous monitoring, were shown to have a higher signal-to-noise ratio than the ambient noise cross-correlations, but suffer from spurious arrivals that are intrinsic to the source geometry.

Two examples of how travel time information extracted from Green's function estimates can be applied to a practical situation were also provided in this thesis. By better understanding the effects of both source geometry and ocean environment on Green's function approximation, it is anticipated that in the future more of the information obtained from ocean acoustic interferometry will be able to be successfully used for practical purposes.

Much of the work presented in this thesis has either been published or submitted for publication by the author in both journals and conference proceedings, as listed in Appendix D.

8.2 Recommendations for future work

The active source experiments detailed in this thesis were the first known set of experiments of their type conducted for the purpose of ocean acoustic interferometry. Much has been learnt from analysis of the collected data, and as such, it would be beneficial to investigate in more detail the SNR of the cross-correlated waveforms as a function of environmental, geometric, and experimental parameters. The first recommendation for future work

presented here concerns such an investigation.

In addition, it would be of useful to be able to perform additional active source experiments using the information that has been learnt from the original experimental design and the subsequent analysis of data. Two of the recommendations for future work presented here concern the collection of additional active source data, and the further analysis of current data if additional information becomes available.

Travel times obtained from cross-correlations were shown to be useful for practical applications. However the work presented in this thesis provides just one step towards the larger goal of using Green's function approximations to determine environmental characteristics such as water column and seafloor properties. It is anticipated that with further development of ocean acoustic interferometry techniques, more information can be obtained from the empirical Green's function approximations and used for practical purposes. Two of the recommendations for future work therefore concern cross-correlation analysis at lower frequencies, and over greater distances than considered within this thesis, with the ultimate goals of determining and monitoring sediment properties.

8.2.1 Effect of various parameters on SNR

A detailed investigation of how certain parameters affect the signal-to-noise ratio of the cross-correlation would be helpful to understand the ocean acoustic interferometry technique more completely, and the results from such an investigation would be advantageous for the design of future experiments. Parameters that could be investigated include noise time-series bandwidth, sensor separation, recording time, attenuation, and ocean fluctuations (in particular changes in waveguide depth due to wave activity, and changes to the sound speed profile). This investigation would, at first, need to be performed by variation of each parameter individually through theory and simulation rather than experimentation, as the uncertainties and changes in the ocean environment would make it difficult to experimentally

focus upon changes in only one parameter at a time.

8.2.2 Additional source lowering experiments

If the opportunity to perform additional at-sea experiments in calmer waters becomes available, then another source lowering experiment should be performed, this time lowering over the whole water column depth. This should remove the spurious arrivals that exist due to gaps in the source distribution at the waveguide top and bottom. The more stable ocean environment will also increase the resolution of the results. Several source lowering experiments at various distances from the array should be performed. This will enable the formulation of a better understanding of the cross-correlation amplitudes and their relationship to the experimental geometry. Analysis of the amplitudes of peaks in the unsummed cross-correlations could then potentially be used to estimate surface and bottom reflection properties. This will require a multi-variable inversion method because reflection properties have angular dependence, the sea surface is not stationary, and the seafloor may be range-dependent. Multiple source lowering distances and calmer conditions would make this task more feasible than it would be for the current data set.

Lowering a source over the water column takes a time period that is long with respect to the time scale of changes in the ocean environment due to processes such as wave activity. It would therefore be desirable to perform an experiment that is geometrically similar to the lowering experiment, except that a vertical array of closely spaced sources spanning the water column is used instead. This would allow for the approximation of short-term Green's functions and would also be useful for monitoring how the Green's function approximation changes over time, and for relating these changes to short time scale processes such as wave activity, and medium time scale processes such as tidal effects.

8.2.3 Experimental hyperbolic source

The theory governing cross-correlation for a horizontal hyperbolic source was presented in Section 3.3. Experimental data from a source towed along hyperbolic paths were collected during the SW06 experiments on the same day and using the same towed source as the horizontal towed straight line source described in Chapter 6. The ship travelled along two hyperbolic paths, as shown in Figure 8.1. Hyperbolic path 1 was designed such that its focal point coincided with hydrophone 30, its apex was at a point midway between hydrophones 30 and 28, and its asymptotic origin was at a point midway between hydrophone 30 and the vertical line array (VLA). Hyperbolic path two also had the same focal point and asymptotic origin, but the apex was chosen to be midway between hydrophones 30 and 16.

The accuracy of the source track is critical around the hyperbola apex. An accurate track was able to be obtained due to the dynamic positioning capabilities of the ship, as shown in Figure 8.2.

Preliminary analysis of hyperbolic source data cross-correlations revealed that they showed less resemblance to the acoustic Green's function between two points than the straight line horizontal source tow. A contributing reason for this is likely to be that the hyperbolic configuration assumed range independence, but the environment was actually range dependent. Hence, if an accurate mapping of the local water column depth and sediment properties could be obtained, then the results from the straight line towed source and hyperbolic towed sources could potentially be used to examine sensitivity of the method to range-dependence.

In addition, if the opportunity to perform at-sea experiments in a range independent environment were to become available, the straight line and hyperbolic source tows could be repeated. This would give a better idea of how factors other than range dependence affect the results obtained using a hyperbolic configuration rather than a straight line tow.

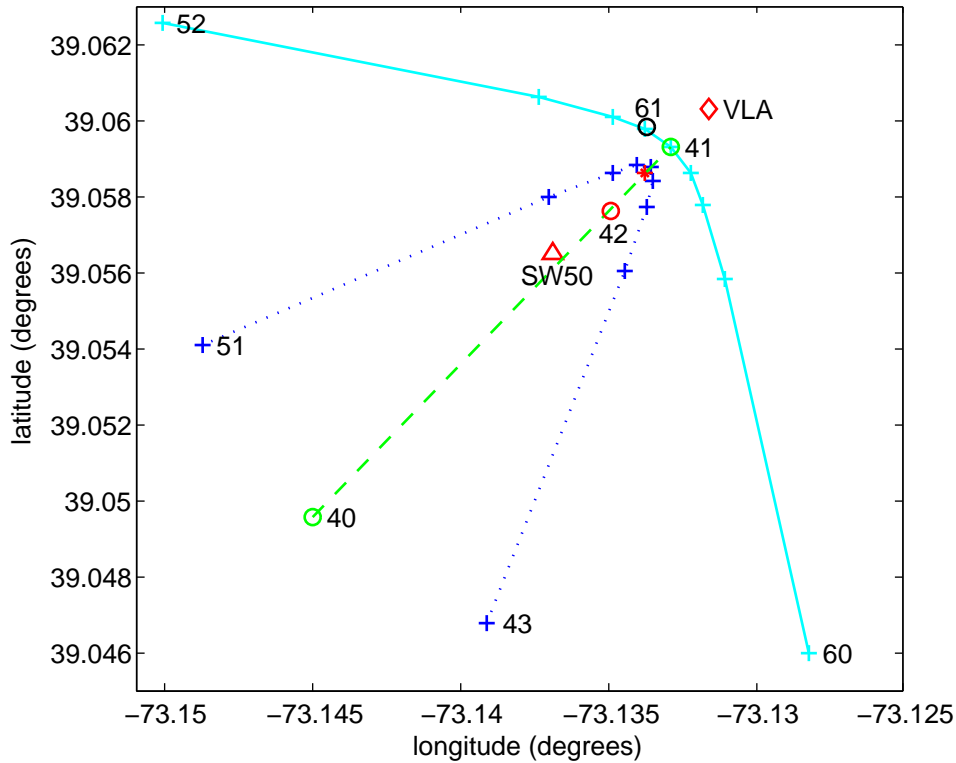


Figure 8.1: Mid-frequency SWAMI32 towed source tracks: straight (green dashed), hyperbolic path 1 (dark blue dotted), and hyperbolic path 2 (light blue). Numbered markers are waypoint numbers, ‘VLA’ is the location of the vertical portion of the SWAMI32 array, and the horizontal portion of the array extends from the VLA to the point marked by an asterisk.

8.2.4 Cross-correlations at seismic frequencies

Due to the maximum array lengths of 465 m, the minimum frequency of the acoustic data used in this thesis was 20 Hz. The SWAMI32, SWAMI52, and Shark arrays were located several kilometres apart. Cross-correlation of data from hydrophones located on separate arrays could therefore be performed at seismic frequencies. Each array had a different sampling frequency, but this would not present a problem as all data would be down-sampled to the same frequency. There were also timing errors of several seconds between the arrays. Corrections for this would need to be made

8. CONCLUSION

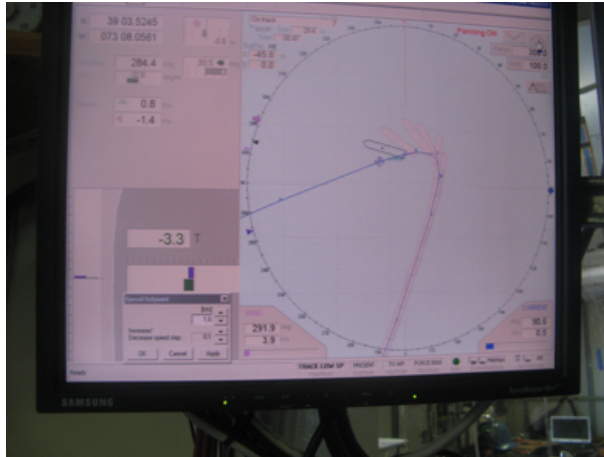


Figure 8.2: Hyperbolic tracks were achieved using dynamic ship positioning. The desired navigation path is entered into the system (blue path) and the actual ship position, shown as grey images, is mapped over time. The ship and navigation path are to scale.

before data cross-correlation.

Data from three stationary sound sources could be used to correct for the timing errors. The stationary sources were active for the first few minutes of every half hour throughout the time the arrays were deployed:

1. *National Research Laboratories* (NRL) 300 Hz linear frequency modulated signal, Bandwidth of BW=60 Hz;
2. *Woods Hole Oceanographic Institute* (WHOI) 224 Hz phase encoded signal, BW=16 Hz; and
3. WHOI 400 Hz phase encoded signal, BW=16 Hz.

The location of these sources relative to the hydrophone arrays is shown in Figure 8.3. The signals emitted by these sound sources were loud enough to be received clearly at each hydrophone array and therefore timing errors could be corrected for using the arrival times, at each array, of the signals emitted by each sound source using a triangulation method.

The greater distances and hence lower frequencies used by cross-correlating between arrays would potentially allow the current study of

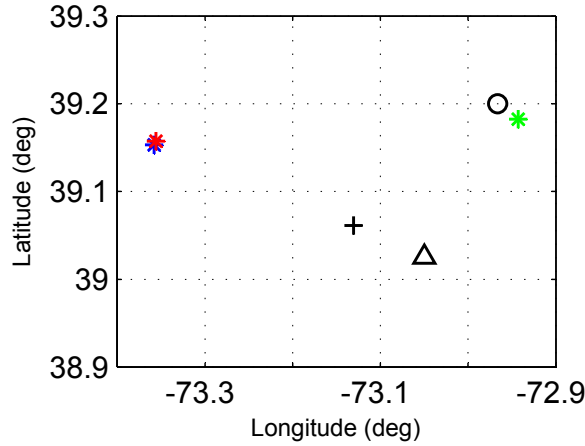


Figure 8.3: Locations of fixed sound sources: NRL 300 Hz (green asterisk), WHOI 224 Hz (blue asterisk), and WHOI 400 Hz (red asterisk); and locations of L-shaped hydrophone arrays: SWAMI52 (circle), Shark (triangle), and SWAMI32 (cross).

body waves (i.e., waves travelling within the ocean waveguide) to be extended to surface waves travelling along the seafloor-sediment interface.

8.2.5 Cross-correlations for monitoring gas hydrates

A gas hydrate sea-floor observatory has recently been installed over a one-kilometre-diameter carbonate/hydrate mound in the Gulf of Mexico Mississippi Canyon Block 118. The location of this canyon block is shown in Figure 8.4. The observatory includes four 400-m horizontal line arrays, each with 16 hydrophones, nested in a 1000 m cross configuration, as shown in Figure 8.5. The large array aperture allows for analysis of lower frequency data than that considered in this thesis.

Cross-correlation of low frequency wave generated seismo-acoustic ambient noise can therefore be used to determine travel times between pairs of sensors in the HLA. Sub-bottom paths will likely be more easily extracted from this lower frequency seismic data. Analysis of long term changes in

8. CONCLUSION

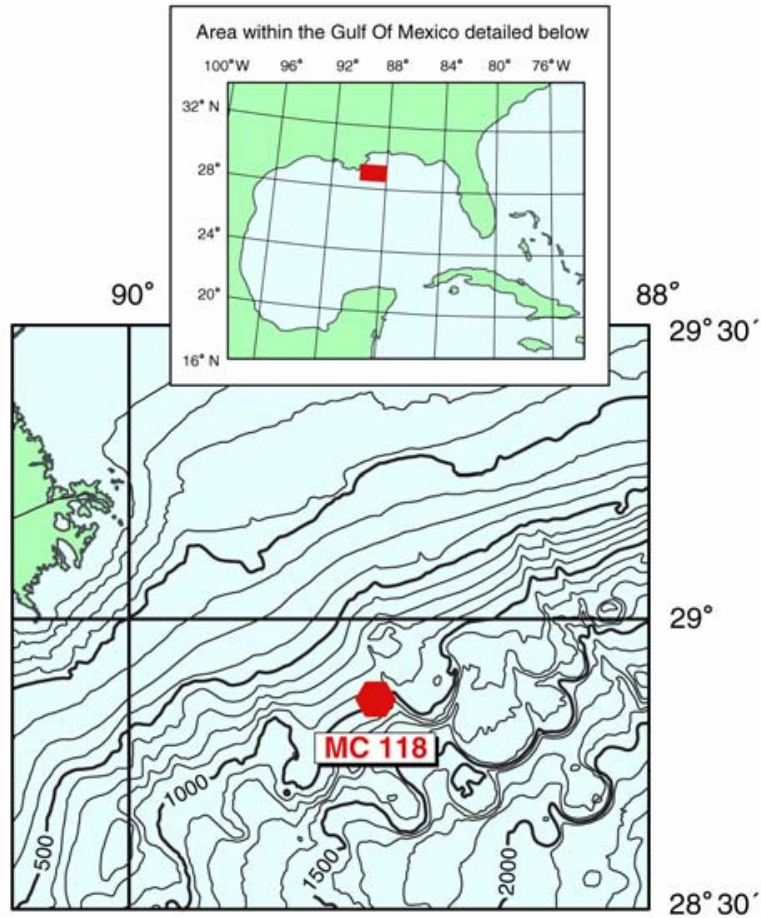


Figure 8.4: Location of Mississippi Canyon Block 118 (MC118), (source: McGee *et al.* [93]).

sub-bottom travel times between sensors can potentially be used to determine when changes have occurred in the materials through which the noise travels. This passive monitoring technique will hopefully lead to an understanding of how fluids migrate and affect the formation of hydrates within the carbonate/hydrate mound.

The seismo-acoustic monitoring technique is a large project within itself and will require several steps:

1. Using existing techniques and codes, an automatic processing technique that removes strong events, and filters and spectrally equalises

8. CONCLUSION

ing; an accurate understanding of spatio-temporal characteristics is vital since otherwise it will not be known whether any changes in the cross-correlation are due to changes in the carbonate/hydrate mound structure or whether they are simply due to changes in source characteristics.

4. Temporal stability of the technique will then need to be assessed and changes will need to be made until a monitoring capability can be demonstrated.
5. Once a monitoring capability has been demonstrated, results will need to be compared with those from high-resolution seismic data for the site to assess the accuracy of the developed technique.

References

- [1] L. M. Brekhovskikh. *Waves in layered media*. Academic Press, 1960.
(Cited on pages 1, 38, and 84)
- [2] R. J. Urick. *Principles of Underwater Sound*. McGraw-Hill Book Company, 1983.
(Cited on page 1)
- [3] H. Medwin and C. S. Clay. *Fundamentals of Acoustical Oceanography*. Academic Press, San Diego, 1998.
(Cited on pages 1 and 14)
- [4] F. B. Jensen, W. A. Kuperman, M. B. Porter, and H. Schmidt. *Computational Ocean Acoustics*. Springer-Verlang New York, Inc., Fifth Avenue, New York, NY 10010, USA, 2000.
(Cited on pages 1, 15, 16, 18, 20, 21, 22, 38, 74, and 189)
- [5] P. C. Etter. *Underwater Acoustic Modeling*. E & FN SPON, 1996.
(Cited on pages 1, 19, 20, 21, and 22)
- [6] O. Diachok, A. Caiti, P. Gerstoft, and H. Schmidt, editors. *Full field inversion methods in ocean and seismo-acoustics*. Springer, 1995.
(Cited on page 1)
- [7] O. I. Lobkis and R. L. Weaver. On the emergence of the Green's function in the correlations of a diffuse field. *J. Acoust. Soc. Am.*, 110(6):3011–3017, December 2001.
(Cited on pages 2, 28, 29, and 30)
- [8] R. L. Weaver and O. I. Lobkis. Ultrasonics without a source: Thermal fluctuation correlations at MHz frequencies. *Phys. Rev. Lett.*, 87(13):134301–1–134301–4, September 2001.
(Cited on pages 2, 30, and 150)

REFERENCES

- [9] A. E. Malcolm, J. A. Scales, and B. A. van Tiggelen. Extracting the Green function from diffuse, equipartitioned waves. *Phys. Rev. E.*, 70:015601, 2004. (Cited on pages 2 and 30)
- [10] K. van Wijk. On estimating the impulse response between receivers in a controlled ultrasonic experiment. *Geophysics*, 71(4):SI79–SI84, July–August 2006. (Cited on pages 2 and 30)
- [11] P. Roux, K. G. Sabra, W. A. Kuperman, and A. Roux. Ambient noise cross correlation in free space: Theoretical approach. *J. Acoust. Soc. Am.*, 117(1):79–84, January 2005. (Cited on pages 2, 44, 82, 86, and 122)
- [12] M. Campillo and A. Paul. Long-range correlations in the diffuse seismic coda. *Science*, 299:547–549, January 2003. (Cited on pages 2, 30, 82, and 98)
- [13] R. Snieder. Extracting the Green’s function from the correlation of coda waves: A derivation based on stationary phase. *Phys. Rev. E.*, 69(4):046610–1–8, 2004 2004. (Cited on pages 2, 25, 30, 39, 44, 86, 120, and 122)
- [14] N. M. Shapiro, M. Campillo, L. Stehly, and M. H. Ritzwoller. High-resolution surface-wave tomography from ambient seismic noise. *Science*, 307:1615–1618, March 2005. (Cited on pages 2 and 30)
- [15] K. G. Sabra, P. Roux, and W. A. Kuperman. Arrival-time structure of the time-averaged ambient noise cross-correlation function in an oceanic waveguide. *J. Acoust. Soc. Am.*, 117(1):164–174, January 2005. (Cited on pages 2, 3, 4, 30, 33, 35, 36, 39, 44, 48, 49, 60, 85, 86, 122, 123, and 150)
- [16] P. Gerstoft, K. G. Sabra, P. Roux, W. A. Kuperman, and M. C. Fehler. Green’s functions extraction and surface-wave tomography from microseisms in southern California. *Geophysics*, 71(4):SI23–SI31, July–August 2006. (Cited on pages 2, 25, 28, 94, and 99)
- [17] K. Wapenaar and J. Fokkema. Green’s function representations for seismic interferometry. *Geophysics*, 71(4):SI33–SI46, July–August 2006. (Cited on pages 2 and 30)

-
- [18] Y. Yang, M. H. Ritzwoller, A. L. Levshin, and N. M. Shapiro. Ambient noise Rayleigh wave tomography across Europe. *Geophys. J. Int.*, 168: 259–274, 2007. (Cited on pages 2, 30, and 99)
- [19] F. Lin, M. H. Ritzwoller, J. Townend, S. Bannister, and M. K. Savage. Ambient noise Rayleigh wave tomography of New Zealand. *Geophys. J. Int.*, 170(2):649–666, August 2007. (Cited on pages 2 and 30)
- [20] E. Larose, A. Khan, Y. Nakamura, and M. Campillo. Lunar subsurface investigated from correlation of seismic noise. *Geophys. Res. Lett.*, 32(16):L16201, 2005. (Cited on pages 2 and 30)
- [21] K. G. Sabra, S. Conti, P. Roux, and W. A. Kuperman. Passive *in vivo* elastography from skeletal muscle noise. *Appl. Phys. Lett.*, 90:194101, May 2007. (Cited on pages 2 and 30)
- [22] G. M. Wenz. Acoustic ambient noise in the ocean: Spectra and sources. *J. Acoust. Soc. Am.*, 34(12):1936–1956, December 1962. (Cited on pages 2 and 83)
- [23] R. J. Urick. *Principles of Underwater Sound*. McGraw-Hill, New York, 1975. (Cited on pages 2 and 83)
- [24] M. R. Loewen and W. K. Melville. A model of the sound generated by breaking waves. *J. Acoust. Soc. Am.*, 90(4):2075–2080, October 1991. (Cited on pages 2 and 83)
- [25] P. Roux, W. A. Kuperman, and the NPAL Group. Extracting coherent wave fronts from acoustic ambient noise in the ocean. *J. Acoust. Soc. Am.*, 116(4):1995–2003, October 2004. (Cited on pages 3, 4, 34, 82, 86, and 150)
- [26] L. A. Brooks and P. Gerstoft. Ocean acoustic interferometry of 20–100 Hz noise. *J. Acoust. Soc. Am.*, Submitted 2008. (Cited on pages 3, 36, and 81)

REFERENCES

- [27] K. G. Sabra, P. Roux, A. M. Thode, G. D’Spain, W. S. Hodgkiss, and W. A. Kuperman. Using ocean ambient noise for array self-localization and self-synchronization. *IEEE J. Ocean. Eng.*, 30(2):338–347, April 2005. (Cited on pages 3, 5, 7, 33, 99, and 157)
- [28] A. Curtis, P. Gerstoft, H. Sato, R. Snieder, and K. Wapenaar. Seismic interferometry—turning noise into signal. *The Leading Edge*, 25:1082–1092, September 2006. (Cited on pages 3, 30, and 35)
- [29] P. Roux and M. Fink. Green’s function estimation using secondary sources in a shallow water environment. *J. Acoust. Soc. Am.*, 113(3):1406–1416, March 2003. (Cited on pages 4, 32, 35, 37, 59, and 63)
- [30] R. Snieder, K. Wapenaar, and K. Larner. Spurious multiples in seismic interferometry of primaries. *Geophysics*, 71(4):SI111–SI124, July–August 2006. (Cited on pages 4, 35, 36, 37, 39, 44, 48, 49, 51, 60, 84, 85, and 120)
- [31] C. C. Leroy and F. Parthiot. Depth-pressure relationships in the oceans and seas. *J. Acoust. Soc. Am.*, 103(3):1346–1352, March 1998. (Cited on page 10)
- [32] H. Medwin. Speed of sound in water: A simple equation for realistic parameters. *J. Acoust. Soc. Am.*, 58(6):1318–1319, December 1975. (Cited on page 10)
- [33] V. A. Del Grosso. New equation for the speed of sound in natural waters (with comparisons to other equations). *J. Acoust. Soc. Am.*, 56(4):1084–1091, October 1974. (Cited on page 10)
- [34] K. V. Mackenzie. Nine-term equation for sound speed in the oceans. *J. Acoust. Soc. Am.*, 70:807–812, 1981. (Cited on page 10)
- [35] F. H. Fisher and V. P. Simmons. Sound absorption in sea water. *J. Acoust. Soc. Am.*, 62(3):558–564, September 1977. (Cited on page 12)

-
- [36] R. E. Francois and G. R. Garrison. Sound absorption based on ocean measurements. Part II: Boric acid contribution and equation for total absorption. *J. Acoust. Soc. Am.*, 72(6):1879–1890, December 1982.
(Cited on pages 12 and 13)
- [37] M. A. Ainslie and J. G. McColm. A simplified formula for viscous and chemical absorption in sea water. *J. Acoust. Soc. Am.*, 103(3):1671–1672, March 1998.
(Cited on page 12)
- [38] F. B. Jensen. Wave theory modeling: A convenient approach to CW and pulse propagation modeling in low-frequency acoustics. *IEEE J. Ocean. Eng.*, 13(4):186–196, October 1988.
(Cited on page 14)
- [39] J. A. Ogilvy. Wave scattering from rough surfaces. *Rep. Prog. Phys.*, 50:1553–1608, 1987.
(Cited on page 14)
- [40] MIT OpenCourseWare site. URL <http://ocw.mit.edu>.
(Cited on page 16)
- [41] P. M. Morse and K. U. Ingard. *Theoretical acoustics*. Princeton University Press, 1986.
(Cited on page 18)
- [42] M. B. Porter and H. P. Bucker. Gaussian beam tracing for computing ocean acoustic fields. *J. Acoust. Soc. Am.*, 82(4):1349–1359, October 1987.
(Cited on page 19)
- [43] H. P. Bucker. A simple 3-D Gaussian beam sound propagation model for shallow water. *J. Acoust. Soc. Am.*, 95(5):2437–2440, May 1994.
(Cited on page 19)
- [44] J. S. Perkins and R. N. Baer. An approximation of the three-dimensional parabolic equation method for acoustic propagation. *J. Acoust. Soc. Am.*, 72(2):515–522, August 1982.
(Cited on page 22)
- [45] H. P. Bucker. An equivalent bottom for use with the split-step algorithm. *J. Acoust. Soc. Am.*, 73(2):486–491, February 1983.
(Cited on page 22)

REFERENCES

- [46] D. Lee and S. T. McDaniel. A finite-difference treatment of interface conditions for the parabolic wave equation: The irregular interface. *J. Acoust. Soc. Am.*, 73(5):1441–1447, May 1983. (Cited on page 22)
- [47] R. A. Stephen. Solutions to range-dependent benchmark problems by the finite-difference method. *J. Acoust. Soc. Am.*, 87(4):1527–1534, April 1990. (Cited on page 23)
- [48] M. Porter. *The KRAKEN normal mode program*. Saclantcen Memorandum: SM-245, September 1991. (Cited on pages 23 and 74)
- [49] H. Schmidt. *OASES Version 3.1 User Guide and Reference Manual*. Department of Ocean Engineering, Massachusetts Institute of Technology, October 2004. (Cited on pages 23, 52, 72, 96, 126, and 154)
- [50] J. F. Claerbout. Synthesis of a layered medium from its acoustic transmission response. *Geophysics*, 33(2):264–269, April 1968. (Cited on page 24)
- [51] J. F. Claerbout. *Fundamentals of geophysical data processing*. Blackwell, 1976. (Cited on page 24)
- [52] J. Rickett and J. Claerbout. Acoustic daylight imaging via spectral factorization: helioseismology and reservoir monitoring. *The Leading Edge*, 18(8):957–960, 1999. (Cited on page 24)
- [53] T. L. Duvall Jr, S. M. Jefferies, J. W. Harvey, and M. A. Pomerantz. Time-distance helioseismology. *Nature*, 362:430–432, April 1993. (Cited on page 24)
- [54] C. R. Farrar and G. H. James III. System identification from ambient vibration measurements on a bridge. *J. Sound Vib.*, 205(1):1–18, August 1997. (Cited on page 24)
- [55] P. Roux, K. G. Sabra, P. Gerstoft, W. A. Kuperman, and M. C. Fehler. P-waves from cross correlation of seismic noise. *Geophys. Res. Lett.*, 32:L19303, 2005. (Cited on page 25)

-
- [56] A. Derode, E. Larose, M. Tanter, J. de Rosny, A. Tourin, M. Campillo, and M. Fink. Recovering the Green’s function from field-field correlations in an open scattering medium. *J. Acoust. Soc. Am.*, 113(6): 2973–2976, June 2003. (Cited on pages 30, 37, 86, and 150)
- [57] K. Wapenaar. Retrieving the elastodynamic Green’s function of an arbitrary inhomogeneous medium by cross correlation. *Phys. Rev. Lett.*, 93(25):254301–1–254301–4, December 2004. (Cited on page 30)
- [58] D.-J. van Manen, J. O. A. Robertsson, and A. Curtis. Modeling of wave propagation in inhomogeneous media. *Phys. Rev. Lett.*, 94(16): 164301–1–164301–4, April 2005. (Cited on page 30)
- [59] E. Larose, A. Derode, M. Campillo, and M. Fink. Imaging from one-bit correlations of wideband diffuse wavefields. *J. Appl. Phys.*, 95: 8393–8399, 2004. (Cited on pages 30 and 99)
- [60] P. Gerstoft, K. Sabra, P. Roux, W. A. Kuperman, and W. S. Hodgkiss. Passive acoustic and seismic tomography with ocean ambient noise in ORION. In *Proceedings of the International Conference “Underwater Acoustic Measurements: Technologies & Results” Heraklion, Crete, Greece, 28 June – 1 July 2005*. (Cited on page 30)
- [61] K. G. Sabra, P. Gerstoft, P. Roux, and W. A. Kuperman. Extracting time-domain Green’s function estimates from ambient seismic noise. *Geophys. Res. Lett.*, 32:L03310, 2005. (Cited on pages 30 and 102)
- [62] G. D. Bensen, M. H. Ritzwoller, M. P. Barmin, A. L. Levshin, F. Lin, M. P. Moschetti, N. M. Shapiro, and Y. Yang. Processing seismic ambient noise data to obtain reliable broad-band surface wave dispersion measurements. *Geophys. J. Int.*, 169:1239–1260, 2007. (Cited on pages 30, 96, 99, and 102)
- [63] K. G. Sabra, E. S. Winkel, D. A. Bourgoyne, B. R. Elbing, S. L. Ceccio, M. Perlin, and D. R. Dowling. Using cross correlations of turbulent

REFERENCES

- flow induced vibrations for structural health monitoring. *J. Acoust. Soc. Am.*, 121(4):1987–1995, April 2007. (Cited on page 30)
- [64] W. A. Kuperman. Utilizing acoustic noise. In *Pacific Rim underwater acoustics conference*, 2007. (Cited on page 31)
- [65] M. Siderius, C. H. Harrison, and M. B. Porter. A passive fathometer technique for imaging seabed layering using ambient noise. *J. Acoust. Soc. Am.*, 120(3):1315–1323, September 2006. (Cited on pages 34 and 86)
- [66] P. Gerstoft, W. S. Hodgkiss, M. Siderius, C.-F. Huang, and C. H. Harrison. Passive fathometer processing. *J. Acoust. Soc. Am.*, 123(3):1297–1305, March 2008. (Cited on pages 34 and 86)
- [67] C. H. Harrison and M. Siderius. Bottom profiling by correlating beam-steered noise sequences. *J. Acoust. Soc. Am.*, 123(3):1282–1296, March 2008. (Cited on page 34)
- [68] C. M. Bender and S. A. Orszag. *Advanced Mathematical Methods for Scientists and Engineers: Asymptotic Methods and Perturbation Theory*. McGraw-Hill, 1978. (Cited on pages 38, 39, 85, and 120)
- [69] L. A. Brooks and P. Gerstoft. Ocean acoustic interferometry. *J. Acoust. Soc. Am.*, 121(6):3377–3385, June 2007. (Cited on pages 44, 84, 85, and 86)
- [70] D. Tang, J. N. Moum, J. F. Lynch, P. Abbot, R. Chapman, P. H. Dahl, T. F. Duda, G. Gawarkiewicz, S. Glenn, J. A. Goff, H. Graber, J. Kamp, A. Maffei, J. D. Nash, and A. Newhall. Shallow water '06: A joint acoustic propagation/ nonlinear internal wave physics experiment. *Oceanography*, 20(4):156–167, December 2007. (Cited on pages 65 and 66)
- [71] Y.-M. Jiang and N. R. Chapman. Bayesian geoacoustic inversion in a dynamic shallow water environment. *J. Acoust. Soc. Am.*, 123(6):EL155–EL161, June 2008. (Cited on pages 65, 77, and 78)

-
- [72] C.-F. Huang, P. Gerstoft, and W. S. Hodgkiss. Effect of ocean sound speed uncertainty on matched-field geoacoustic inversion. *J. Acoust. Soc. Am.*, 123(6):EL162–EL168, June 2008. (Cited on pages 65, 77, and 78)
- [73] J. A. Goff, B. J. Kraft, L. A. Mayer, S. G. Schock, C. K. Sommerfield, H. C. Olson, S. P. S. Gulick, and S. Nordfjord. Seabed characterization on the New Jersey middle and outer shelf: Correlatability and spatial variability of seafloor sediment properties. *Mar. Geol.*, 209:147–172, 2004. (Cited on pages 67, 79, 104, and 126)
- [74] N. R. Chapman. Empirical geoacoustic model for SW06 experimental sites. Pre-cruise document, 2006. (Cited on page 67)
- [75] A. E. Newhall, T. F. Duda, K. von der Heydt, J. D. Irish, J. N. Kemp, S. A. Lerner, S. P. Liberatore, Y.-T. Lin, J. F. Lynch, A. R. Maffei, A. K. Morozov, A. Shmelev, C. J. Sellers, and W. E. Witzell. Acoustic and oceanographic observations and configuration information for the WHOI moorings from the SW06 experiment. Technical report, Woods Hole Oceanographic Institute, May 2007. (Cited on pages 66, 68, 191, and 198)
- [76] *SBE 9plus CTD User’s manual*. Sea-Bird Electronics, Inc. URL <http://www.seabird.com>. (Cited on page 69)
- [77] M. Badiy, Y. Mu, J. Lynch, J. Apel, and S. Wolf. Temporal and azimuthal dependence of sound propagation in shallow water with internal waves. *J. Acoust. Soc. Am.*, 27(1):117–129, January 2002. (Cited on page 72)
- [78] C. W. Holland. Seabed reflection measurement uncertainty. *J. Acoust. Soc. Am.*, 114(4):1861–1873, October 2003. (Cited on page 73)
- [79] A. Turgut. SW06 bottom characterization by using chirp sonar and GeoProbe data. In *Shallow Water 2006 Experiment San Diego Workshop*, 2007. (Cited on page 78)

REFERENCES

- [80] K. Wapenaar. Green's function retrieval by cross-correlation in case of one-sided illumination. *Geophys. Res. Lett.*, 33:L19304, October 2006. (Cited on page 82)
- [81] K. G. Sabra, P. Gerstoft, P. Roux, W. A. Kuperman, and M. C. Fehler. Surface wave tomography from microseisms in Southern California. *Geophys. Res. Lett.*, 32:L14311, 2005. (Cited on pages 94 and 99)
- [82] A. Derode, A. Tourin, and M. Fink. Ultrasonic pulse compression with one-bit time reversal through multiple scattering. *J. Appl. Phys.*, 85:6343, 1999. (Cited on page 99)
- [83] N. M. Shapiro and M. Campillo. Emergence of broadband Rayleigh waves from correlations of the ambient seismic noise. *Geophys. Res. Lett.*, 31:L07614, 2004. (Cited on page 99)
- [84] F. J. Sánchez-Sesma and M. Campillo. Retrieval of the Green's function from cross correlation: The canonical elastic problem. *Bull. Seism. Soc. Am.*, 96(3):1182–1191, June 2006. (Cited on page 104)
- [85] L. A. Brooks and P. Gerstoft. Experimental ocean acoustic interferometry. *J. Acoust. Soc. Am.*, Submitted 2008. (Cited on page 118)
- [86] L. A. Brooks, P. Gerstoft, and D. P. Knobles. Multichannel array diagnosis using noise cross-correlation. *J. Acoust. Soc. Am.*, 124(4):EL203–EL209, October 2008. (Cited on page 145)
- [87] M. Celis, J. E. Dennis, and R. A. Tapia. A trust region strategy for nonlinear equality constrained optimization. *Numerical Optimization 1994*, pages 71–82, 1985. (Cited on pages 147 and 160)
- [88] T. F. Coleman and Y. Li. On the convergence of reflective Newton methods for large-scale nonlinear minimization subject to bounds. *Mathematical Programming*, 67(2):189–224, 1994. (Cited on pages 147 and 160)

-
- [89] P. S. Wilson, J. L. Ellzey, and T. G. Muir. Experimental investigation of the combustive sound source. *IEEE J. Ocean. Eng.*, 20(4):311–320, October 1995. (Cited on page 147)
- [90] W. S. Hodgkiss. Shape determination of a shallow-water bottomed array. In *Proc. OCEANS’89*, pages 1199–1204, 1989. (Cited on page 157)
- [91] W. S. Hodgkiss, P. Gerstoft, and J. J. Murray. Array shape estimation from sources of opportunity. In *OCEANS 2003 Proc.*, 2003. (Cited on page 157)
- [92] S. Dosso, N. E. B. Collison, G. J. Heard, and R. I. Verrall. Experimental validation of regularized array element localization. *J. Acoust. Soc. Am.*, 115(5):2129–2137, May 2004. (Cited on page 157)
- [93] T. McGee, J. R. Woolsey, L. Lapham, R. Kleinberg, L. Macelloni, B. Battista, C. Knapp, S. Caruso, V. Goebel, R. Chapman, and P. Gerstoft. Structure of a carbonate/hydrate mound in the Northern Gulf of Mexico. In *6th International Conference on Gas Hydrates, Vancouver, British Columbia, Canada*, 2008. (Cited on page 174)
- [94] T. M. McGee. Presented to the international association of oil and gas producers. Technical report, 2007. (Cited on page 175)
- [95] W. S. Hodgkiss. DURIP: Autonomous broadband receive arrays. Technical report, Marine Physical Laboratory, Scripps Institution of Oceanography, 1997. Final Report, Contract N00014-05-1-0447. (Cited on page 193)
- [96] SWAMI mooring diagrams supplied by ARL-UT engineers. (Cited on pages 195 and 196)

Appendix A

Normalisation for Impedance Changes

In order to satisfy the equal amplitude criterion of Section 3.1.2, the cross-correlations from sources that span an area of varying impedance should be normalised by dividing by $\frac{\rho_s c}{\sin \theta_s}$, as calculated at the source location, where ρ is medium density, c is medium sound speed, and θ is the grazing angle with the horizontal. This can be understood by considering the following.

Consider the geometry of Figure 3.3(a). Let R be a reflection from the bottom of the water column, R' be a reflection from the top of the sediment, R'' a reflection from the bottom of the sediment, T a transmission from the water column into the sediment, and T' a transmission from the sediment to the water column. If the source amplitude is S_a , the cross-correlation of the acoustic path from S to A with the path from S to B yields an amplitude of $S_a T T' \times S_a R$. Similarly, for the geometry of Figure 3.3(b) the cross-correlation of the paths from S' to each receiver yield an amplitude of $S_b R' T' \times S_b T'$. The two will cancel only if

$$S_a T T' \times S_a R = -S_b R' T' \times S_b T'. \quad (\text{A.1})$$

The reflection coefficient at the interface of two media is defined as [4]

$$R_{12} = \frac{\frac{\rho_2 c_2}{\sin \theta_2} - \frac{\rho_1 c_1}{\sin \theta_1}}{\frac{\rho_2 c_2}{\sin \theta_2} + \frac{\rho_1 c_1}{\sin \theta_1}}, \quad (\text{A.2})$$

A. NORMALISATION FOR IMPEDANCE CHANGES

where medium 1 is the medium in which the wave is travelling, and medium 2 is the medium on the other side of the interface. The transmission coefficient from medium 1 to 2 is

$$T_{12} = \frac{2 \frac{\rho_2 c_2}{\sin \theta_2}}{\frac{\rho_2 c_2}{\sin \theta_2} + \frac{\rho_1 c_1}{\sin \theta_1}}. \quad (\text{A.3})$$

Substituting Eq. (A.2) and Eq. (A.3) into Eq. (A.1) and simplifying yields

$$\frac{S_a^2}{\frac{\rho_a c_a}{\sin \theta_a}} = \frac{S_b^2}{\frac{\rho_b c_b}{\sin \theta_b}}, \quad (\text{A.4})$$

where subscript a denotes the water column and subscript b denotes the sediment.

Appendix B

Array Details

Four arrays were used to collect data: MPL-VLA1, SWAMI32, SWAMI52, and Shark. The MPL-VLA1 is a vertical line array that is able to maintain its vertical configuration after deployment due to an anchor at the array bottom, and a buoyancy float at the top. The other three arrays are L-shaped, with a vertical line array (VLA) component and a horizontal line array (HLA) component. The vertical components maintain their shape due to buoyancy floats at the top and electronics modules that are heavy enough to anchor them at the bottom. The horizontal arrays are all anchored at both ends so that they retain their straight horizontal configuration. Descriptions of the SW06 array dimensions with mooring diagrams, as well as details of the data acquisition system for each array, are included in this appendix. Photographs of the arrays are included in the thesis body as Figure 4.2. All of the information in this appendix has been provided courtesy of the Marine Physical Laboratory, Scripps Institution of Oceanography (MPL-VLA1 array), Applied Research Laboratories, University of Texas at Austin (SWAMI arrays), and Woods Hole Oceanographic Institute [75] (Shark array).

B.1 Array geometries

The array geometries and mooring diagrams are detailed here. The mooring diagrams are the *a priori* experimental designs, and as such, the depth specified on each mooring diagram is different from the surveyed water depth at the experimental site.

B.1.1 MPL-VLA1 array

The MPL-VLA1 array is a 16 element VLA with elements denoted H-1–H-16. A mooring diagram of the configuration is shown in Figure B.1. During the SW06 experiments it was deployed at a depth of 79 m, at a surveyed location of $39^{\circ} 01.477' \text{ N}$, $73^{\circ} 02.256' \text{ W}$. The elements were evenly spaced vertically at 3.75 m intervals, the lowest, H-1, being 8.2 m above the seafloor.

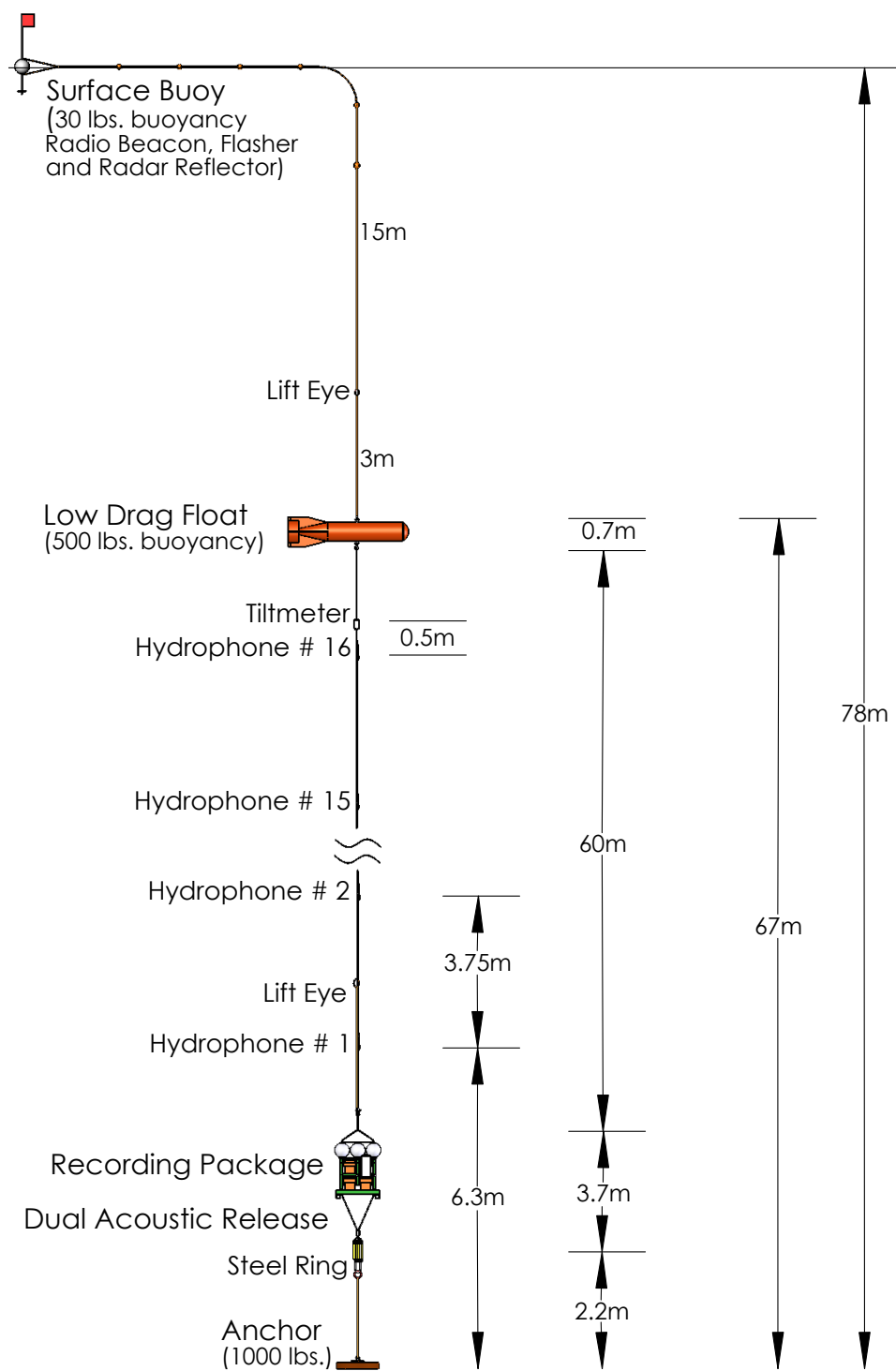


Figure B.1: MPL-VLA1 mooring diagram (source: Hodgkiss [95]).

B. ARRAY DETAILS

B.1.2 SWAMI arrays

The SWAMI32 array consists of a 12 element VLA, with elements denoted H-1–H-12, and a 20 element HLA, with elements denoted H-13–H-32. A mooring diagram of the configuration is shown in Figure B.2. During the SW06 experiments it was deployed at a depth of 68.5 m, with the base of the VLA at a surveyed location of $39^{\circ} 03.6180' \text{ N}$, $73^{\circ} 07.8970' \text{ W}$. The two lowest VLA elements, H-11 and H-12, were tied off approximately 2 m above the seafloor. The other 10 VLA elements were evenly spaced at 5.95 m intervals, the lowest, H-10, being 4.65 m above the seafloor. The first HLA element, H-13, was located 7.795 m from the base of the VLA at a bearing of 224° True . The vector of distances of H-14–H-32 from H-13 in metres was [20.32, 39.66, 58.06, 75.57, 92.24, 108.10, 123.20, 137.57, 151.24, 164.25, 176.63, 188.42, 199.64, 210.31, 220.47, 230.14, 239.34, 248.10, 256.43].

The SWAMI52 array consists of a 16 element VLA, with elements denoted H-1–H-16, and a 36 element HLA, with elements denoted H-17–H-52. A mooring diagram of the configuration is shown in Figure B.3. During the SW06 experiments it was deployed at a depth of 73.8 m, with the base of the VLA at a surveyed location of $39^{\circ} 12.0010' \text{ N}$, $72^{\circ} 57.9740' \text{ W}$. The two lowest VLA elements, H-15 and H-16, were tied off approximately 2 m above the seafloor. The other 14 VLA elements were evenly spaced at 4.37 m intervals, the lowest, H-14, being 4.3 m above the seafloor. The first HLA element, H-17, was located 7.795 m from the base of the VLA at a bearing of 314° True (i.e. perpendicular to the SWAMI32 array). The vector of distances of H-18–H-52 from H-17 in metres was [15.84, 29.48, 41.21, 51.32, 60.00, 67.49, 73.94, 79.48, 84.60, 89.33, 93.70, 97.74, 101.47, 104.91, 108.09, 111.03, 113.75, 116.25, 118.97, 121.91, 125.09, 128.53, 132.26, 136.30, 140.67, 145.40, 150.52, 156.07, 162.51, 169.99, 178.69, 188.79, 200.52, 214.16, 230.00].

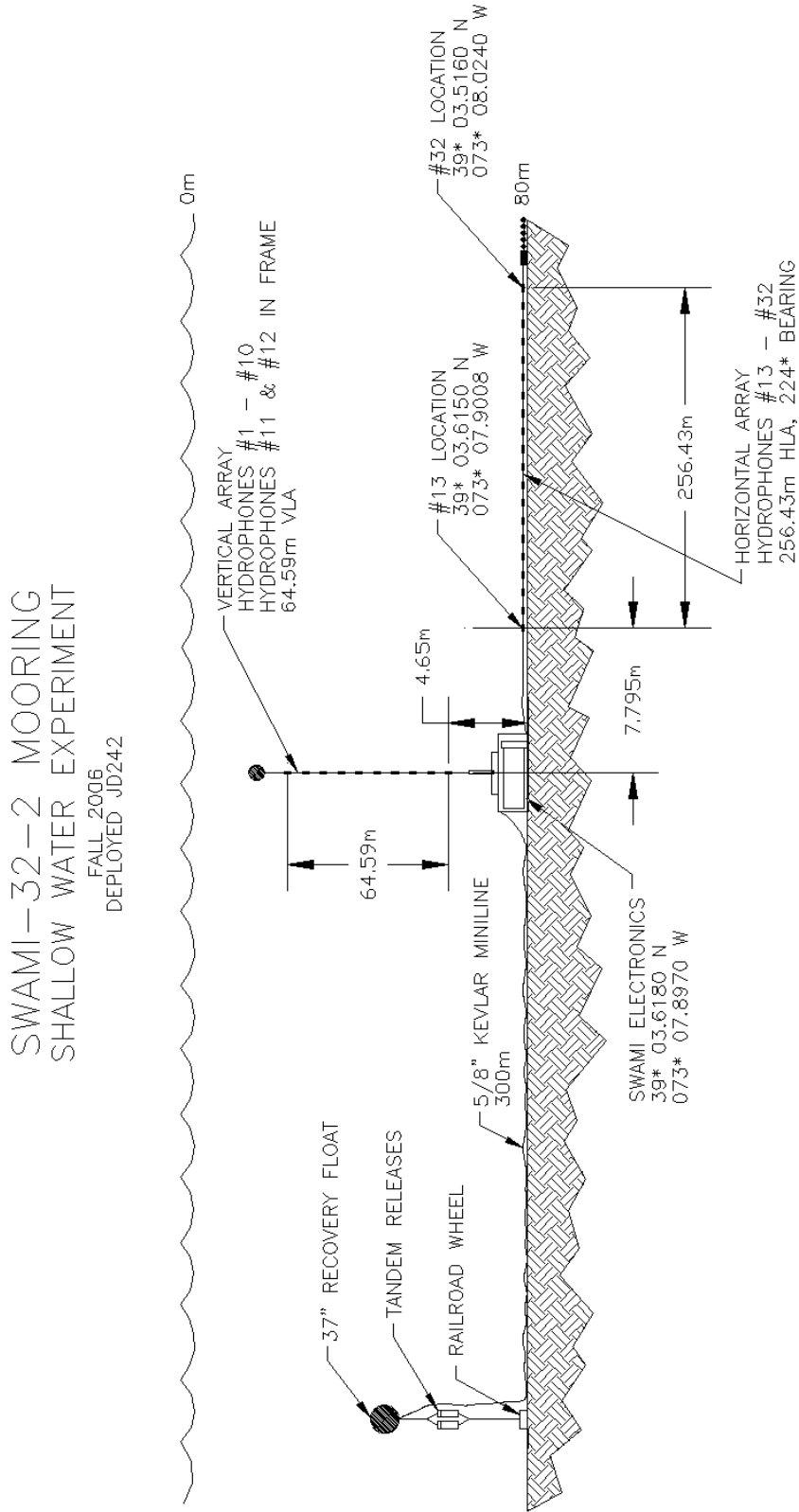


Figure B.2: SWAMI32 mooring diagram (source: ARL-UT [96]).

B. ARRAY DETAILS

SWAMI-52 MOORING
SHALLOW WATER EXPERIMENT

FALL 2006
DEPLOYED JD236

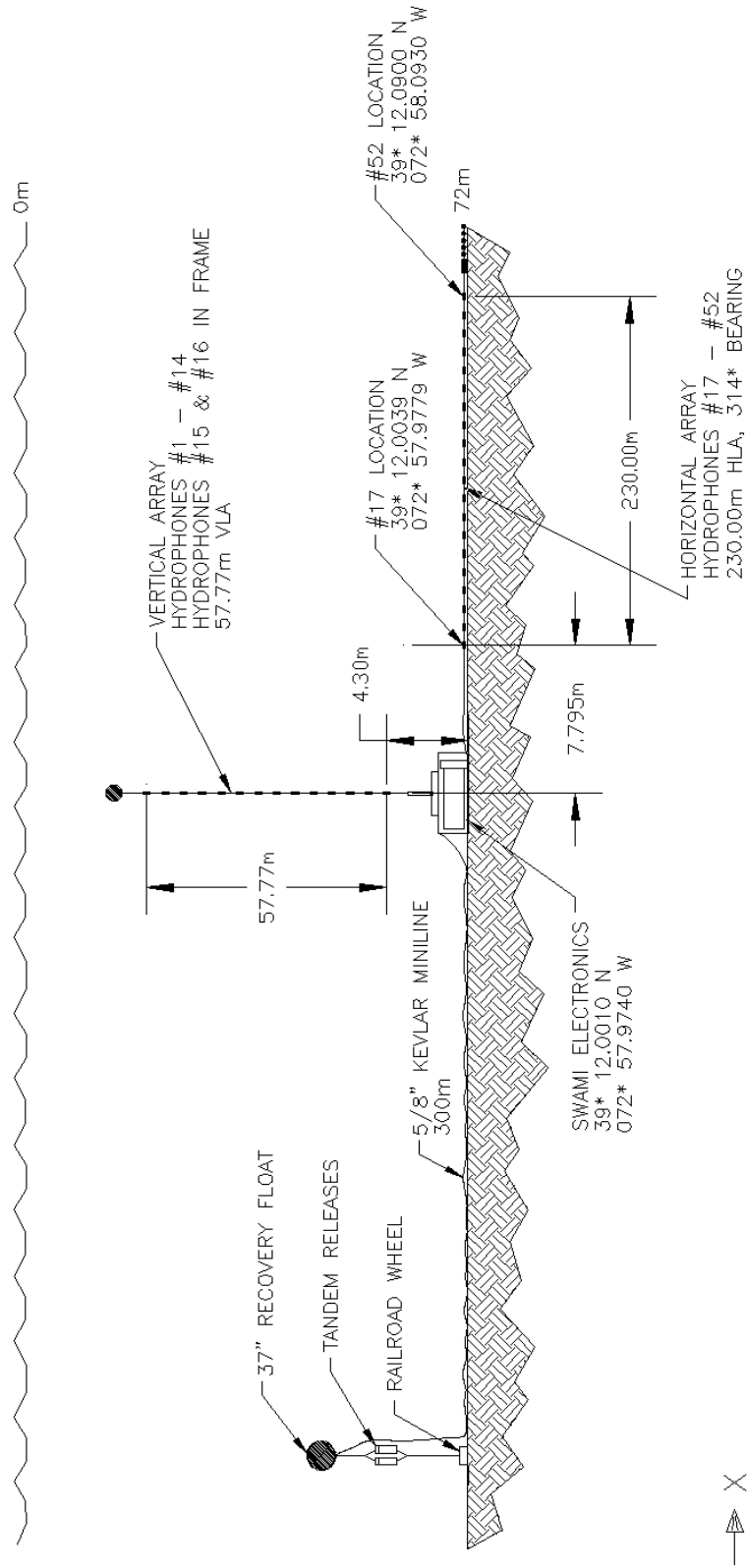


Figure B.3: SWAMI52 mooring diagram (source: ARL-UT [96]).

B.1.3 Shark array

The Shark L-array consists of a 16 element VLA, with elements denoted H-0–H-15, and a 32 element HLA, with elements denoted H-16–H-47. A mooring diagram of the configuration is shown in Figure B.4. During the SW06 experiments the array was deployed at a depth of 79 m, with the base of the VLA at a surveyed location of $39^{\circ} 01.2627' \text{ N}$, $73^{\circ} 02.9887' \text{ W}$. The three lowest VLA elements, H-13–H-15, were tied off 1.25 m above the seafloor. The vector of depths in metres below the sea surface of the other 12 VLA elements, H-0–H-12, was [13.5, 17.25, 21.0, 24.75, 28.5, 32.35, 36.0, 39.75, 43.5, 47.25, 54.75, 62.25, 69.75]. The HLA bearing was $1.45^{\circ} \text{ True}$. The HLA elements, H-47–H-16, were evenly spaced at 15 m intervals, with the closest, H-47, located 3 m from the base of the VLA.

B. ARRAY DETAILS

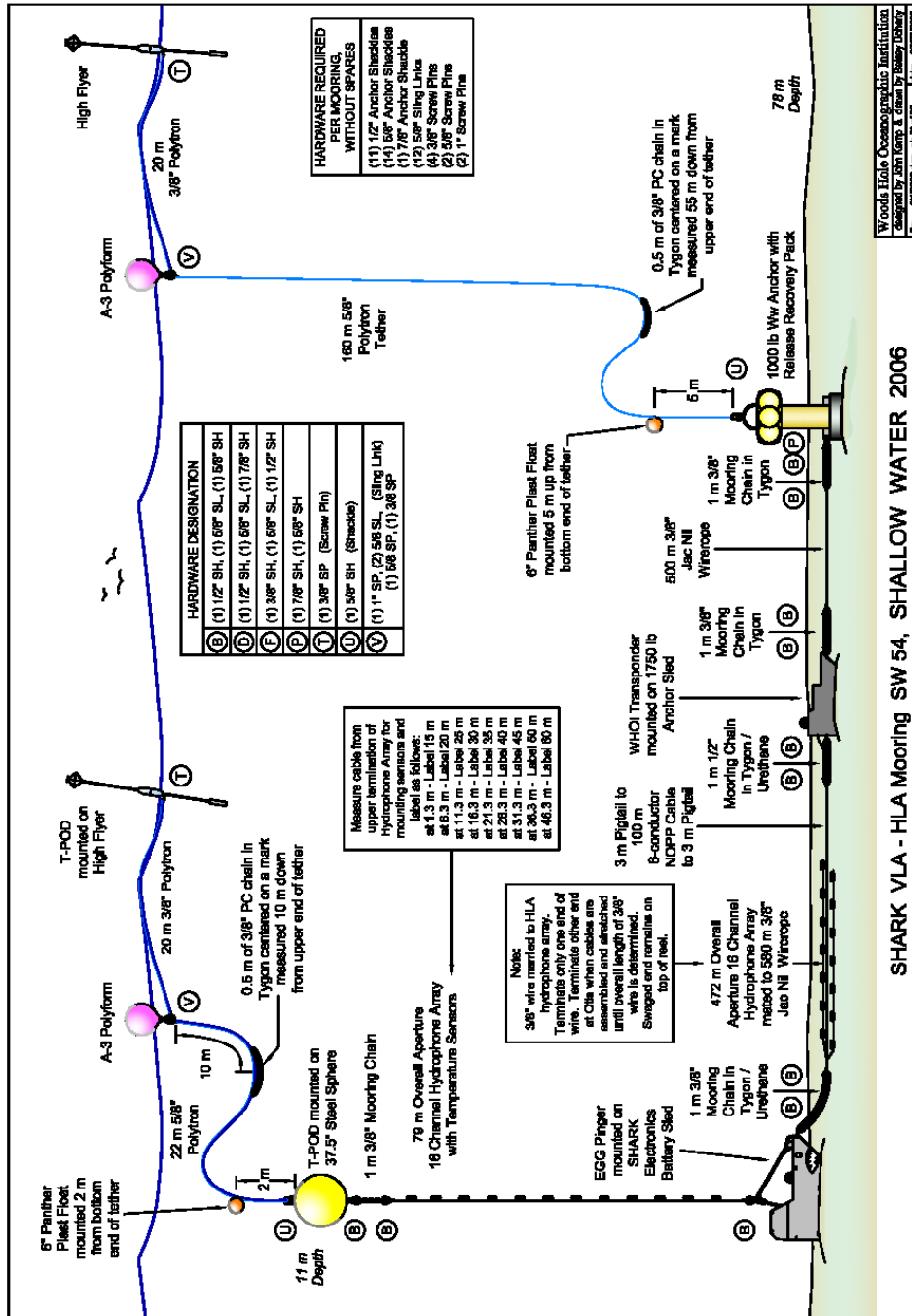


Figure B.4: Shark mooring diagram (source: Newhall *et al.* [75]).

B.2 Array data acquisition specifications

Details of the data acquisition system for each array are presented in Table B.1.

	SWAMI arrays	MPL-VLA1 array	Shark array
Resolution	16 bits	16 bits	16 bits
Sampling rate	2400 Hz (SWAMI52) 6250 Hz (SWAMI32)	50 kHz	9765.625 Hz
Recording media	DAT DDS-3 (digital audio tape digital data storage)	IDE (integrated drive electronics) hard disk drive	PC/104-plus stack (PC compatible circuit board with a peripheral component interface bus addition)
Capacity	264 Gb	470 Gb	~ 4 TB
Continuous recording	8 days	116 hours	43 days
Hydrophone sensitivity	-222 dB re 1 V/ μ Pa or -168 dB re 1 V/ μ Pa (variable)	-198 dB re 1 V/ μ Pa	-170 dB re 1 V/ μ Pa
Input gain	variable: 10 dB, 30 dB, 50 dB or 70 dB	variable: 20 dB, 40 dB or 60 dB	21 dB
Frequency range	rated down to 20 Hz	20 Hz – 30 kHz	10 Hz – 10 kHz

Table B.1: Data acquisition capabilities of the SWAMI arrays, MPL-VLA1 array, and Shark array.

Appendix C

The Inversion Process

The inversion process attempts to determine a model, \mathbf{m} , which optimises an objective function, ϕ , for a set of physical data measurements, \mathbf{p} . The solution of an inverse problem has two components, namely the forward model, and the inverse model. The forward model determines the mathematical relationship between the unknown parameters to be estimated and the acoustic field. Using the measured acoustic field and the forward mathematical relationship, the inverse model determines the rule used to calculate the unknown parameters.

The inverse problem requires P data measurements, forming vector

$$\mathbf{p} = [p_1, p_2, \dots, p_P]^T. \quad (\text{C.1})$$

The Q unknown parameters to be determined form vector

$$\mathbf{q} = [q_1, q_2, \dots, q_Q]^T, \quad (\text{C.2})$$

where $P > Q$. Using the forward model, \mathbf{p} is predicted for different combinations of \mathbf{q} . The inverse model is employed to identify values of \mathbf{q} that give the best prediction of \mathbf{p} . As the number of measurements exceeds the number of unknown parameters, an exact solution that satisfies all N measured parameters does not generally exist. Hence, a solution that best satisfies the measured parameters must be obtained. This is done by repeatedly running the forward and inverse models with different \mathbf{q} vectors, as

C. THE INVERSION PROCESS

depicted in Figure C.1, until the difference between the measured acoustic field and the field predicted by the forward model is minimised.

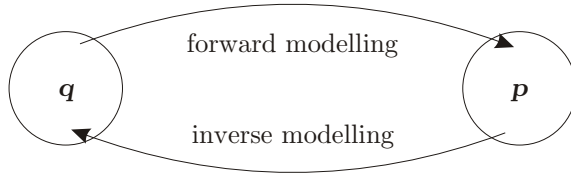


Figure C.1: The inversion process.

The inversion process can be carried out using either non-linear techniques based on full-field global optimisation, or using linear inversion techniques that match only selected features of the acoustic field with corresponding replica features, that is, features that are estimated from the inversion. These optimisation techniques seek to minimise the objective function $\phi = f(\mathbf{p}, \mathbf{q}(\mathbf{m}))$, where \mathbf{m} is the set of physical parameters to be estimated.

Appendix D

Publications

Journal publications and conference proceedings that have directly resulted from the work presented in this thesis are listed here:

D.1 Journal papers

L. A. Brooks and P. Gerstoft, “Ocean acoustic interferometry,” *J. Acoust. Soc. Am.* 121(6), pp. 3377–3385, June 2007.

L. A. Brooks, P. Gerstoft, and D. P. Knobles, “Multichannel array diagnosis using noise cross-correlation,” *J. Acoust. Soc. Am.* 124(4), pp. EL203–EL209, October 2008.

L. A. Brooks and P. Gerstoft, “Ocean acoustic interferometry of 20–100 Hz noise,” *J. Acoust. Soc. Am.* Submitted 2008.

L. A. Brooks and P. Gerstoft, “Experimental ocean acoustic interferometry,” *J. Acoust. Soc. Am.* Submitted 2008.

D.2 Refereed conference papers

L. A. Brooks and P. Gerstoft, “Ocean acoustic interferometry experiment,” proceedings of ICSV14, Cairns, Australia, July 2007.

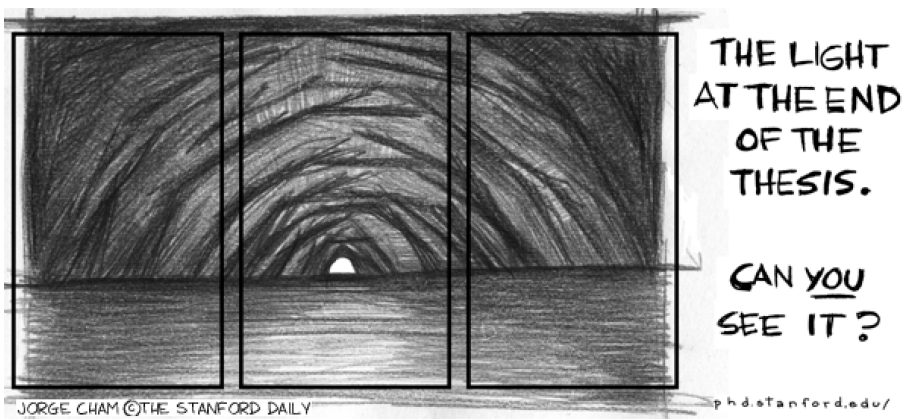
D.3 Invited talks

P. Gerstoft, L. A. Brooks*, S. Fried, W. A. Kuperman, and K. G. Sabra, “Ocean acoustic interferometry using noise and active sources,” AGU Fall Meeting, San Francisco, December 10–14 2007.

D.4 Other conference proceedings

L. A. Brooks and P. Gerstoft, “Green’s function retrieval through ocean acoustic interferometry (A),” 153rd Meeting of the Acoustical Society of America *J. Acoust. Soc. Am.* 121(5), p. 3102, May 2007.

L. A. Brooks and P. Gerstoft, “Extracting Green’s functions from noise correlation of SW06 data,” Acoustics ’08, Paris, June 29 – July 4, 2008.



JORGE CHAM © THE STANFORD DAILY

phd.stanford.edu/

source: "Piled Higher and Deeper" by Jorge Cham - www.phdcomics.com